Nanomechanics of Confined Polymer Systems

Inauguraldissertation

zur

Erlangung der Würde eines Doktors der Philosophie

vorgelegt der

Philosophisch-Naturwissenschaftlichen Fakultät

der Universität Basel

von

Janne T. Hyötylä

aus Finnland

Basel, 2016

Genehmigt von der Philosophisch-Naturwissenschaftlichen Fakultät
auf Antrag von

Prof. Dr. Roderick Lim
Prof. Dr. Thomas Pfohl

Basel, den 22.4.2014

Prof. Dr. Jörg Schibler

Dekan

Abstract

Nanomechanics of Confined Polymer Systems

Polymers anchored to surfaces play an important role in nature and technology, and regulate diverse interfacial phenomena in areas such as tribology and colloidal stability. Polymers grafted to surfaces at high density form elongated "brushes" with characteristic lengths much larger than free coils in solution. These brushes can reduce interfacial friction and wear as well as impart fouling resistance to surfaces. In light of these functionalities it is important to understand the behaviour of surface-grafted polymers at the molecular and nanoscopic level. An emerging area of interest are polymers attached to nanopores. Theoretical studies predict interesting morphologies and dynamics of such confined brushes in and around nanopores, but nanopore environments have been difficult to study experimentally. In this thesis a unique polymer-functionalized nanopore-like experimental system is presented, functionalized with poly(ethylene glycol) (PEG). Atomic force microscopy (AFM) is employed to probe the PEG brushes with nanometre spatial precision and sub-nanonewton force sensitivity, revealing novel dynamics depending on the local grafting position of PEG with respect to the nanopore geometry. Further, AFM is used together with fluorescence microscopy to show how polymer–protein interactions can be used together with the anti-fouling property of PEG to sort specific biomolecules from complex biological fluids to nanoscale targets. This shows a way how to confer biological recognition and specificity to synthetic nanoscale systems which is important for biosensing and bioseparation applications.

Contents

List of Figures

List of Tables

Abbreviations

AdG	Alexander–de Gennes polymer brush model
AFM	Atomic force microscopy/microscope
Anti-PEG	Antibody that recognizes PEG
BSA	Bovine serum albumin
DI H$_2$O	Deionized water
DLS	Dynamic light scattering
EBL	Electron beam lithography
FV	Force volume
IgG	Immunoglobulin G
IPA	Isopropanol
mPEG-SH	Methoxy-PEG-thiol
MWC	Milner–Witten–Cates polymer brush model
NA	Numeric aperture
NPC	Nuclear pore complex
PBS	Phosphate-buffered saline
PEG	Poly(ethylene glycol)
PSD	Position-sensitive detector
SEM	Scanning electron microscopy/microscope
SPR	Surface plasmon resonance
TIRF	Total internal reflection fluorescence

Symbols

a	monomer size	m
c	concentration	g/l
d	separation distance (tip-sample distance)	m
E	Young's modulus	Pa
f	free energy	J
F	force	N
g	average surface grafting distance	m
g_{SPR}	grafting distance measured by SPR	m
h	polymer brush height	m
I	fluorescence intensity	
k	cantilever spring constant	N/m
k_B	Boltzmann constant	$\approx 1.38 \times 10^{-23}\,\mathrm{J\,K^{-1}}$
k_{obs}	observed kinetic rate constant	$\mathrm{s^{-1}}$
K_D	equilibrium dissociation constant	M
M_W	polymer molecular weight	Da
N	number of monomers in polymer chain	
N_A	Avogadro number	$\approx 6.022 \times 10^{23}\,\mathrm{mol^{-1}}$
n_b	number of monomers in one blob	
N_B	number of blobs in polymer chain	
P	pressure (force per unit area)	$\mathrm{N/m^2}$
R	polymer end-to-end distance	m
R	sphere radius	m
R_{tip}	AFM tip radius at apex	m

R_F	Flory length	m
R_H	hydrodynamic size	m
RU	SPR resonance units	
s	linear stiffness	N/m
t	time	s
T	temperature	K
U	PSD voltage signal	V
v	excluded volume	m^3
W	interaction energy per unit area	J/m^2
Z	AFM Z piezo position	m
δ	cantilever vertical displacement	m
ξ	polymer blob size	m
σ	surface grafting density	m^{-2}
ϕ	monomer number density	m^{-3}
χ	deflection sensitivity	nm/V

Chapter 1

Introduction

1.1 Motivation: Polymer-functionalized nanoscale systems

Nanopores and nanochannels are emerging as a novel class of materials to mediate transport between reservoirs [1–3]. Channel diameters typically ranging from a few nm to 100 nm approach the dimensions of molecular aggregates or large molecules, which allows for unprecedented control of material flow through the channels. This can be combined with simultaneous sensing of what is going through the pore, especially when pores are functionalized at the entrances and/or within the channel [4].

One versatile and comparably easy way to achieve such a functionalization is the surface grafting of polymers at the pore opening and walls [5]. The conformation of surface-attached polymers is a classical subject in polymer science [6–8]. When polymer chains are tethered to the surface on one end (so-called grafting), they can adopt different conformations, depending on the polymer grafting density. At low enough densities, the individual polymer chains do not interact with each other, and form a "mushroom" at the anchoring point. In the absence of chain–surface interactions, the mushroom size is typically on the order of the unperturbed chain

size in solution. When the grafting distance between individual chains becomes smaller than the mushroom size, the polymer chains will extend away from the grafting surface in order to maximize the favoured interaction of monomers with solvent, i.e. to lower the osmotic pressure within the brush [6, 7, 9]. The stretched layer is called a polymer "brush".

Polymer brushes can make nanopores anti-fouling (i.e. resistant to non-specific adsorption of other particles) [10–13], and by changing the polymer morphology based upon an external stimulus (e.g. temperature, solvent or pH [14, 15]) the flow of solvent and solute through a pore can be regulated [16, 17]. Despite these potential advantages and emerging applications of polymer-functionalized nanopores, direct experimental probing of polymer morphology, interactions and dynamics inside and outside of a nanopore remains a challenge. The detailed knowledge of molecular behaviour of polymers in nanopores and their interactions with material and solvent passing through the pore could aid in improving nanopore characteristics such as selectivity, flux, biocompatibility and fouling resistance, and guide the selection or design of polymers for a desired nanopore functionality.

Further, insights into polymer-functionalized nanopores can help in deciphering the functional transport mechanisms of biological nanopores. For example, the nuclear pore complex (NPC), a pore regulating the transport of molecules in and out of the cell nucleus has similar dimensions but much more sophisticated gating control than current synthetic nanopores [18, 19]. The transport is regulated by intrinsically disordered protein domains which can be likened to polyelectrolytes lining the nanopore walls and filling the central channel. Understanding the behaviour of surface-attached polymers and polyelectrolytes might elucidate also the operating mode of biological analogues such as the NPC, and vice versa learning from biology might bring about further improvements to synthetic nanopore design.

Some experiments have been performed by probing the morphology of polymer

brush-functionalized nanopores or nanopore-like systems via atomic force microscopy [20–22], but mostly treatment of these systems has been limited to theoretical calculations or simulations [23, 24]. These provide interesting hypotheses that are waiting to be experimentally tested. Recent simulations show for example that a nanopore's geometric details influence the confined polymer morphology and functionality non-trivially [16, 25].

More generally, while many experiments probing the mechanics of polymer brushes attached to extended flat surfaces have been carried out [26–30], as well as on 2D-nanopatterned brushes [31], polymers grafted to true 3D nanoscale surfaces have not been measured as often [32].

Moreover, even for polymer brush dynamics on extended flat surfaces open questions still remain, for example about the height of a polymer brush under a constant or oscillatory shear, with some experiments and theory reporting a swelling of the brush and increase of the polymer layer height [33–35], while others predicting a decline of layer height [36] or measuring no height change [27, 37].

1.2   Thesis outline

I continue this chapter by introducing the principles of atomic force microscopy (AFM), the main experimental apparatus used in this thesis. I also explain the fundamentals of polymer theory that apply to our experimental systems and theoretically describe the behaviour of compressed and confined surface-attached polymers.

In chapter 2 I describe the materials and the sample handling, measurement and analysis methods used in this thesis.

Chapter 3 employs various experimental methods to characterize poly(ethylene glycol) (PEG), the polymer of interest in this thesis, in solution and especially when attached to macroscopic and nanopore-like surfaces. I present AFM measurements of a 3D nanoscale system consisting of Au nanorings, functionalized with

PEG which forms a brush on the Au rings. A second similar PEG-functionalized nanohole system is investigated for comparison.

In chapter 4 I investigate how polymer brushes behave when confined by an AFM tip. I compare PEG brush dynamics and morphology at local features provided by our nanoring system, i.e. the flat ring and the nanopore-like central hole regions. When probing the brush by AFM at a range of loading rates (i.e. tip approach velocities), I show that the brush in the pore behaves differently than over the flat area. I further show that depending on the surface density of PEG chains, sudden transitional jumps in the force can occur. These resemble "polymer escape transitions" that have been theoretically described. I analyse the data in this context, comparing experiment to theory.

Chapter 5 demonstrates how intrinsic polymer–protein interactions between PEG brushes on the nanorings and PEG-binding antibodies can be used for sorting specific biomolecules from complex bulk biological fluids to synthetic nanoscale targets. I show how anti-PEG antibodies can bind and ferry cargo to PEG targets which normally do not interact with proteins. Moreover, anti-PEG binding triggers a stimuli-responsive conformational collapse in the PEG brush, thereby imparting an intrinsic "smart" biorecognition functionality to the PEG. I use the AFM to probe the PEG nanomechanics, and fluorescence microscopy to measure the biochemical interactions between proteins and the PEG brush.

Finally, chapter 6 concludes this thesis with a discussion of the work presented here together with an outlook on future directions and opportunities.

1.3   Atomic force microscopy[1]

1.3.1   Basic operation

The essence of the atomic force microscope (AFM) [38] lies with the nanometre-sharp tip or probe that is located at the end of a very sensitive "spring-board"-like cantilever (Fig. 1.1). Attractive or repulsive interactions that act on the tip as it is moved over a surface cause the cantilever to bend, thereby providing a mechanical means to probe local nanoscale effects. This allows for the topographical imaging of surfaces from sub-millimetre scan sizes down to the single molecule [39] or even atomic resolution [40]. Moreover, because the AFM is operational even in liquids, it provides for a direct quantitative measure of surface properties in authentic environments of interest. Beyond imaging, the AFM is also suited to measure intra- and inter-molecular interactions [41]. A bare AFM tip can act as a confining surface that measures the local response of an surface-attached molecular layer, e.g. a polymer brush [20]. Taken together, the AFM is ideal for probing the local properties of a surface with high spatial precision and force sensitivity.

A standard AFM tip has a sharpness (i.e. tip radius) of a few to some tens of nanometres and is fabricated at the free end of a microcantilever. When the AFM tip is close to a surface or in mechanical contact, forces acting on the tip translate into a mechanical deflection of the cantilever, which is detected optically using a laser beam that reflects off the back side of the cantilever (Fig. 1.1). A position-sensitive detector (PSD) in the form of a four-quadrant diode then converts the vertical and horizontal beam deflections into voltage signals, which are continuously recorded.

The high spatial resolution of the AFM is achieved by the ability to control relative positions of cantilever and sample with high accuracy. This is accomplished via piezoelectric crystals, which expand or contract along a preferred axis upon

---

[1]Parts of this section have been published in the following book chapter: Hyotyla J. T., Lim R. Y. H., 2012. *Atomic Force Microscopy (AFM)*. In: J. W. Steed & P. A. Gale, eds. 'Supramolecular Chemistry: From Molecules to Nanomaterials.' pp. 659–668.
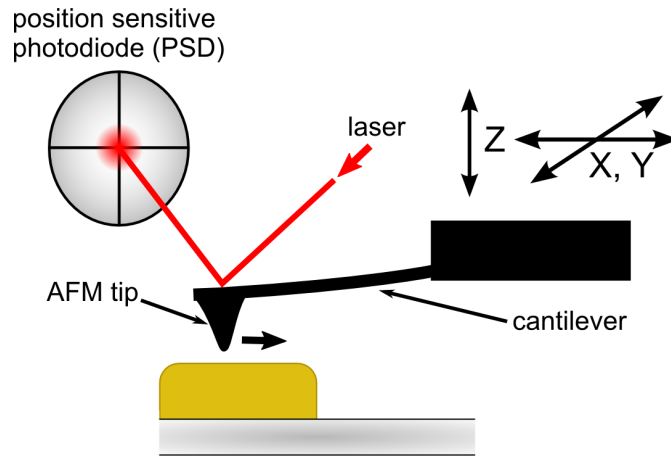
FIGURE 1.1: Schematic illustration of basic AFM operation. Scanning occurs either by translating the cantilever or the sample stage via piezoelectric crystals. A laser reflected from the back of the cantilever measures its deflection.

application of a bias voltage. The use of piezoelectric scanners allows controlling the lateral (denoted X, Y) and vertical (Z) position of the tip and/or sample with sub-nanometre resolution. At this accuracy, raster scanning the sharp tip over the sample results ideally in an image resolution of a few nm and <1 nm in the lateral and vertical directions, respectively.

1.3.2   Imaging modes

The most common mode of AFM operation is to raster-scan the sample with the tip either in constant contact (contact mode imaging) or intermittent contact (tapping mode imaging) with the underlying surface. In contact mode, the sample topography data is collected by feeding the vertical cantilever deflection through a feedback loop into the Z piezo scanner so that the vertical deflection is kept at a constant setpoint. During scanning the feedback loop continuously adjusts the vertical tip position, which ensures constant contact to the sample surface. The topography (i.e. sample height) data is gathered from the position of the Z piezo at each sampling point. In tapping mode, the cantilever is typically oscillated near its resonance frequency, which allows the tip to continuously "tap" the sample surface. The PSD detects the amplitude of the oscillation, which is determined

mostly by the average distance of the tip to the sample and is used as the feedback loop setpoint variable.

1.3.3 Force spectroscopy

Most of the AFM data about polymer brush morphology and dynamics in this thesis has been obtained using force spectroscopy. Fig. 1.2 illustrates the principle. The AFM cantilever is vertically ramped towards and away from the sample (called approach and retract phases) as its lateral position is kept constant. During ramping the cantilever deflection and its Z position are constantly recorded. Since the cantilever deflection relates to the force acting on the tip, we obtain a force curve, $F(d)$ with the force F plotted against the distance between sample substrate and tip (tip-sample distance d). See Methods, section 2.2.6 for details about transforming the cantilever deflection into a calibrated force.
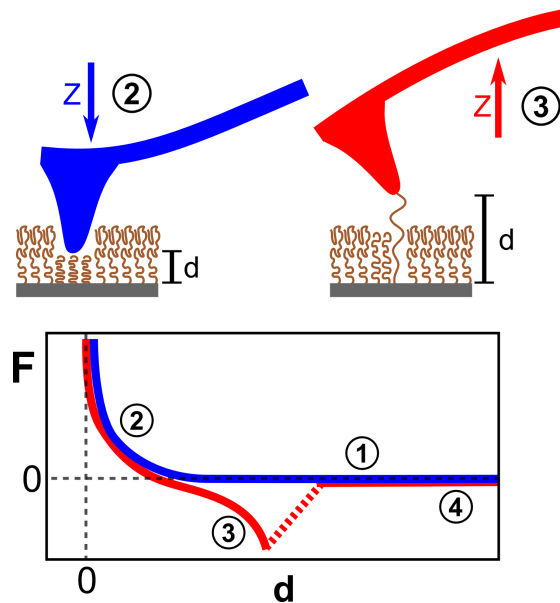
FIGURE 1.2: Demonstrating the principle of force spectroscopy. While the cantilever is ramping in Z-direction towards (approach; top left) and away from the sample (retract; top right), the force acting on the tip is recorded (bottom). See text for explanation of the numbered force curve segments.

Typically a force curve consists of the following segments (Fig. 1.2): (1) During initial approach of the tip towards the sample surface, no force is acting on the cantilever ("free cantilever"). (2) Upon contact with the sample, forces acting

on the tip (here, a polymer brush resisting compression by the tip) cause the cantilever to bend and an increasing force to be recorded. (3) After moving a desired distance or reaching a defined force, the cantilever movement reverses to retract from the sample. If the sample is elastic, initially the retraction force curve tracks the approach data, but if parts of the sample (here, a polymer chain) adheres to the tip, a negative force (downwards bending of the cantilever) is recorded. (4) Once the cantilever bending force exceeds the adhesion force, the tip snaps off the surface and the cantilever returns to a free state. At this point the ramp cycle is repeated. If desired, the cantilever is moved laterally to a new position before ramping again.

Force spectroscopy is very versatile because the complete time- and distance-resolved interaction between the tip and the sample is available. Based on this, various parameters of interest can be extracted, such as the height and stiffness of a polymer brush (see Methods, section 2.2.6). Further, by changing the speed of ramping, dynamic interaction forces can be accessed, as we show in chapter 4.

1.4   Polymers in solution and at surfaces

1.4.1   Polymer sizes in solution

For linear polymers in solution, we can define a characteristic length scale R, which is the radius of the spherical volume that is occupied by the polymer. For real polymers, the volume filled by the polymer depends on the relative contributions of each monomer's interaction with the solvent and with other monomers, the so-called excluded volume interactions. The excluded volume v is a single parameter that summarizes the net two-body interaction between monomers [42]. It includes the short-range hard-core repulsion between monomers (which gives a positive contribution to v) as well as any attractive longer-range interactions between the monomers (which reduce v). We can then distinguish between solvent regimes

based on the excluded volume which lead to different polymer coil sizes in solution: (1) In *good solvents* there is only a small contribution of monomer-monomer attraction, leading to a large v, and the polymer is in a well-swollen state (i.e. "the polymer likes to interact with solvent molecules"). (2) At *theta conditions* (θ), the negative and positive contributions to v cancel out, and the chain behaves like an ideal chain with random-walk (Gaussian) statistics. Since the excluded volume depends also on temperature, there is only a single theta point for a given polymer–solvent combination. (3) In *bad solvents*, the monomer–monomer attraction outweighs, and we get a negative v which signifies an effective attraction of monomers. Polymers in bad solvents collapse unto themselves.

The Flory theory is a simple successful theory for polymer coil sizes in solvents. The Flory theory calculates the size of a polymer chain by balancing the energetic and entropic contributions to the free energy of a chain [42]. The excluded volume effect described above tends to energetically swell a polymer chain in good solvents, while the loss of entropy of a stretched chain contributes a free energy term in the other direction. Free energy minimization with respect to the coil volume leads to a Flory length $R = R_F$ of the chain, with the number of monomers N, and the monomer size a:

$$R_F \approx a N^{3/5} \; . \tag{1.1}$$

The operator $\approx$ means here and for the rest of this chapter that we leave out numerical prefactors of order unity, which depend here on the solvent quality. This is good enough to extract general scaling behaviours. In comparison, an ideal chain (no intermolecular interactions, e.g. theta solvent) leads to a different power law:

$$R \approx a N^{1/2} \; . \tag{1.2}$$

1.4.2   Polymers attached to surfaces

Surface-attached (grafted) polymers exhibit unique physicochemical properties that regulate diverse interfacial phenomena in a wide variety of areas ranging

from tribology, colloidal stability and biology [43–45] to nanopores [25].

The conformation of polymer chains grafted at one end to a surface (e.g. covalently attached) depends on the surface grafting density σ, or equivalently to the average grafting distance between two chains, $g = \sigma^{-1/2}$. We can apply scaling considerations, using the so-called blob picture, to understand the resulting polymer morphologies [7, 8, 42, 46]. This method gives correct predictions up to numerical prefactors of order unity. A blob is a correlation element of size ξ in a polymer chain. Within a blob, the polymer chain behaves randomly, while at distances larger than ξ, the chain conformation is not random. The energy scale associated with a blob is $k_B T$, with k_B being the Boltzmann constant and T the temperature. For polymer chains in good solvents, $\xi = R_F$, i.e. the chain forms a single random coil blob.

At grafting distances $g > R_F$, the surface-attached chains behave mostly as in solution, i.e. they form a single blob of size R_F, a *mushroom* (Fig. 1.3a). When grafting distances become smaller than R_F, the polymers start to repel each other and form a stretched layer of blobs of size $\xi = g$, a *polymer brush* (Fig. 1.3b). In this Alexander–de Gennes model, the brush has uniform density up to its height h after which it drops to zero (i.e. the brush density is a step function).

The height of the brush can then be estimated by applying a Flory-type argument of two competing free energy terms. The first term, f_{stretch}, describes the entropic cost of stretching an ideal chain to length h. The second term, f_{volume}, describes the real chain excluded volume energy cost of overlapping monomers.

A polymer chain in the brush consists of $N_b = h/g$ number of blobs. The entropic cost of a stretched chain is on the order of $k_B T$ per blob:

$$f_{\text{stretch}} \approx k_B T N_b = k_B T \frac{h}{g} \; . \tag{1.3}$$

Within a blob, the sub-chains follow ideal chain statistics, so a blob contains n_b subunits with $n_b \approx g^2/a^2$ (Eq. 1.2). With this, the height of the brush can be
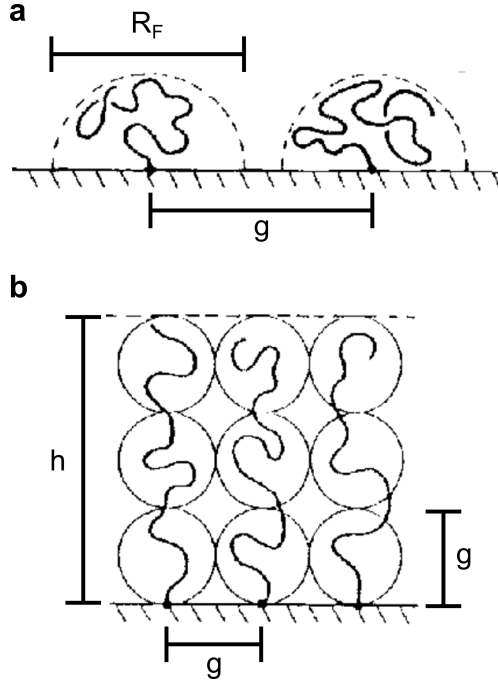
FIGURE 1.3: Blob picture of polymers covalently attached to a surface. **(a)** At large enough grafting distances $(g > R_F)$, polymer chains form mushrooms of size $\sim R_F$. **(b)** As grafting distances are decreased $(g < R_F)$, polymer chains are forced to form smaller blobs of size g, thereby extending to a brush of height h. Adapted from *Advances in Colloid and Interface Science*, 27, P.G. de Gennes, 'Polymers at an interface, a simplified view', 189-209, Copyright (1987), with permission from Elsevier [8].

expressed as

$$h \approx g N_b = g \frac{N}{n_b}$$
$$\approx \frac{Na^2}{g} \tag{1.4}$$

and by combining with Eq. 1.3 we get

$$f_{\text{stretch}} \approx k_B T \frac{h^2}{Na^2} \ . \tag{1.5}$$

The excluded volume cost is on the order of $k_B T$ per monomer overlap. The number density of monomers in the brush is

$$\phi \approx N \frac{\sigma}{h} \tag{1.6}$$

and the probability of a second monomer being in the excluded volume of a given monomer is $v\phi$. The excluded energy term is then

$$f_{\text{volume}} \approx k_B T N v \phi$$
$$\approx k_B T N v \frac{N\sigma}{h} \tag{1.7}$$

which leads to the following free energy equation for a polymer brush with a step-like profile:

$$f_{\text{tot}} = f_{\text{stretch}} + f_{\text{volume}}$$
$$\approx k_B T \left(\frac{h^2}{Na^2} + v\frac{N^2\sigma}{h} \right) \ . \tag{1.8}$$

Minimizing f_{tot} with respect to h yields the scaling prediction for the brush height (prefactors have been left out):

$$h \sim N(v\sigma)^{1/3} \ . \tag{1.9}$$

We immediately see that the brush height scales with N, compared to $N^{3/5}$ for free chains in solution. This means that brushes can become much longer than the unperturbed size of a polymer chain. At not too high grafting densities, the excluded volume parameter v can be neglected and the scaling with regards to grafting density relation becomes $h \sim \sigma^{1/3}$, but at high densities the excluded volume effects play a larger role and experimentally scaling relations up to $h \sim \sigma^{0.6}$ have been measured [47]. Self-consistent mean field calculations and experiments have revealed that the brush density profile is not step-like but rather parabolic, i.e. with gradually decreasing density at larger distances from the surface [48]. Brush height calculations using such a density profile still show the same scaling as predicted by the Alexander–de Gennes free energy balance derived above.

1.4.3 Confinement of surface-attached polymer brushes

Because confinement of a brush displaces the polymer from its energetic minimum, a force resisting the confinement will result. The compression of polymer brushes by infinite planes has been calculated theoretically, and the compression of surface-attached polymers by macroscopic obstacles is accurately experimentally accessible via surface force apparatus measurements [49–51].

Based on the step-like Alexander–de Gennes profile and by postulating no inter-penetration of chains, de Gennes calculated the force needed to push two parallel plates functionalized with polymer brushes towards each other [8]. For infinite plates, the force per unit area (i.e. pressure $P(d)$) as a function of the inter-plate distance d is:

$$P(d) = \frac{k_B T}{g^3} \left[\left(\frac{2h}{d} \right)^{9/4} - \left(\frac{d}{2h} \right)^{3/4} \right] \qquad d < 2h \qquad (1.10)$$

where h is the brush height per plate. The Derjaguin approximation [51, 52] relates the interaction energy per unit area $W(d)$ between two parallel plates at distance d to the force between a sphere and a plate, $F(d)$, at the same distance:

$$F(d) = 2\pi R W(d) \qquad (1.11)$$

where R is the sphere radius. With

$$W(d) = \int_d^\infty P(x) \, \mathrm{d}x \qquad (1.12)$$

we can express Eq. 1.10 in terms of the force required by a polymer brush-coated sphere pushing on a brush-coated plate:

$$F(d) = 2\pi R \frac{k_B T}{g^3} \int_d^{2h} \left[\left(\frac{2h}{x} \right)^{9/4} - \left(\frac{x}{2h} \right)^{3/4} \right] \mathrm{d}x \ . \qquad (1.13)$$

An AFM tip can be regarded as sphere-like at the very apex. Since the polymer chains do not interpenetrate, we can convert the calculated force to apply to a

bare AFM tip pushing on a polymer-brush functionalized surface by replacing $2h$ with h and dividing F by 2 [26]. The final expression is then:

$$F(d) = \frac{8\pi}{35} R_{\text{tip}} k_B T \frac{h}{g^3} \left[7 \left(\frac{h}{d} \right)^{5/4} + 5 \left(\frac{d}{h} \right)^{7/4} - 12 \right] \tag{1.14}$$

where R has been replaced by R_{tip}, the AFM tip radius at the apex.

For $d/2h$ in the range of 0.2 to 0.9 the AdG equation (Eq. 1.10) has an exponential form and can be approximated by [51]:

$$P(d) \approx \frac{100}{g^3} k_B T \mathrm{e}^{-\pi d/h} . \tag{1.15}$$

By applying the Derjaguin approximation and reducing to the form of a bare AFM tip pushing on a polymer brush-functionalized surface following the steps above, we get:

$$F(d) = R_{\text{tip}} \frac{50h}{g^3} k_B T \mathrm{e}^{-2\pi d/h} \qquad 0.2 < d/h < 0.9 . \tag{1.16}$$

As the step-like AdG brush profile is not realistic, Milner–Witten–Cates (MWC) developed a pressure expression analogous to the AdG one with a parabolic brush profile [48]:

$$P(d) = \frac{P_0}{h} \left[\ln \left(\frac{d}{2h} \right) + 2 \left(\frac{d}{2h} \right) - \left(\frac{d}{2h} \right)^4 \right] \tag{1.17}$$

with

$$P_0 = \frac{k_B T N}{2} \left(\frac{\pi^2 a^4}{12} \right)^{1/3} g^{-10/3} \tag{1.18}$$

where N and a are the number of monomers and the monomer size. With the Derjaguin approximation applied and the transformation for a bare AFM tip pushing on a surface with a polymer brush, we get:

$$F(d) = \pi R_{\text{tip}} k_B T N \left(\frac{\pi^2 a^4}{12} \right)^{1/3} g^{-10/3} \left[\frac{h}{d} + \left(\frac{d}{h} \right)^2 - \frac{1}{5} \left(\frac{d}{h} \right)^5 - \frac{9}{5} \right] . \tag{1.19}$$

The AdG and the MWC equations lead to very similar force profiles at intermediate to high compression, and have been verified by using two functionalized mica

sheets pushing on each other in a surface force apparatus [53] and by colloidal probe AFM (where the sharp tip has been replaced by a µm-sized colloid) [28]. At large separations, i.e. small forces, the MWC formula gives more accurate results when compared to experiments than the AdG model. This is to be expected, since it is exactly at weak compression where the difference between a step and a parabolic profile will play a role.

1.4.4 Polymer escape transition

When the compression of a polymer mushroom by a finite obstacle or piston of size on the order of the polymer was first considered theoretically based on scaling theory, some interesting behaviour emerged [54–56]. If the compressing piston radius is larger than the mushroom size but smaller than the contour length of the polymer, two distinct chain conformations will occur, with a sudden transition between them. For weak compression, the complete chain stays confined under the piston. Scaling considerations predict $F(d) \sim d^{-8/3}$ in good solvent, where $F(d)$ is the force needed to compress the mushroom at distance d from the grafting surface (Fig. 1.4a). For strong compression, below a critical distance, it becomes energetically favourable for a stretched tether to form up to the piston edge, and for the rest of the chain to form an unconfined random coil outside the compressing piston (Fig. 1.4b). The stretched tether expends conformational energy which is however more than offset by the release of the rest of the chain from confinement. Here the predicted force relationship is $F(d) \sim d^{-2}$. Between the two states a first-order transition occurs (i.e. a discontinuous jump in force).

This polymer escape transition has been confirmed by further theoretical calculations and with simulations at theta conditions [57] and in good solvents [58–60]. The escape transition has been compared to similar transitions for polymers adsorbing from solution and for polymers in repulsive potentials [61–63]. The escape transition has also been described for more complex polymer chains, such as block copolymers [64] and star polymers [65, 66]. Simulations at finite temperatures
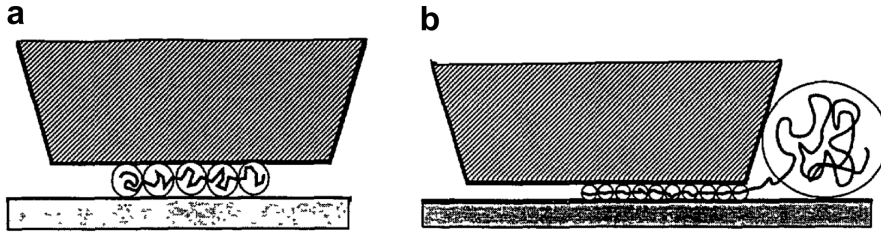
FIGURE 1.4: **(a)** A polymer chain that is compressed under a flat obstacle breaks down into a number of independent blobs, each blob having the size on the order of the distance between the two confining surfaces. **(b)** As the chain is further compressed, the chain escapes from beneath the obstacle. The resulting stretched tether together with a large blob outside the obstacle is energetically more favourable than the fully confined configuration. Adapted from Ref. [55].

show that the sharp transition can become "smeared out" or even disappear completely especially for short chains because the chain is able to easily move between confined and escaped states.

AFM, having a sharp tip as a probe not much larger than single polymer coils, was recognized early as a potential way to probe these escape transitions experimentally, and so several works have calculated or simulated the escape under more realistic "AFM-like" conditions, i.e. different tip shapes and off-centre compression [67–69]. These confirm the predicted scaling laws even in less idealized systems, but also show a possible smearing of the transition.

So far no experimental work exists to our knowledge which measures the force response of a single compressed polymer chain. This might be due to the difficulty of obtaining such high spatial and force resolutions needed to probe a single mushroom. It is easier to prepare and measure a surface functionalized with a polymer brush. Some theoretical works have addressed a finite obstacle compressing a polymer brush in the context of escape transitions. One molecular dynamics simulation in good solvent shows that chains escape under a compressing tip, but no first-order transition is visible in the force [70], while another simulation under theta conditions finds a visible transition between confined and escaped chains [71].

Even for polymer brush systems only a few experimental works address the polymer escape transition. Compression of polyethylene glycol (PEG) / polystyrene

brushes was shown to exhibit abrupt transitions in force near the grafting surface [26], but the measurements pre-date the theoretical discussions of escape transitions and the authors only talk about a "jump into contact". A different experiment combining AFM and electrochemical measurements to probe PEG mushrooms shows no transitions in force, but the electrochemical data indicates an escape of the polymer when highly compressed [72].

1.5 Poly(ethylene glycol)

The polymer of choice in this work is poly(ethylene glycol) (PEG)[2], specifically its derivative methoxy-PEG-thiol (mPEG-SH) which is terminated by a methoxy group (CH_3-O) at one end and a thiol group (SH) on the other end. The chemical formula of mPEG-SH is $H_3C-O[-CH_2-CH_2-O]_n-CH_2-CH_2-SH$ (Fig. 1.5). The thiol end group provides a means to covalently attach the PEG to Au surfaces, and the methyl keeps the other end of the chain inert by not exposing an oxygen. PEG itself is a hydrophilic polymer.
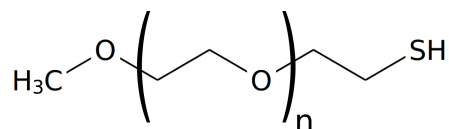
FIGURE 1.5: Chemical formula of methoxy-PEG-thiol (mPEG-SH), the PEG derivative used in this thesis for covalent attachment to Au surfaces via the thiol group.

The driving impetus to use PEG lies in its unique properties that can be harnessed technologically. PEG is biocompatible, i.e. it does not elicit a strong immune response in the body [73]. PEG is also highly antifouling, i.e. it prevents adsorption of proteins and other macromolecules from solution to PEG-coated surfaces [29, 74]. These extraordinary characteristics stem from the strong hydration properties of PEG [75]. The PEG backbone participates in the water molecule hydrogen

---

[2]PEG is sometimes also referred to as poly(ethylene oxide), PEO.

bonding [76, 77]. This strong interaction with water adds energy costs to adsorption of macromolecules, leading to their rejection from the vicinity of PEG and thus to the antifouling and nonimmunogenic properties.

Due to its anti-fouling properties, PEG is widely used for surface passivation. PEG-coated filtration membranes show a reduction in fouling [78]. Surfaces functionalized with PEG prevent adhesion of cells and bacteria, making them a candidate for protecting medical implants [79–81]. The biocompatibility of PEG also has lead to its use in drug development. PEG modification of some proteins inhibits an immune response against them, in contrast to unmodified proteins [82]. PEG is the most used polymer for this so-called "stealth" behaviour [83, 84].

The abovementioned features and its use in technological and medical applications, together with the ease of handling and ready commercial availability make PEG an interesting polymer to investigate. Particularly in chapter 5 we make use of the PEG antifouling characteristics to reject unspecific proteins from nanoscale targets while allowing specific interactions to provide exclusive access to the PEG-protected samples.

Chapter 2

Materials and Methods

2.1 Materials

2.1.1 Au nanorings

Arrays of 20×20 gold nanorings were fabricated by electron beam lithography (EBL) and subsequent evaporation on $0.17\,\mu\text{m} \pm 0.02\,\mu\text{m}$ thick standard microscopy cover glass slides (round, $24\,\text{mm}$ diameter; Karl Hecht Assistent, Germany). Each sample was cleaned by ultrasonicating in acetone and isopropanol (IPA), followed by thorough rinsing with deionized (DI) water and drying with N_2 gas. $950\,\text{kDa}$ poly(methyl methacrylate) (PMMA) was spin-coated at $5000\,\text{rpm}$ onto the substrate to create a $350\,\text{nm}$ thick polymer resist layer for EBL. After the coating, the samples were placed into an oven and baked for $15\,\text{min}$ at $170\,^\circ\text{C}$. After preparing the resist layer, EBL was performed with an Elionix ELS-7000 (Elionix, Japan) EBL system. The nanostructure patterns were written at a dose of $800\,\mu\text{C/cm}^2$ by using an electron beam with acceleration voltage of $100\,\text{kV}$ and a beam current of $20\,\text{pA}$. After exposure, the samples were developed in a solution of 3 parts IPA and 1 part methyl isobutyl ketone (MIBK) for $70\,\text{s}$, followed by rinsing in IPA and DI water for $20\,\text{s}$ and drying with N_2. An adhesion layer of $\sim5\,\text{nm}$ Cr followed by $\sim30\,\text{nm}$ Au was deposited on the samples by thermal

evaporation. The lift-off was performed by soaking in acetone for 10 min and final rinsing in acetone, IPA and DI water, followed by drying the sample with N_2.

Two different nanoring geometries were used in this work. Structures with nominal dimensions of 400 nm and 100 nm for the outer and the inner diameter of the rings were used unless otherwise mentioned (also denoted rings with *large central holes*). For experiments in chapter 4 additionally nanorings with outer and inner diameters of 400 nm and 50 nm were fabricated (denoted rings with *small central holes* for disambiguation). For both samples the distance between individual nanorings was chosen as 1.3 μm so that neighbouring nanorings did not interact with each other.

2.1.2   Solutions

Deionized water (DI H_2O) was obtained from an in-house system (Barnstead Nanopure, Thermo Scientific; 18.2 MΩ cm resistivity). Phosphate-buffered saline (PBS) with 1.5 mM KH_2PO_4, 2.7 mM Na_2HPO_4, and 155.2 mM NaCl, pH 7.2, was obtained from Invitrogen (USA). Bovine serum albumin (fraction V; A9647, Sigma-Aldrich, USA) was dissolved in PBS to obtain a 1 % BSA solution (10 mg/ml), used for the SPR BSA height determination (chapter 3), and as passivating molecules for fluorescence measurements (chapter 5). Rabbit serum was obtained from Eurogentec (Belgium). A 5 μl amount of 1 M Tris-buffer, pH 8, was added per 100 μl of serum. NaOH solutions were prepared by dissolving NaOH in DI water to obtain the appropriate concentration.

2.1.3   Poly(ethylene glycol) (PEG)

Thiolated methoxy-terminated PEG (mPEG-SH) with molecular weights of 5 kDa, 10 kDa and 20 kDa (average monomer numbers of 114, 228 and 455, respectively) was obtained from Laysan Bio, USA. Incubation solutions for the experiments were prepared by dissolving the desired amount of mPEG-SH in the incubation solvents (H_2O, PBS, or 0.6 – 0.9 M Na_2SO_4 in PBS, as described in the results)

and agitating vigorously for 20 s. PEG cloud point concentrations were identified by dissolving a large amount of PEG in the desired Na_2SO_4 solvent, and gradually diluting the PEG solution until the appearance switched from cloudy to transparent. Cloud point concentrations for 5 kDa, 10 kDa and 20 kDa mPEG-SH identified this way were 0.83 mg/ml, 0.36 mg/ml and 0.15 mg/ml in 0.9 M Na_2SO_4, respectively, and additionally 0.3 mg/ml and 9.0 mg/ml for 20 kDa PEG in 0.7 M and 0.6 M Na_2SO_4, respectively.

2.1.4 Antibodies

Monoclonal mouse IgG_1 antibodies against PEG (E11, anti-PEG) [85] were covalently labelled at the N-terminus with Alexa Fluor 488 5-SDP ester (A30052, Invitrogen, USA) for 2 h at room temperature with a 10× molar excess of dye according to the manufacturer's protocol. UV/vis spectrophotometry indicated a labelling efficiency of ∼1 dye molecule per antibody by comparing absorbance at 280 nm (protein) and 494 nm (dye) after purification of the labelled anti-PEG. Cy3-labelled polyclonal donkey anti-mouse (715-165-151, Jackson Immunoresearch, USA) and Cy5-labelled polyclonal donkey anti-rabbit (711-175-152, Jackson Immunoresearch) were used as the specific and unspecific IgG, respectively. UV/vis showed ∼1 dye molecule per antibody for both.

2.2 Methods

2.2.1 Sample cleaning

All grafting surfaces, i.e. surface plasmon resonance chips, Au nanoring and Au nanohole samples, used in this thesis were cleaned as following. Samples were ultrasonicated in acetone and isopropanol (IPA) for 20 min each and dried in an N_2 stream, followed by exposure to UV-Ozone (Model 42A-220; Jelight, USA) for 45 min.

The samples were further cleaned in RCA1 solution[1]. RCA1 solution was prepared by mixing 6 parts H_2O with one part NH_4OH ($\sim$30 %), and heating the solution to 65 °C. After reaching 65 °C, the solution beaker was removed from the heating plate, and one part H_2O_2 (30 %) was added. In our case, the solvent volumes were 50 ml : 8.3 ml : 8.3 ml of H_2O : NH_4OH : H_2O_2. After waiting for 2 min, the samples were then immersed into the RCA1 solution for 10 min.

We note that usually RCA1 is prepared with a 5:1:1 ratio, but in our case this proved too harsh, damaging the nanostructures on our samples. A slightly less aggressive ratio was chosen, and no loss in cleaning quality was observed. By using RCA1 cleaning, even already functionalized samples could be returned to an unfunctionalized, bare Au state. For measurements in chapter 5, RCA1 cleaning was not used, since only freshly produced nanoring samples were used in the experiments.

Finally, the samples were rinsed with H_2O, and finally ultrasonicated in Ethanol for 30 min. After drying in an N_2 stream, the sample functionalization was started immediately.

2.2.2   Nanostructure functionalization

Nanostructures (Au nanoring and Au nanohole arrays) were functionalized by covalently attaching mPEG-SH to Au surfaces via the thiol group. To achieve this, the samples were incubated in mPEG-SH containing solution at the desired concentration immediately after cleaning. For high-concentration PEG solutions (>10 mg/ml in H_2O and PBS), a drop of $\sim$60 µl PEG solution was placed on top of the nanostructures and left to incubate in darkness at room temperature. For lower concentrations (solutions containing Na_2SO_4), the samples were immersed in the PEG solutions in a beaker and incubated in darkness at room temperature while gently shaking the beaker. Incubation was carried out for 14 – 24 h, after

---

[1]RCA1 and its constituent solvents are hazardous. Adhere to the appropriate safety measures when preparing and handling RCA1.

which the samples were ultrasonicated for 10 s, rinsed in DI water and dried in a stream of N_2 gas. The samples were then used immediately for measurements.

2.2.3 PEG characterization by dynamic light scattering

Dynamic Light Scattering (DLS) measurements were performed using a Zetasizer Nano instrument (Malvern, UK). To measure the 20 kDa mPEG-SH hydrodynamic size in good solvent, 5 mg/ml was dissolved in PBS. To measure the PEG size at cloud point conditions, 0.13 mg/ml mPEG-SH was dissolved in PBS with 0.9 M Na_2SO_4. The samples were centrifuged at $16\,000 \times g$ for 15 min just before the measurement to degas them and to precipitate any dust or aggregate particles. Three measurements per condition were performed and averaged, each measurement consisting of 10 runs with 50 s acquisition time each. The measurements were done at 25 °C, the input parameters into the analysis were viscosity 0.9074 cP and refractive index 1.332 (values for PBS). The hydrodynamic size was calculated in a standard manner by the DLS machine manufacturer's software from the intensity distribution fit to the correlation curves, while making sure that the number distribution fit showed >99 % of molecular species being at said size.

2.2.4 Surface plasmon resonance (SPR)

Surface Plasmon Resonance (SPR) measurements were performed at 25 °C with a Biacore T100 instrument (GE Healthcare Life Sciences). "SIA Kit Au" (GE Healthcare) bare Au SPR sensor chips were used for measurements. Sensor surfaces were cleaned (see section *Sample cleaning* above) and mounted on the SPR chip holder for immediate usage. The PBS running buffer was filtered and degassed using filterware of 0.2 µm pore size. All samples used in SPR measurements were centrifuged at $16\,000 \times g$ for 15 min just before loading the samples into the machine to degas them and to precipitate any dust or aggregate particles.

Grafting density measurements

For PEG grafting density measurements, the sensor surface was incubated with the desired concentration and solvent at a flow rate of $5\,\mu l/min$ for 30 min. After incubation, PBS was injected into the flow cell and the amount of bound PEG was measured (in Resonance Units, RU). From the RU signal, the average distance between two PEG grafting sites can be calculated with the following equation [86, 87]:

$$g_{\mathrm{SPR}} = \sqrt{\frac{1000 \cdot M_W \cdot 10^{21}}{N_A \cdot \mathrm{RU}}} \qquad (2.1)$$

where g_{SPR} is the average grafting distance in nm, M_W is the PEG molecular weight in Da, and N_A the Avogadro number. This formula uses the relation $1000\ \mathrm{RU} = 1\,\mathrm{ng/mm^2}$.

Brush height measurements

SPR was used to measure the brush height of the surface-grafted PEG brush by using non-interacting molecules as probes of layer height as described by Schoch and Lim [86]. One flow cell of the SPR machine was used as a reference cell and blocked with (ethylene glycol)$_3$−undecane−thiol (EG$_3$−U−SH; chemical formula HO−(CH$_2$CH$_2$O)$_3$−(CH$_2$)$_{11}$−SH, Nanoscience). EG$_3$−U−SH was prepared by diluting the stock solution to 10 mM with ethanol, and further diluting to 1 mM with PBS. The reference cell was incubated with EG$_3$−U−SH for 30 min at a flow rate of $2\,\mu l/min$. mPEG-SH was grafted to three other cells, as described above. After incubation of reference and sample cells, Bovine Serum Albumin (BSA) was injected into all cells as non-interacting probes. Each BSA injection lasted for 30 s at a flow rate of $10\,\mu l/min$, with 1 min PBS flow in between BSA injections. First, 5 sequential BSA injections were performed to equilibrate the system, then 3 injections to measure the height of the molecular surface layer.

From the SPR response of the BSA injections, the brush height in the main cell, d_{sample}, can be calculated [86]:

$$d_{\text{sample}} = \frac{l_d}{2} \ln\left(\frac{R_{\text{ref}}}{R_{\text{sample}}}\right) + d_{\text{ref}} \qquad (2.2)$$

where l_d is the surface plasmon wave decay length into the sample medium, R_{ref} is the SPR response of the reference cell during BSA injection, R_{sample} the response in the sample cell, and d_{ref} is the layer height in the reference cell. Following the calculations described in Schoch and Lim [86], we used $l_d = 292\,\text{nm}$ and $d_{\text{ref}} = 2\,\text{nm}$. Fig. 2.1 shows in a schematic way how the SPR height measurement is performed and how the non-interacting BSA molecules modulate the SPR signal from which the molecular layer height can then be calculated.
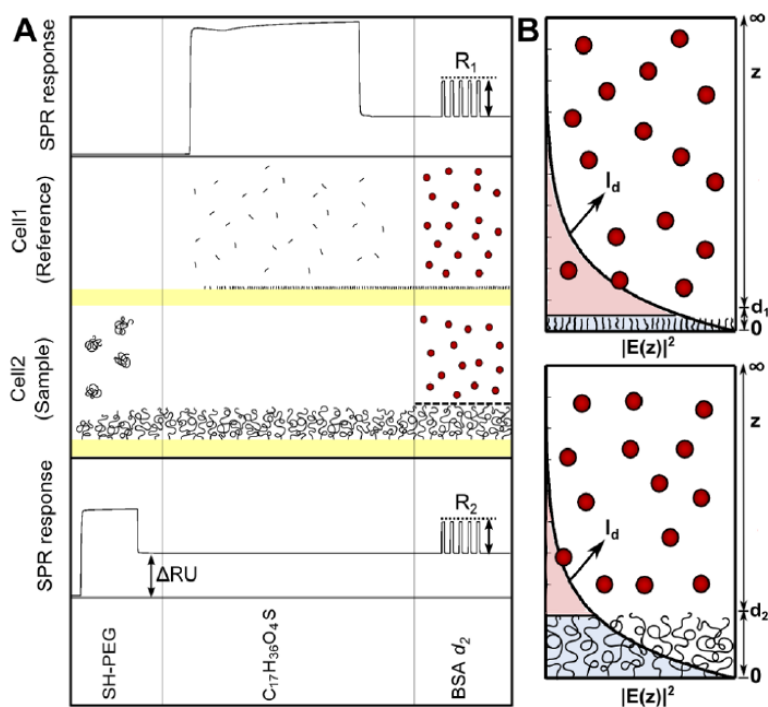
FIGURE 2.1: **(a)** Schematic measurement procedure of a polymer layer height (d_2) using SPR with a sample and a reference cell. **(b)** SPR signal (exponentially decaying evanescent wave above the Au surface) arising from injected BSA molecules (red area) over the reference and sample cells, from which the brush height (blue area) in the sample cell can be calculated. Reprinted with permission from *Langmuir*, 29, R. L. Schoch and R. Y. H. Lim, 'Non-interacting molecules as innate structural probes in surface plasmon resonance', 4068-4076, Copyright (2013) American Chemical Society [86]

2.2.5   Atomic force microscopy (AFM)

All AFM measurements were done on a Bioscope Catalyst or Bioscope 2 AFM
with a Nanoscope V controller, running the Nanoscope version 8 (Catalyst) or
7 (Bioscope 2) control and acquisition software (Bruker, USA). Technical differ-
ences between the two AFM systems were negligible regarding our measurements.
The AFMs were part of a combined setup integrated with a commercial optical
fluorescence (TIRF) microscope (see section *Fluorescence measurements*, p. 38).
All experiments were performed in PBS unless otherwise noted. Samples were
mounted on the AFM immediately after cleaning (see section *Nanostructure func-
tionalization*, p. 22). The cantilever was mounted on the AFM and equilibrated
together with the sample for ca. 1 h before use. Fig. 2.2 shows a schematic of the
combined AFM and TIRF setup probing an Au nanoring in buffer.
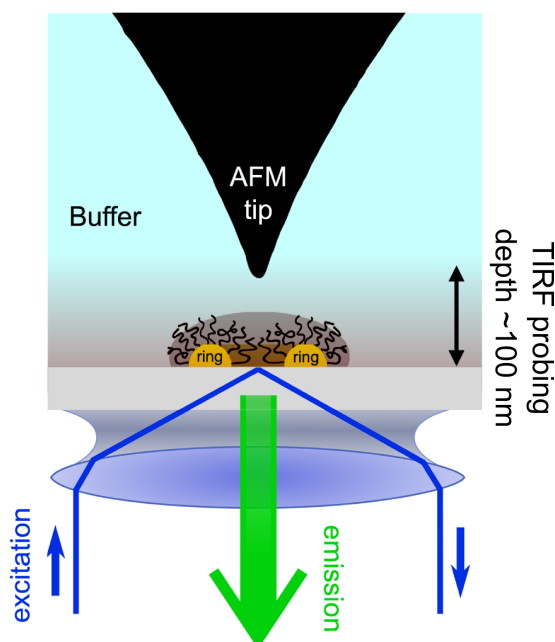
FIGURE 2.2: Schematic of the combined AFM and TIRF setup probing a Au
nanoring in buffer.

Cantilever calibration

In order to accurately measure interaction forces with the AFM, careful calibration
of the cantilever is important. The cantilever can be regarded as a spring obeying

Hooke's law, and so its deflection is described by

$$F = k \cdot \delta \tag{2.3}$$

where F is the normal force acting on the cantilever, δ is the vertical displacement of the cantilever from its equilibrium position, and k is the cantilever spring constant. As the cantilever is bent by an applied force acting on the tip at the end of the cantilever, the laser light reflection angle changes and the laser spot moves across the position-sensitive detector (PSD). We introduce a calibration factor, the deflection sensitivity χ,

$$\chi = \delta / \Delta U \tag{2.4}$$

which relates the voltage change in the PSD signal (ΔU) to the corresponding linear displacement δ of the cantilever tip. By combining this with Eq. 2.3 we obtain an expression for the force acting on the cantilever which can be calculated from the change of the vertical displacement voltage signal:

$$F = k \cdot \chi \cdot \Delta U . \tag{2.5}$$

Accurate force values can be obtained once χ and k are calibrated.

To calibrate the deflection sensitivity χ, the cantilever was ramped on the hard unfunctionalized glass surface of a sample and the voltage signal vs Z piezo movement, $U(Z)$, was recorded. As the tip cannot penetrate into the glass, any movement of the (calibrated) Z piezo downwards must correspond to a deflection of the cantilever upwards by the same distance. χ is calibrated by fitting this linear part (when the cantilever is in contact with the glass) of $U(Z)$ with a linear fit. The inverse slope of this fit is then

$$\Delta Z / \Delta U = \delta / \Delta U = \chi . \tag{2.6}$$

The deflection sensitivity was measured and averaged from at least three different positions $\sim 1\,\mu\mathrm{m}$ apart, and was re-calibrated any time a new cantilever was mounted or the laser spot was moved relative to the cantilever.

The cantilever spring constant, k, was calibrated using the thermal tune method [88, 89]. This well-established method of calibration was provided by the controller and software of our AFMs. In short, the thermal tune method uses the approximation of the cantilever as an ideal harmonic oscillator. Then, by the equipartition theorem,

$$\left\langle \frac{1}{2} m \omega_0^2 \delta^2 \right\rangle = \frac{1}{2} k_B T \tag{2.7}$$

where the brackets denote the time averaged value, m is the oscillator mass, $\omega_0 = \sqrt{k/m}$, k_B the Boltzmann constant, and T the temperature. We can simplify this equation to

$$k = \frac{k_B T}{\langle \delta^2 \rangle} \ . \tag{2.8}$$

$\langle \delta^2 \rangle$ can be found by measuring the noise spectrum of a free cantilever, performing a power spectral density analysis on the data and integrating the area under the first resonant peak in the spectrum (as higher resonances don't contribute much to the cantilever energy). The integrated power equals the time averaged cantilever displacement $\langle \delta^2 \rangle$ and can be used to calculate the spring constant from Eq. 2.8. Additional correction factors need to be added to account for deviations from the ideal harmonic oscillator picture [89]. In our experiments, the spring constant was calibrated once for each new cantilever, before starting the measurements.

Cantilevers

Biolever cantilevers (OBL type B, Bruker) were used for all measurements (for exceptions see below). OBL(B) are rectangular Si_3N_4 cantilevers, coated with Au on all sides, with length, width and thickness of $\sim 100 \, \mu m$, $\sim 30 \, \mu m$ and $\sim 0.18 \, \mu m$ (manufacturer's specifications). The tip is a vertically bisected pyramid with $\sim 7 \, \mu m$ height and 45° side wall angles, with a sharpened apex (Fig. 2.3a and b). The tip apex radius was measured by high-magnification scanning electron microscopy of used and unused cantilevers. To measure the tip radius, a circle was fitted manually to the very apex of a tip in SEM images, and the best fitting circle's radius was determined to be the tip apex radius. For OBL, the nominal radius is given as $\sim 30 \, nm$ by the manufacturer. SEM measurements confirmed

the tip radius to be in the range of $25 - 40\,\text{nm}$, with some tips having radii as low as $10\,\text{nm}$. Based on the SEM images of used cantilevers taken after the AFM measurements, a slight blunting was visible, but inspection of topographical AFM images confirms that the bulk of the measurements was performed with tip radii $\leq 40\,\text{nm}$. The spring constant was on average $k = 8.1\,\text{pN/nm} \pm 1.5\,\text{pN/nm}$.

HYDRA2R-100NGG cantilevers (Applied Nanostructures, USA) were used in chapter 4 to compare the measurements to OBL. The HYDRA is as well a Si_3N_4 cantilever, coated with Au on all sides (length, width, and thickness of $\sim 100\,\mu\text{m}$, $\sim 35\,\mu\text{m}$ and $\sim 0.2\,\mu\text{m}$, tip height $\sim 5\,\mu\text{m}$; Fig. 2.3c). Tip radii determined from SEM images were $15 - 20\,\text{nm}$, the spring constant was $k = 11.2\,\text{pN/nm} \pm 0.8\,\text{pN/nm}$. RTESP cantilevers (Bruker) were used to obtain topographic images of nanostructures in tapping mode in air.
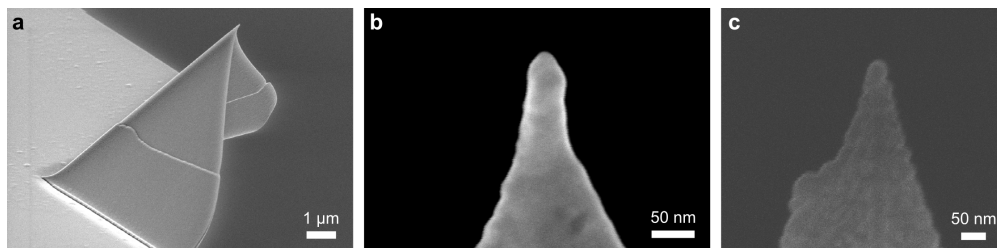
FIGURE 2.3: Scanning electron micrographs of AFM tips. **(a)** OBL tip. **(b)** OBL tip apex. **(c)** HYDRA tip apex.

Force volume measurements

AFM force curves were recorded in force volume (FV) mode. FV maps with 32×32 force curves per map were recorded over randomly selected individual nanorings and nanoholes. FV maps were obtained over an area of $300\,\text{nm} \times 300\,\text{nm}$ for nanoholes, and $500\,\text{nm} \times 500\,\text{nm}$ for nanorings. To avoid tip contamination or damage, great care was taken to minimize unnecessary scanning of the AFM tip on the surface before or between FV acquisitions. Unless otherwise noted, force curves were taken with tip approach velocities of $\sim 2 - 5\,\mu\text{m/s}$. Force triggering was used to limit the maximal applied force during ramping to $500 - 700\,\text{pN}$.

To improve statistics for the loading rate experiments in chapter 4, the point-and-shoot feature of the AFM software was used to take large amount of force curves at specific locations over a nanoring (i.e., over the central hole, over the ring Au surface). Before applying point-and-shoot, an image of the nanoring was taken in contact mode at minimal force ($<50\,$pN) in XY closed loop mode, to determine the exact position where the following force curves were recorded relative to the nanoring. In order to achieve various tip velocities between $0.4 - 29\,\mu$m/s, the cantilever was ramped at $0.6 - 4.9\,$Hz with ramp sizes between $300\,$nm and $3\,\mu$m. The movement of the Z piezo was measured using the internal "height sensor" provided by the AFM hardware to avoid introducing piezo nonlinearities into the force curve data.

2.2.6   AFM data analysis

Cross-sectional height profiles were extracted from AFM topographic images with Gwyddion[2] [90] and averaged to obtain the height of the non-PEGylated nanorings. FV topography maps were corrected after measurement by linearly fitting the glass part (i.e. excluding the nanostructures) of each pixel row and subtracting the whole row by the fit, thereby levelling the data relative to a known surface (the plain glass). FV maps in Figs. 3.9 and 4.7 were 3×3 median filtered to reduce visual pixel noise. Other FV maps were kept unfiltered because the exact pixel values were deemed useful for visual analysis of the maps. Force volume maps and point-and-shoot force curve datasets were analysed by custom-written software using IGOR Pro (WaveMetrics, USA). Appendix B provides a manual for the operation of the custom software. The algorithms used to analyse each recorded force curve are described in the next sections.

---

[2]http://gwyddion.net

Raw force curve transformation

Raw curves with deflection voltages vs Z piezo position were read from binary Nanoscope files. The non-contact part of the force curves was fitted with a linear equation and the fit subtracted from the curve. The raw recorded voltages were converted into forces by multiplying them with the calibrated deflection sensitivity χ and the spring constant k. The force vs Z piezo position curves ($F(Z)$) were transformed into force vs tip-sample distance curves ($F(d')$) by adding the cantilever deflection at each point to the piezo height:

$$d' = Z + \delta \; . \tag{2.9}$$

This way the force acting on the cantilever is plotted against the real distance of the tip from the sample surface (the Z position decreases as the tip moves closer to the surface, while the deflection increases as the cantilever is bent upwards by the acting force). A hard surface is represented by a vertical force curve (i.e. infinite slope, termed "hard-wall") and softer surfaces have smaller slopes. Finally the force curve is shifted horizontally by the position of the hard-wall contact, d'_0, so that the final transformed curve is $F(d) = 0$ at the hard-wall.

$$\begin{aligned} d &= d' - d'_0 \\ &= Z + \delta - d'_0 \; . \end{aligned} \tag{2.10}$$

d'_0 was determined by averaging the tip-sample distances of the hard-wall part of the curve. Fig. 2.4 shows the transformation of two schematic force curves above surfaces of different stiffnesses.

Brush height calculation

Unless noted otherwise, we use a *noise-based method* for measuring the brush height by AFM. The brush height (i.e., initial contact point of the tip with the brush, relative to the hard surface beneath) was calculated from approach force curves by first binomially smoothing the curve, and taking the distance at which
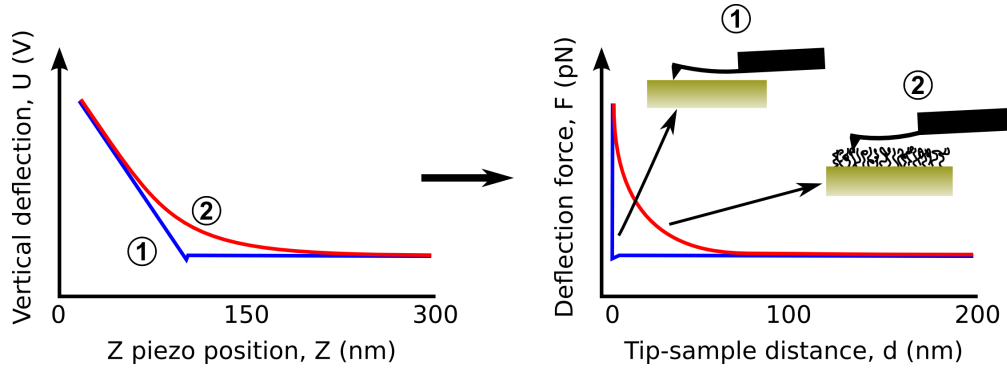
FIGURE 2.4: Transformation of the raw sensor voltage vs Z piezo movement curve (left) to a force vs tip-sample distance curve (right). Curves (1) and (2) correspond schematically to ramping over a bare hard surface (e.g. glass) and over a softer layer, respectively.

the force crosses twice the magnitude of the smoothed baseline (non-contact) force noise. Smoothing was carried out to prevent individual outliers or noise spikes from influencing the brush height calculation. This brush height calculation algorithm robustly assigns a brush height for each analysed force curve, regardless of the exact shape of the curve, but underestimates the real brush height somewhat, since a finite force (estimated $\sim$20 pN) has to be already applied to the brush before detection of the height (see results in chapter 3 for details).

In chapter 5, the brush height was determined by a different algorithm using an exponentially decaying curve,

$$F_{\mathrm{fit}}(d) = Ae^{-\tau d} \ . \tag{2.11}$$

Eq. 2.11 was fitted to the steric repulsive region of the approach force curve with A and τ as free parameters, and the brush contact distance was defined at the point $F_{\mathrm{fit}} = 1$ pN. Not all force curves could be fitted well by an exponential equation. Only curves with a good fit were considered in the analysis. This fit algorithm results in slightly larger (i.e. possibly more realistic) brush height values than the noise-based method used otherwise in this thesis, but is less robust in regard to different force curve shapes.

Brush stiffness calculation

To calculate the stiffness of the brush, two different methods were used. The *linear stiffness*, s [N/m], was defined as:

$$s = \frac{\Delta F}{\Delta Z} = \frac{150\,\text{pN} - 50\,\text{pN}}{Z(150\,\text{pN}) - Z(50\,\text{pN})} \tag{2.12}$$

where $Z(F)$ is the Z piezo position at force F of the approach curve. $50\,\text{pN}$ and $150\,\text{pN}$ were chosen as the limits because these forces are in the sterically repulsive interaction regime between tip and brush and so the calculated stiffness represents the brush properties (Fig. 2.5a). A curve recorded on a hard substrate has a stiffness equal to the cantilever spring constant, $s_{\text{hard}} = k$. Values above s_{hard} are not possible physically, values below signify softer material.

A second measure of stiffness, the *Young's modulus*, was obtained by applying the Hertzian contact model of a sphere indenting an elastic half-space [91] to the approach force curves. The general Hertz force equation is of the form

$$F(d) = A(d_0 - d)^{3/2} \tag{2.13}$$

where $F(d)$ is the force at separation distance d, A is a proportionality constant, and d_0 is the contact point (i.e. zero indentation, in our case the brush height). The Hertz model for a sphere indenting an elastic half-space yields the following form for A:

$$A = \frac{4}{3}\frac{1}{(1 - \nu^2)}\sqrt{R}\,E \tag{2.14}$$

where ν is the sample Poisson number (fixed to 0.3), R the indenting tip radius (fixed to $40\,\text{nm}$), and E the Young's modulus. It was not possible to fit the full repulsive part of the force curves with a single fit. Instead, when splitting the curves in two regions and fitting each region with its Young's modulus, reasonable fits were achieved, with two separate Young's moduli, E_1 and E_2, for each force curve (Fig. 2.5b). Both parts of the force curve were fit simultaneously. Formally,

the fitting equation is expressed as

$$F(d) = \frac{4}{3} \frac{1}{(1-\nu^2)} \sqrt{R} \cdot \begin{cases} E_1 (d_{0_1} - d)^{3/2}, & \text{for } d > d_{\text{split}} \\ E_2 (d_{0_2} - d)^{3/2}, & \text{for } d \leq d_{\text{split}}. \end{cases} \tag{2.15}$$

The subscripts 1 and 2 denote fit parameters valid in region 1 and 2, respectively. The splitting distance d_{split} was regarded as a free parameter as well. Fig. 2.5 shows an example force curve analysed with the two described stiffness extraction methods.
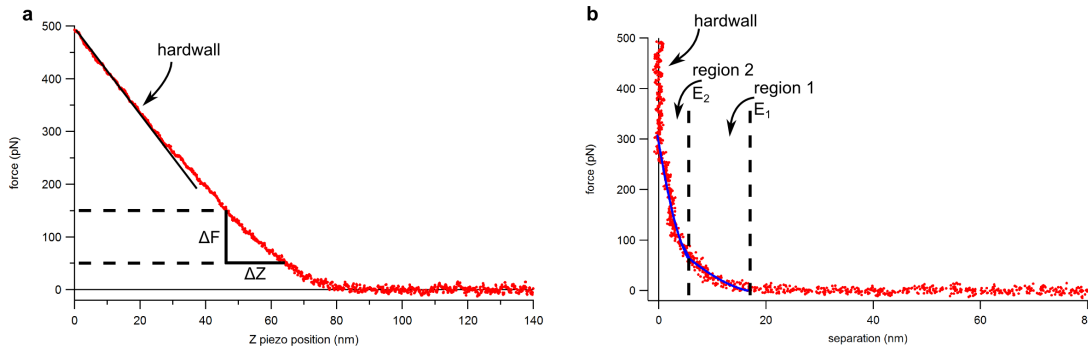
FIGURE 2.5: Two different stiffness measurements performed on a force curve (red dots = data). **(a)** Extracting the linear stiffness from the Z piezo movement between 50 and 150 pN. **(b)** Young's moduli E_1 and E_2 extracted from fits (blue line) of the Hertz contact model to the force curve split in two separate regions.

Escape transition determination

For the determination of escape transition-like effects (chapter 4), each approach force curve over a nanoring was manually classified as either containing a sudden jump in force or not. Curves where this could not be determined unambiguously were excluded from classification ($\sim$15 % of curves over a ring, especially at the very edge of the rings due to spurious interactions of the tip with the ring walls). The classified curves were binned according to the lateral distance of their acquisition position from the ring centre and the number of curves containing a jump was normalized to the total number of classified curves for each bin. Typically, of the 1024 curves in each map around 500 were recorded over the ring, the rest being over the glass substrate and hence not of interest.

2.2.7 Scanning electron microscopy (SEM)

Lateral sizes of nanostructures (nanorings and nanoholes), as well as AFM tip dimensions, were measured by imaging with the Hitachi S-4800 field emission scanning electron microscope (Hitachi, Japan). Nanostructure samples were cleaned and afterwards directly imaged by SEM without additional pre-treatment. AFM cantilevers were taken directly out of the storage box (for imaging new tips) or soaked in DI H_2O for $\sim18\,h$ and left to dry for several days in an enclosed container before imaging by SEM (for tips used in experiments). The cantilevers were attached to SEM sample holders by adhesive carbon conductive tapes, and conductive silver was applied over the cantilever chip substrate (not touching the cantilever itself) to enhance the conductive connection between cantilever and SEM sample holder.

2.2.8 Anti-PEG characterization

Immunoblots

To check the specificity of anti-PEG antibodies against PEG on a standard assay, immunoblotting was performed. $20\,kDa$ mPEG-SH at different concentrations ($1\,\mu l$ per dot) was applied on dry nitrocellulose membranes ($0.45\,\mu m$ pore size, Whatman, UK). The membranes were blocked with $5\,\%$ skim milk and incubated with $50\,nM$ anti-PEG and unspecific control antibodies in PBS-Tween20 ($0.1\,\%$ wt./vol.) for $2\,h$ at room temperature and washed afterwards with PBS-Tween20. Secondary antibody incubation was performed with alkaline phosphatase-conjugated goat anti-mouse-IgG ($1:5000$ dilution; A3562, Sigma-Aldrich) for $1\,h$. After washing, CDP-Star chemiluminescent substrate (Applied Biosystems, USA) was added onto the membranes for $5\,min$. The membranes were exposed on medical x-ray films (Fujifilm, Japan).

Anti-PEG to PEG binding constants

Custom SPR sensor substrates were prepared for measuring the binding affinity of Anti-PEG towards a surface-attached PEG brush. Glass slides ($10\,mm \times 12\,mm \times 0.17\,mm$, Karl Hecht, Germany) were immersed into freshly prepared Piranha solution[3] ($3:1\ H_2SO_4 : H_2O_2$) and subsequently sonicated in DI water followed by high purity ethanol and dried under a N_2 gas stream. Next, the glass slides were cleaned for $30\,min$ in UV-ozone before thermal evaporation of $2\,nm$ Ti and $50\,nm$ Au layers onto the glass slides in vacuum. The substrates were then stored in an argon atmosphere after removal from the vacuum deposition chamber until usage. SPR measurements were performed using a BIAlite system (GE Healthcare Life Sciences, formerly Biacore) consisting of two flow cells. All reagents used in the measurements were dissolved in PBS that was filtered through $0.2\,\mu m$ membrane pores (Sarstedt). The samples were then spun in a centrifuge for degassing.

The bare gold surfaces were incubated with $0.5\,mM$ $20\,kDa$ mPEG-SH for $25\,min$ in flow cell 2. Flow cell 1 was passivated with $1\,mM$ 6-mercaptohexanol (6-MH) (Fluka) in PBS for $5\,min$ and used as a reference. After mPEG-SH incubation, an additional $1\,mM$ 6-MH was added for $3\,min$ to both flow cells at a flow rate of $2\,\mu l/min$ to block any remaining Au surfaces left exposed. Fluorescently-labelled anti-PEG (E11) was then applied at different concentrations ($0.08\,nM$, $0.156\,nM$, $0.3125\,nM$, $0.625\,nM$, $1.25\,nM$ and $2.5\,nM$) for $33\,min$ at $3\,\mu l/min$ flow rate each. The PBS running buffer was filtered and degassed with $0.2\,\mu m$ pore size filterware (Nalgene) before connecting to the SPR instrument. The SPR measurements were performed at $25\,°C$.

---

[3]Piranha solution is very dangerous. Adhere to the appropriate safety measures when preparing and handling it.

2.2.9 Antibody incubation on nanorings

For the antibody experiments in chapter 5, anti-PEG, specific IgG, and/or un-specific IgG antibodies (for an explanation of the terms, see chapter 5) were pre-incubated together with either 1 % BSA or rabbit serum at their final concentrations for at least 1 h prior to use. BSA was used in all PBS-based experiments to reduce the unspecific adsorption of antibodies (so as to reduce background fluorescence) on the glass substrate with the following exceptions: (i) AFM force measurements in the absence of antibodies (i.e., PBS; Fig. 5.4), (ii) after NaOH washing (Fig. 5.4), and (iii) the fouling control (Fig. 5.8a). BSA was not used in the blood serum experiments given that rabbit serum albumin was already present. Solutions were pipetted on individual samples (pre-incubated for 15 min in 1 % BSA or serum) and incubated for 30 min in darkness. Fluorescence and AFM measurements were performed without washing the sample or replacing/diluting the solution.

After the first incubation was performed as above, the reversibility data in PBS (Fig. 5.3f) were obtained by applying 500 mM NaOH (pH 13.7) in deionized water to the sample surface for 30 min in darkness, after which the sample was rinsed with deionized water. This rather harsh condition affected the quantitative reversibility of anti-PEG binding over subsequent targeting–wash cycles (Fig. 5.3f), but was important at the time to ensure the complete removal of prebound antibodies. Over the course of our later experiments in blood serum (Fig. 5.7), we subsequently found that 10 mM NaOH (pH 12) was the optimal condition to clean and regenerate the PEG, all other aspects of the cleaning protocol remaining the same. Therefore, the extent of PEG regeneration can vary with NaOH conditions.

For time-lapse measurements, the sample surface was pre-incubated as above. Fluorescence images were taken before adding antibodies and directly after addition.

2.2.10   Fluorescence measurements

Total internal reflection fluorescence (TIRF) setup

Fluorescence images were obtained with a 1.46 NA TIRF 100× oil immersion objective (Leica Microsystems, Germany) with an additional tube magnification of 1.6× in a Leica DMI6000 B inverted microscope integrated together with the AFM system. The fluorescence microscope was fitted with a TIRF module (Leica AM TIRF MC) using three solid-state lasers with wavelengths of 488 nm, 561 nm and 635 nm. Table 2.1 lists the band pass filter cubes used by the different laser lines. The sample was automatically illuminated at the correct angle to achieve an evanescent wave decay length of 90 nm in TIRF mode, and wide-field laser illumination of the sample in epifluorescence mode. Images were taken with an EMCCD camera (C9100-02, Hamamatsu, Japan) in 14-bit mode with a resulting pixel size of 50 nm/pixel. Data sets used for the analysis of fluorescence intensity were collected under the same parameters and constant EM gain. In Figs. 5.3a–d, 5.7a, and 5.8, the exposure times for Alexa488, Cy3, and Cy5 were set at 2 s, 600 ms, and 3 s with constant EM gain, respectively. In Fig. 5.8c, the Cy3 channel was exposed for 300 ms. During time-lapse imaging, for each time point, the sample surface was manually focused before taking an image.

TABLE 2.1: Excitation and emission bandpass filter cubes
used for TIRF imaging

	Filter pass bands	
Laser line (fluorophore)	excitation (nm)	emission (nm)
488 nm (Alexa Fluor 488)	490 ± 10	525 ± 25
561 nm (Cy3)	560 ± 5	610 ± 33
635 nm (Cy5)	635 ± 5	720 ± 30

Fluorescence Data Analysis

Fluorescence images were rotated, cropped, and pseudocolored using ImageJ [92]. Brightness and contrast values were adjusted for best visual clarity. For Figs. 5.3a–d, 5.7a, and 5.8, automatic background subtraction was performed as provided by ImageJ (sliding paraboloid method, radius 100 pixels).

Quantitative fluorescence intensity analysis in Figs. 5.3 and 5.7 was performed identically for each condition with custom macros in ImageJ (see appendix B for a description of the macros). 10×10 nanorings within the array were selected for intensity analysis. First, individual nanoring intensities were obtained by averaging over all pixels enclosed within a diameter of 16 pixels. Next, the background intensity was averaged over an area of 100 pixels $\times$ 500 pixels outside the ring array. The mean fluorescence intensity was calculated by averaging over the 100 individual nanoring intensities and dividing by the background intensity. We found that the mean fluorescence intensities obtained in the absence of antibodies gave values above background. This was caused by small autofluorescence effects at the nanorings, which we measured to be 2 % above the background for Alexa488 and Cy3 and 6 % above the background for Cy5. Nevertheless, we accounted for these effects by subtracting the non-zero values from all mean fluorescence intensities on a per channel basis.

Subsequently, the mean intensities from Alexa488 and Cy3 were scaled to have the same value at the first targeting measurement with the same scaling factor being applied to each respective fluorescence channel throughout all the targeting and washing steps. The calculated fluorescence intensities were additionally offset so that background (autofluorescence subtracted) equals unity. In this way, the relative intensities remained self-consistent and allowed comparisons to be made within individual experimental sets. Histograms were calculated from these relative intensities with a bin width of 0.1 fluorescence units.

For time-lapse fluorescence analysis, a single average fluorescence intensity value was extracted for each time point and plotted against time after the start of

the incubation. The intensity was obtained by averaging fluorescence intensities within a diameter of 16 pixels over 100 rings. Each kinetic trace was fitted with the equation

$$I(t) = A \left(1 - e^{-k_{\mathrm{obs}}t}\right) \tag{2.16}$$

with $I(t)$ being the fluorescence intensity at time t, A being the equilibrium intensity at infinite time, and k_{obs} being the observed kinetic rate constant. Each trace was normalized by A.

Chapter 3

Characterization of Poly(ethylene glycol) Grafted to Au Surfaces and Nanostructures

Poly(ethylene glycol) (PEG) grafted to Au surfaces forms the bulk of the samples in this thesis. It is thus important to accurately characterize the grafting conditions and the resulting polymer morphology on the surfaces. In this chapter we first characterize the PEG coil size in solution. Afterwards, systematic studies of PEG layer formation on Au surfaces are performed. By using surface plasmon resonance (SPR) we can measure the density of PEG chains covalently grafted to the Au surface from solution under various grafting conditions and for different PEG chain lengths (i.e. chain molecular weights). We apply a recently developed SPR technique for measuring molecular layer heights and show that PEG is forming a polymer brush on the surface under our chosen grafting conditions. Additionally we show how different grafting conditions lead to different final brush heights.

In this chapter we introduce our main experimental system of Au nanorings fabricated on microscopy glass slides. The functionalization of the nanorings with PEG (*PEGylation*) creates unique, "real" 3D nanopatterned polymer brush systems (as opposed to nanopatterning on flat surfaces) with different local geometries.

Atomic force microscopy (AFM) with its nanometre-sharp probe is well suited to measured the PEG brush morphology and other nanomechanical and dynamical properties on the nanorings. We compare AFM measurements on the nanorings to our SPR data for flat surfaces, and to different theoretical models of brush compression by an obstacle.

Finally, to show that our AFM-based approach is valid and useful for different kind of polymer-brush functionalized nanoscale structures we perform AFM measurements on Au nanoholes with a slightly differing geometry. Here we demonstrate how differently sized PEG chains grafted to the nanostructures can have a profound effect on the access of nanoscale particles to the inner volume of the nanoholes.

3.1   PEG chain size in solution

The size of polymer coils in solution influences the grafting density on the surface in a "grafting-to" approach [93]. The polymer coil size in a solvent decreases as the conditions change from good solubility to marginal solvation at the "cloud point" (at which precipitates start to form, thus clouding the solution). In our experiments, we use H_2O and phosphate-buffered saline (PBS) as examples of good solvents for PEG. Adding Na_2SO_4 to the solvent drives the solution towards the cloud point. In the experiments described in this thesis we take advantage of the different resulting grafting densities when incubating our samples at different salt (Na_2SO_4) and PEG concentrations.

First, to establish the PEG coil size in good solvent and at cloud point, we performed dynamic light scattering measurements (DLS; Methods section 2.2.3) of 20 kDa PEG chains at good solvent conditions (PBS, 5 mg/ml PEG concentration) and just below cloud point (0.9 M Na_2SO_4 in PBS, 0.13 mg/ml PEG concentration). Figure 3.1 shows the correlation function and number fraction distribution of 20 kDa PEG in good solvent, and Figure 3.2 shows the data for the cloud point conditions. In both cases we have a good fit to the correlation curves from which

the coil sizes can be extracted. The number fraction distribution shows a single peak in each case, indicating that $>99\%$ of coils by number have sizes within this peak. The deviation of the correlation curve fit at large time scales indicates some possible formation of aggregates or precipitates, which however do not interfere with the measurements. The actual size of the PEG coils was extracted from the intensity fraction distribution, as this is more accurate. The measured hydrodynamic sizes were $R_{\mathrm{H,PBS}} = 9.3\,\mathrm{nm} \pm 2.4\,\mathrm{nm}$ for the good solvent case, and $R_{\mathrm{H,CP}} = 0.69\,\mathrm{nm} \pm 0.07\,\mathrm{nm}$ at cloud point. The hydrodynamic size is the diameter of a solid sphere with same diffusion times as the measured particles. For the linear polymer PEG it corresponds to the characteristic polymer coil size (i.e. Flory length R_F). The data indicate a complete collapse of the coils at cloud point to a fraction of their well-solvated size. It is thus reasonable to assume that grafting to a surface at cloud point leads to a much denser polymer layer at the surface because the already adsorbed polymer chains exert a much smaller steric hindrance effect to new chains adsorbing from the solution.
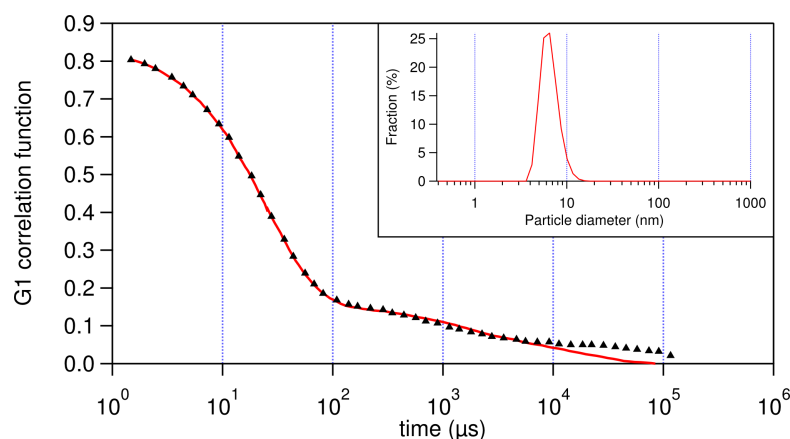
FIGURE 3.1: DLS measurement of $20\,\mathrm{kDa}$ PEG, $5\,\mathrm{mg/ml}$ in PBS (good solvent conditions). Correlation function data (triangles) and fit (solid line). Inset: Particle diameter distribution (number fraction).

3.2   PEG grafting density

To have an accurate understanding of the grafting of methoxy-PEG-thiol (mPEG-SH) to gold surfaces, we used surface plasmon resonance (SPR) to assess the final
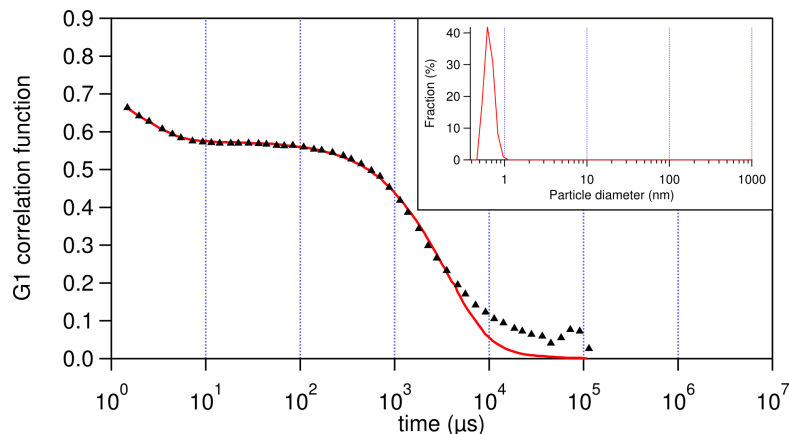
FIGURE 3.2: DLS measurement of 20 kDa PEG, 0.13 mg/ml with 0.9 M Na_2SO_4 in PBS (cloud point conditions). Correlation function data (triangles) and fit (solid line). Inset: Particle diameter distribution (number fraction).

grafting density for different PEG chain sizes and grafting solutions. We performed SPR measurements with 5 kDa, 10 kDa and 20 kDa mPEG-SH on bare Au sensor chips, both at good solvent conditions and at cloud point, as well as at various conditions in between. The thiol end group forms a stable covalent bond with the Au surface of the sensor chip. The grafting densities calculated from the adsorbed mass signal (Methods section 2.2.4) proved to be very reproducible, varying less than 3 % between independently prepared samples. Figure 3.3 shows an example sensogram with 20 kDa PEG grafted under three different conditions. Grafting in good solvent (PBS; 40 mg/ml PEG) results in much less adsorbed mass on the surface than near the cloud point in 0.9 M Na_2SO_4 (0.1 mg/ml PEG), even though the PEG concentration in solution is much lower in the latter case. The use of very low PEG concentration (2.5 µg/ml) in 0.6 M Na_2SO_4 results in an intermediate amount of PEG at the surface.

Table 3.1 summarizes the grafting densities, σ (in number of chains per unit area), and average grafting distances, $g = \sigma^{-1/2}$, for PEG at various incubation conditions. Figure 3.4 shows an overview of grafting distances plotted against the PEG concentration in Na_2SO_4-containing solvent. For each PEG molecular weight there is a maximum achievable grafting density, above which higher PEG concentrations in solution do not yield an increased adsorption to the surface. This "plateau" is reached already far below the cloud point PEG concentration (right-most point
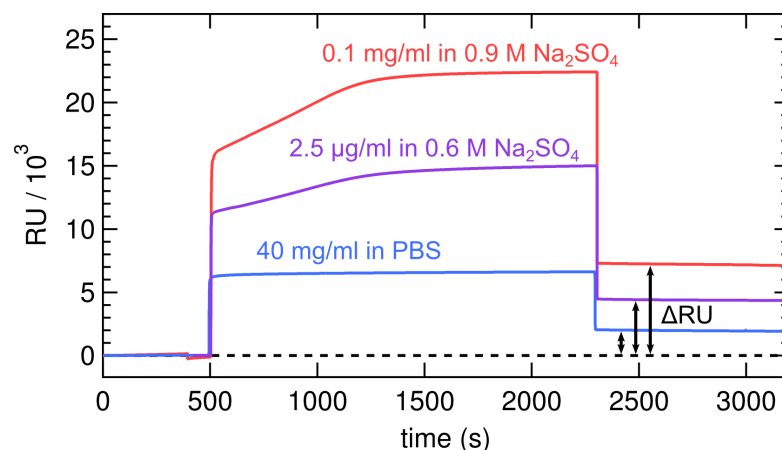
FIGURE 3.3: Examples of 20 kDa mPEG-SH surface immobilization SPR senso-grams (RU = SPR response units). From 500 – 2300 s (i.e. for 30 min), PEG was injected at the concentrations and in the solvents indicated. Before and after, PBS was flowed over the sensor surface. The surface density of attached PEG was read out from the response unit difference (ΔRU, which is proportional to the adsorbed mass) to the baseline. The resulting average grafting distances between adjacent polymer chains were $g_{0.9\text{M}} = 2.1$ nm, $g_{0.6\text{M}} = 2.8$ nm, and $g_{\text{PBS}} = 3.9$ nm.

for each condition in Figure 3.4). Larger grafting distances can be achieved by using appropriately low PEG incubation concentrations. As expected, shorter PEG chains allow for higher grafting densities under otherwise identical grafting conditions. For 20 kDa PEG we show that using 0.9 M instead of 0.6 M Na_2SO_4 yields a slightly higher grafting density (i.e. lower grafting distance).
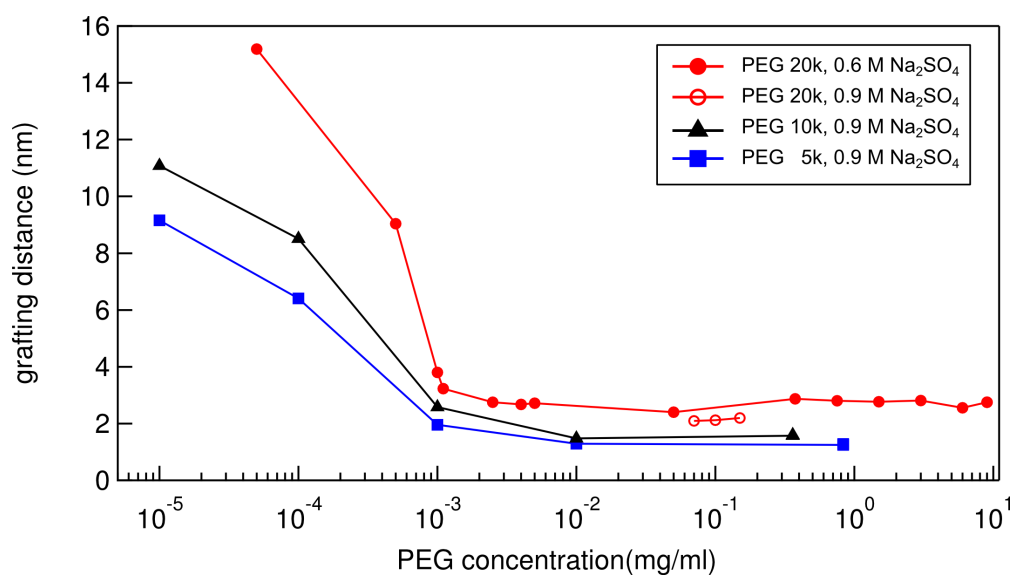
FIGURE 3.4: Average PEG surface grafting distances from SPR measurements.

TABLE 3.1: Grafting densities (σ) and corresponding average grafting distances ($g = \sigma^{-1/2}$) of mPEG-SH (molecular weight M_W) grafted at concentration c in the given solvent to Au SPR chip surfaces.

M_W (kDa)	c (mg/ml)	solvent	σ (chains/nm^2)	g (nm)
20	40	H$_2$O	0.066	3.9
	40	PBS	0.059	4.1
	0.15[a]	0.9 M Na$_2$SO$_4$	0.21	2.2
	0.3[a]	0.7 M Na$_2$SO$_4$	0.17	2.4
	9.0[a]	0.6 M Na$_2$SO$_4$	0.13	2.8
	0.001	0.6 M Na$_2$SO$_4$	0.069	3.8
10	20	PBS	0.21	2.2
	0.36[a]	0.9 M Na$_2$SO$_4$	0.39	1.6
	0.001	0.9 M Na$_2$SO$_4$	0.15	2.6
5	10	PBS	0.31	1.8
	0.83[a]	0.9 M Na$_2$SO$_4$	0.59	1.3
	0.001	0.9 M Na$_2$SO$_4$	0.25	2.0

[a] cloud point conditions.

3.3 PEG polymer brush formation

As can be seen from Table 3.1 and Figure 3.4, most grafting conditions investigated here lead to an average grafting distance between chains that is smaller than the hydrodynamic size in good solvent (for 20 kDa PEG, $R_{\mathrm{H,PBS}} = 9.3$ nm). This means that the chains cannot remain in a random-coiled mushroom state and must assume a brush morphology on the surface. We investigated this using a recently developed SPR-based method [86, 94] employing non-interacting particles to directly probe the height of a molecular layer on the surface. This method bypasses refractive index uncertainties which usually compromise the reliability of height measurements in SPR (Methods section 2.2.4).

After grafting 20 kDa PEG to the sensor chip Au surface at different conditions, the resulting layer height in PBS solvent was measured. For this, non-interacting

TABLE 3.2: Grafting distances (g) and resulting polymer brush heights (h) for 20 kDa PEG grafted to the Au SPR sensor surface at concentration c, in the indicated solvent. The brush height was measured in PBS. After a wash with NaOH to remove weakly bound polymer chains, the brush height was measured again (h_{wash}).

c (mg/ml)	solvent	g (nm)	h (nm)	h_{wash} (nm)
40	PBS	4.1	19	17
0.001	0.6 M Na_2SO_4	3.2	27	26
0.1[a]	0.9 M Na_2SO_4	2.1	39	33

[a] cloud point conditions.

molecules were flowed over the grafted PEG layer, in our case the protein bovine serum albumin (BSA), which has been shown not to bind to PEG brushes [95]. Comparing the SPR signal of the BSA probe molecules over the PEG layer to the signal over a passivated reference surface on the same chip allows the calculation of the PEG layer height. Figure 3.5 shows an example sensogram with a standard PEG immobilization signal, followed by three short BSA injections to probe the layer height. Table 3.2 lists the measured heights in PBS solvent for three chosen grafting conditions. For all conditions, the measured heights are larger than the hydrodynamic coil size in solution, which means that the PEG indeed forms a brush on the surface.
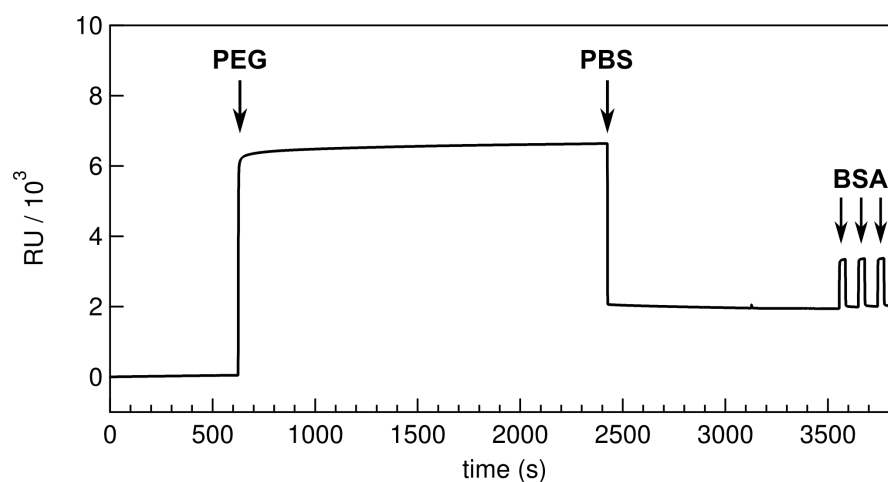
FIGURE 3.5: SPR sensogram with the PEG immobilization signal (40 mg/ml of 20 kDa PEG in PBS), and afterwards three BSA injections to probe the immobilized layer height.

As expected from polymer brush theory [6], a smaller grafting density yields a shorter brush height. The scaling of polymer brush height h as a function of its surface density σ follows the power law

$$h \sim \sigma^n \qquad (3.1)$$

with n being between 0.33 and 0.6 for moderate to high brush densities in a good solvent [47]. For our measurements the best fit is $n \approx 0.5$, which is in good agreement with published results [47]. The measurements also show that although the grafting at cloud point conditions happens with collapsed PEG coils, the chains re-extend to form a brush after switching to good solvent conditions.

To check the stability and covalent bonding of the PEG-thiols to the Au surface, after measuring the initial brush height with the BSA method we flowed 0.2 M NaOH over the PEG brushes for 300 s. This treatment removes any weakly non-covalently bound species from the surface. Immediately afterwards we re-measured the height in PBS. The NaOH wash lead to a reduction in brush height of $5 - 15\%$ (Table 3.2). Due to signal drift in the system we could not accurately measure the grafting distance after NaOH wash, but from our fitted power-law exponent (Eq. 3.1) we see that the calculated grafting distance increases by $5 - 15\%$ as well. This means that the predominant amount of PEG chains was covalently bound to the surface, forming a stable polymer brush.

3.4   PEG-functionalized Au nanorings

To investigate the behaviour of PEG brushes confined to 3D nanoscale objects, we use Au nanorings as our main experimental system in this thesis. Arrays of 20×20 Au nanorings were fabricated on microscopy glass slides (Methods section 2.1.1), with each nanoring having the following dimensions: inner diameter ~ 100 nm, outer diameter ~ 400 nm (measured by SEM), height ~ 30 nm (measured by AFM). Figure 3.6 shows optical and SEM images of a nanoring array. The

nanorings were functionalized with 20 kDa PEG at the different conditions invest-
igated by SPR (Methods section 2.2.2), and measured by AFM in PBS solvent.
Figure 3.7 shows AFM contact mode scanning images of bare unfunctionalized and
PEGylated nanorings (incubated with 40 mg/ml PEG in PBS). The topography
of the bare rings can easily be resolved by the AFM tip, whereas when scanning
at a low force over PEGylated rings (<50 pN; ca. 20 pN is the lowest achievable
setpoint above the noise threshold), the PEG forms a repulsive barrier against the
pushing tip and the rings appear occluded. It is noteworthy that at the centre of
the nanorings there are no PEG chains attached to the glass base. Nevertheless
the PEG chains at and near the inner walls stretch out towards the centre and
cover the central hole.
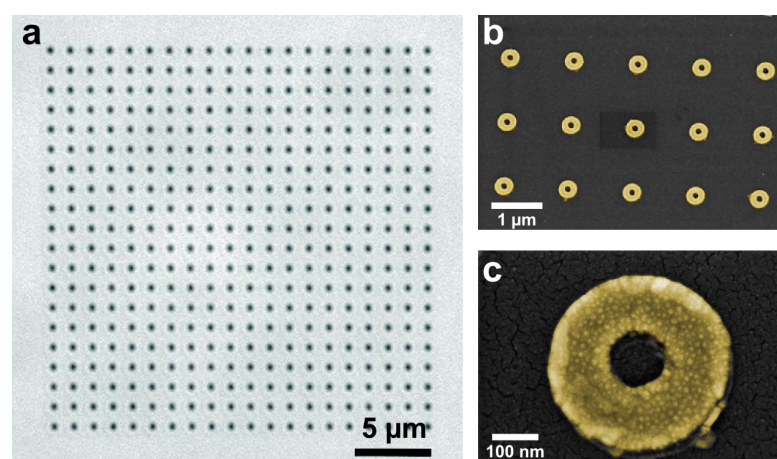
FIGURE 3.6: **(a)** Optical image of a 20×20 Au nanoring array fabricated on
a glass slide. **(b, c)** False-color SEM images of Au nanorings at two different
magnifications (yellow: Au; gray: glass).
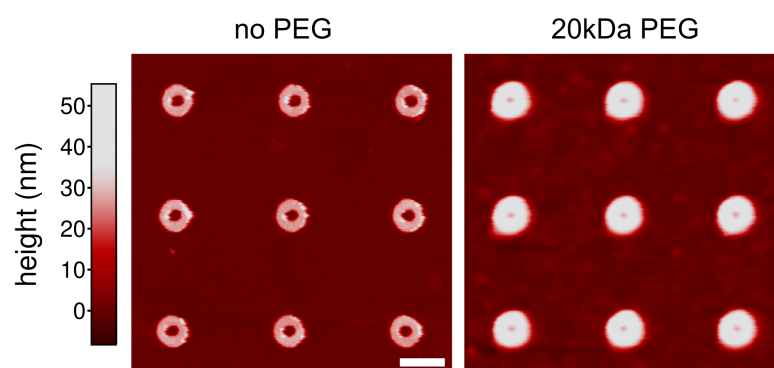
FIGURE 3.7: AFM height images (contact mode imaging) of bare Au (left) and
PEGylated nanorings (right), scanned at low force (<50 pN). Scale bar, 500 nm.

Figure 3.8 shows the dynamic and flexible nature of the PEG chains on the rings. As previously we see the barrier effect of PEG at low force ($<50\,\mathrm{pN}$). At higher force ($1.4\,\mathrm{nN}$) the AFM tip pushes through the PEG chains, revealing the underlying ring topology. Upon returning to a low force setpoint, the barrier against the scanning tip is re-established again. This also shows that the PEG brush remains undamaged when imaged at a high force.
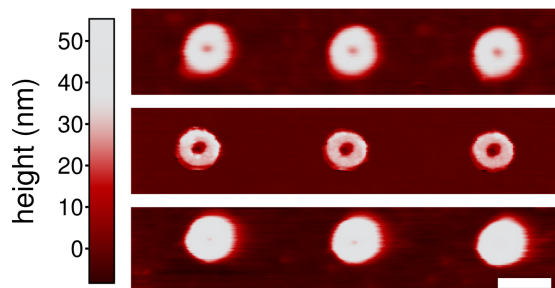
FIGURE 3.8: AFM height images (contact mode scanning) of PEGylated Au nanorings. Top row: Image taken at a low scanning force ($<50\,\mathrm{pN}$), visualizing the PEG brush above the nanorings. Middle row: When the same sample is scanned at high force ($1.4\,\mathrm{nN}$) the AFM tip pushes through the brush, revealing the nanoring structure. Bottom row: Upon returning to a low scanning force, the brush barrier is re-established again. Scale bar, $500\,\mathrm{nm}$.

By using force spectroscopy, we obtain additional quantitative information about the PEG brush on the nanorings. Fig. 3.9 shows force volume (FV) maps with 32×32 force curves (one curve per pixel, over an area of $500\,\mathrm{nm} \times 500\,\mathrm{nm}$; see Methods section 2.2.5) taken above individual nanorings. FV maps were recorded in PBS for rings PEGylated at low density (as measured by SPR; incubation in $40\,\mathrm{mg/ml}$ PEG in PBS, $g_{\mathrm{SPR}} = 4.1\,\mathrm{nm}$) and at high density ($0.13\,\mathrm{mg/ml}$ PEG in $0.9\,\mathrm{M}\,\mathrm{Na_2SO_4}$ in PBS, $g_{\mathrm{SPR}} = 2.2\,\mathrm{nm}$). The solvent of the high-density sample was then exchanged in-situ from PBS to $0.9\,\mathrm{M}\,\mathrm{Na_2SO_4}$ in PBS, followed by another FV measurement.

Fig. 3.10a shows typical approach force curves for the low- and high-density brush on a nanoring, compared to a curve taken over the unfunctionalized glass part of the sample. When compressing the brush, we measure an exponentially increasing steric repulsive force up to the hard-wall contact point, at which the tip cannot penetrate further into the sample and an "infinitely stiff" barrier is measured. At low density, the repulsive interaction starts closer to the hard-wall compared to the

grafting density (g$_{SPR}$): low (4.1 nm)   high (2.2 nm)   high (2.2 nm)

measurement conditions: PBS   PBS   0.9 M Na$_2$SO$_4$

topography (nm)
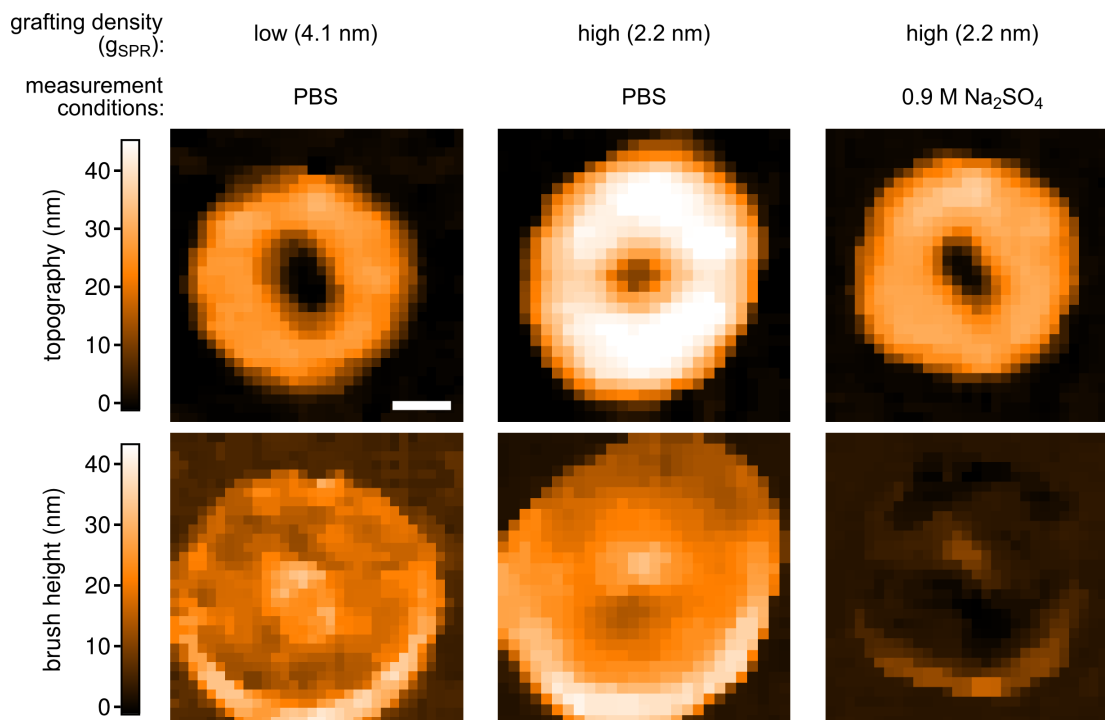
brush height (nm)

FIGURE 3.9: Force volume maps over individual nanorings functionalized with 20 kDa PEG, taken under different conditions. The top row shows the topography of each ring (extracted from the hard-wall position), the bottom row shows the brush heights relative to the hard-wall position. The column labels indicate the grafting density of PEG, as measured by SPR (g_{SPR}), and the solvent at time of measurement. Scale bar, 100 nm.

high density case. This is what we expect for a lower vs higher brush. Appendix A contains additional example force curves taken over low and high density brushes. Over glass, no long-range interaction between tip and sample is measurable before the contact to hard-wall. Fig. 3.10b shows a comparison between a force curve on glass in PBS, and on the PEGylated ring in 0.9 M Na$_2$SO$_4$. As expected from the DLS measurements, the PEG chains collapse to tight coils, so that no brush is detected by AFM any more. The PEG remains on the rings though, as can be seen by an occasional pulling and stretching of one or several PEG chains upon tip retraction, which leads to a negative force as the cantilever is bent towards to surface. No such pulling curves are recorded on glass.

The brush height can be extracted from each recorded force curve by measuring the onset of the repulsive force. We define the brush height as the distance from the point where the force exceeds twice the baseline noise level (noise-based method, see section 2.2.6), to the hard-wall part of the force curve (which is set to zero
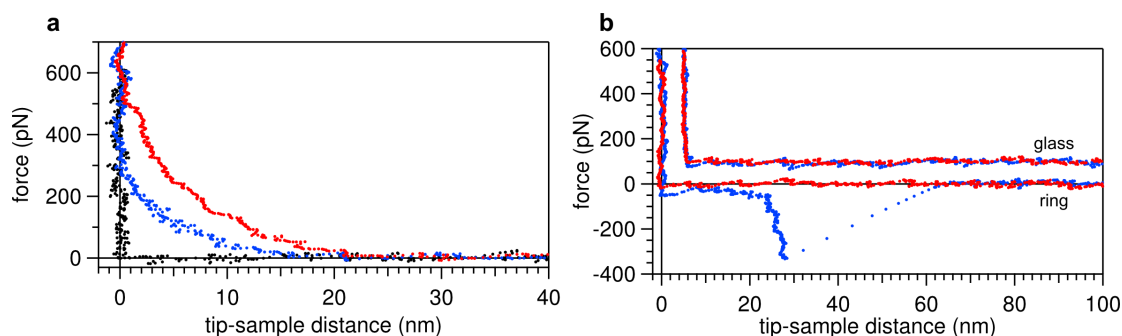
FIGURE 3.10: **(a)** Typical approach force curves taken over the ring for a high-density ($g_{SPR} = 2.2\,nm$, red) and a low-density ($g_{SPR} = 4.1\,nm$, blue) brush in PBS. For comparison, a force curve over the unfunctionalized glass next to a PEGylated nanoring is shown (black). **(b)** Comparison of approach (red) and retract (blue) force curves over unfunctionalized glass in PBS and over a high-density PEGylated nanoring in $0.9\,M\ Na_2SO_4$. The glass force curve is offset by ($5\,nm$, $100\,pN$) for clarity.

height). Fig. 3.11 illustrates the brush height measurement principle where the height is measured relative to the hard-wall surface at the position where the tip is probing.
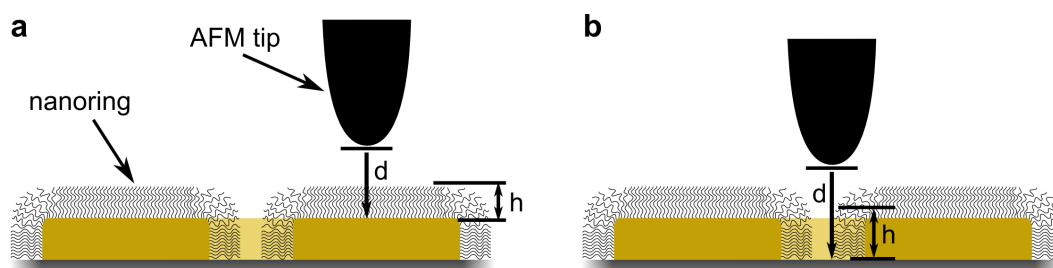
FIGURE 3.11: Cartoon illustrating the brush height measurement on top of a nanoring by an AFM tip. **(a)** Over the ring, the tip-sample distance d and the brush height h are measured relative to the ring surface. **(b)** At the central hole, d and h are measured relative to the pore base.

Fig. 3.12 shows brush height histograms extracted from the FV maps in Fig. 3.9. When the brush is surrounded by good solvent (PBS; Fig. 3.12a and b), we see two distinct peaks in the histograms. The first one, at heights $<5\,nm$, stems from the curves obtained above the glass. Here, no PEG molecules are present, but our algorithm assigns an "apparent" brush height for these regions as well. The brush height measurement and calculation algorithm is robust for heights above $5\,nm$, but becomes inaccurate below that threshold, due to measurement noise and possible spurious short-range interactions between tip and substrate.

Thus even pixels with no brush can get a small brush height value assigned. The glass peak serves as an internal control to assert that both the sample and the AFM tip are clean. The second peak shows the brush height distribution above the PEGylated nanoring. The two peaks are fitted together with a sum of two Gaussian distributions, and the brush height over the rings can be extracted from the mean value of the second fitted Gaussian.
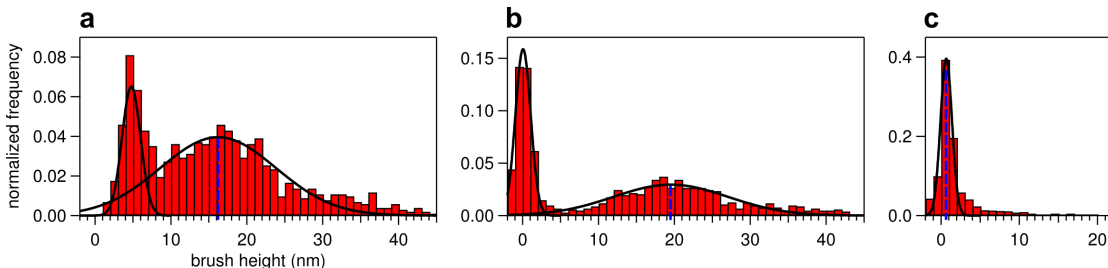
FIGURE 3.12: Brush height histograms for nanorings functionalized with 20 kDa PEG (from data in Fig. 3.9). **(a)** PEG grafted at low density ($g_{SPR} = 4.1$ nm), measured in PBS. **(b)** Grafted at high density ($g_{SPR} = 2.2$ nm), measured in PBS. **(c)** Grafted at high density, measured in 0.9 M Na_2SO_4. Solid lines are Gaussian fits to measured brush heights on glass (no PEG) and on the rings. The dashed line indicates the average brush height over the ring. In c, the brush has collapsed, and only one peak is discernible.

For nanorings incubated at low density conditions (Fig. 3.12a), we obtain a brush height of $h = 16.2$ nm. For high density conditions (Fig. 3.12b), we get $h = 19.5$ nm. These brush heights can be compared to the ones measured by the SPR BSA method at identical grafting conditions: $17 - 19$ nm for low PEG density and $33 - 39$ nm for high density (Table 3.2). In the low density case we measure a slightly lower value by AFM than by SPR, while in the case of high density grafting we get a significantly smaller value. Smaller values from our AFM noise-based brush height measurement method than from the SPR method are expected, since the tip has to exert a force on the brush first before a repulsion can be measured (see Discussion, section 3.7 for further elaboration).

After exchanging the solvent to 0.9 M Na_2SO_4 for the high-density sample, the data collapses into a single histogram peak <5 nm (Fig. 3.12c). At this condition, the unfunctionalized glass and the PEGylated ring cannot be distinguished any more based on the height measurement, as we already saw from the force curves in Fig. 3.10b.

3.5   PEG brush compression force analysis

The theoretical force vs distance equations that were derived for two polymer brush–functionalized plates pushing towards each other, and later adapted for an AFM tip pushing onto a polymer brush grafted on a flat surface, can be compared to our measurement data (see derivations in Introduction, section 1.4.3). Since the brush height and the surface grafting density are variables in the theoretical equations, the parameters extracted from fits of the theoretical equations to the AFM data can be compared to the values from SPR measurements. Fig. 3.13 shows force curves recorded at high and low density brush conditions (as defined previously) and best fits of different applicable models to the data.
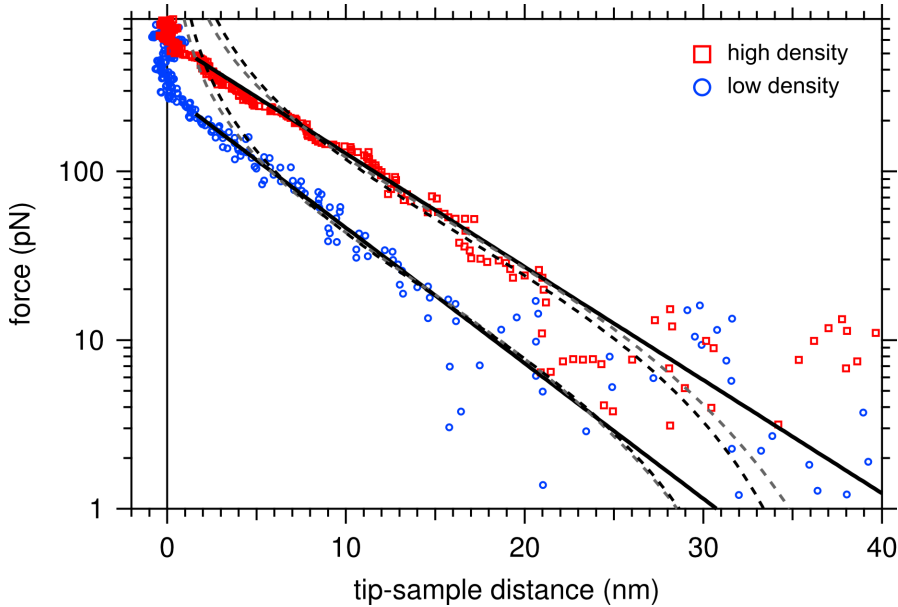
FIGURE 3.13: Logarithmic plots of force curves taken over rings PEGylated at high density ($g_{SPR} = 2.2\,\text{nm}$, red squares) and at low density ($g_{SPR} = 4.1\,\text{nm}$, blue circles). The force curves were fitted with the exponential approximation of the Alexander–de Gennes equation (solid lines), the full Alexander–de Gennes equation using a step brush profile (black dashed lines), and with the Milner–Witten–Cates equation using a parabolic brush profile (grey dashed lines). The noise limit of the measurement system is slightly below 20 pN

We fitted the data to the full Alexander–de Gennes (AdG) equation with Derjaguin approximation, adapted for a brush attached on a single surface,

$$F(d) = \frac{8\pi}{35} R_{\text{tip}} k_B T \frac{h}{g^3} \left[-12 + 7 \left(\frac{h}{d} \right)^{5/4} + 5 \left(\frac{d}{h} \right)^{7/4} \right] \tag{3.2}$$

where $F(d)$ is the repulsive force at distance d from hard-wall contact, the tip radius $R_{\text{tip}} = 30\,\text{nm}$ (based on SEM images of the tip), k_B is the Boltzmann constant, temperature $T = 300\,\text{K}$. The grafting distance g and the brush equilibrium height h were free parameters. The equation fits the data well up to tip-sample distances of $d \approx 5 - 10\,\text{nm}$. At large d the sensitivity of the AFM is not enough to determine the quality of the fit. At short d the theoretical fit deviates substantially from the data.

The AdG equation assumes a step form of the brush profile, i.e. a uniform brush density up to its brush height h, and zero density beyond. For real brushes, the profile has been measured to be parabolic instead. An improved model is thus the Milner-Witten-Cates (MWC) equation which calculates the force for a parabolic brush profile. The MWC force, with Derjaguin approximation and single-surface brush is

$$F(d) = \pi R_{\text{tip}} k_B T N \left(\frac{\pi^2 a^4}{12} \right)^{1/3} g^{-10/3} \left[\frac{h}{d} + \left(\frac{d}{h} \right)^2 - \frac{1}{5} \left(\frac{d}{h} \right)^5 - \frac{9}{5} \right] \tag{3.3}$$

with $N = 455$ being the monomer number for $20\,\text{kDa}$ PEG, and $a = 0.35\,\text{nm}$ the monomer size. Again, h and g were left as free parameters for the fit. The MWC equation yields a very similar fit to the data as the AdG model at forces which are accessible to our setup. The good fit range is slightly enhanced towards short and long distances d, but at small d the fit deviates again substantially from our data.

The most commonly used equation to describe the force needed to compress a brush by an AFM tip is the exponential approximation of the AdG-equation, which is valid at intermediate tip-sample distances, $0.2 < d/h < 0.9$. With Derjaguin approximation and single-surface brush:

$$F(d) = R_{\text{tip}} \frac{50h}{g^3} k_B T \exp\left(-\frac{2\pi d}{h} \right) \tag{3.4}$$

where g and h are free parameters for grafting distance and brush equilibrium height. As can be seen in Fig. 3.13, this equation fits our data well, over the

TABLE 3.3: Grafting distances (g) and brush heights (h) for low and high density 20 kDa PEG grafted to the nanorings, extracted from force curve fits to three different theoretical equations and the noise-based measurement method.

	low density		high density	
	g (nm)	h (nm)	g (nm)	h (nm)
AdG[a]	11.0	35	8.5	38
MWC[b]	9.2	38	7.2	43
exp[c]	9.0	34	7.5	41
noise-based	–	16	–	20

[a] Alexander–de Gennes
[b] Milner–Witten–Cates
[c] exponential approximation to AdG

widest range of distances and forces, despite actually being an approximation to the full AdG equation. It is also immediately visible that the exponential equation is indeed a valid approximation to the AdG equation at intermediate distances.

Table 3.3 shows the obtained grafting distances and brush heights from best fits for all three equations and brush heights from the noise-based method. The MWC and exponential approximation equations yield very similar values, the AdG equation produces significantly larger grafting distances. Due to its nature, the noise-based method yields the lowest brush heights and no grafting distance data. The values obtained are consistent with the expectation that the high grafting density conditions (as measured by SPR) yield a higher grafting distance and larger brush height from the AFM force curve fits, compared to the low grafting conditions. When comparing to SPR data, we note that the AFM fits yield much larger grafting distances. The brush height extracted from the force curve fits matches the SPR value for high grafting density conditions, but is much larger for the low density case.

3.6 PEGylated Au nanoholes

Nanohole arrays (Figure 3.14) correspond quasi to inverted nanoring systems, and are especially useful as plasmonic sensors [96, 97]. We used AFM force spectroscopy to investigate an Au nanohole system with hole diameters of $\sim$115 nm (measured by SEM) and hole depths of $\sim$25 nm (measured by AFM). We compare the effect of PEGylation on these nanoholes with our previous measurements on the similarly sized nanorings. As the spatial localization of analytes in the nanoholes can be measured in a plasmonic sensor setting, it is especially interesting to see how PEGylation of the nanohole array might influence the access of analytes to the nanohole "interior". PEGylation of the sample was performed as with the nanorings, using mPEG-SH which covalently binds to the Au surface and the inner walls of the nanoholes (Methods section 2.2.2). Two different PEG molecular weights, 10 kDa and 20 kDa, were used to PEGylate the nanohole array at cloud point conditions, leading to a high grafting density of PEG on the surface ($g_{SPR,10k} = 1.6$ nm; $g_{SPR,20k} = 2.2$ nm). As our previous measurements with the nanorings showed, the PEG-thiol only binds to gold and not to glass. Thus the bottom glass surface at the center of the nanoholes remained free of attached chains.

Fig. 3.15 shows force volume maps (32×32 pixels, 300 nm $\times$ 300 nm) of three different nanoholes: an unfunctionalized one, and those functionalized with 10 kDa and 20 kDa PEG, respectively. The topography maps (left panels in Fig. 3.15) show a clearly distinguishable nanohole in each case. The brush contact height maps (right panels) visualise at which height relative to the Au surface the AFM tip encountered steric repulsion by the PEG brush. Values above 0 nm mean that the brush is felt before the tip crosses the Au surface plane while values below 0 nm indicate that the tip has entered the hole before coming in contact with a brush. Since there is no brush in the unfunctionalized sample, contact occurs only at the hard-wall surface, and thus the contact height map tracks the topography map. For the functionalized samples, a brush can be measured on the whole Au surface, with the 10 kDa brush being less high than the 20 kDa one, as expected.
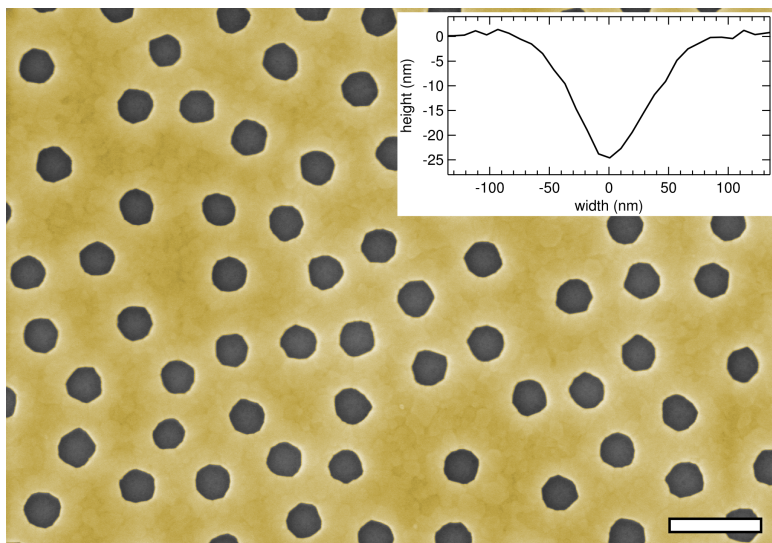
FIGURE 3.14: False-color SEM image of an Au nanohole array (yellow: Au surface; grey: bottom glass surface of nanoholes). Scale bar, 300 nm. Inset: Cross-section of a single nanohole measured by AFM. Tip convolution makes the edges appear inclined although they are steep in reality.

An interesting difference between the two brushes can be seen over the nanohole itself. With 10 kDa PEG, the brush contact height is <0 nm at the centre of the hole, while with 20 kDa PEG the contact height stays above 0 nm even at the very centre.

Fig. 3.16 shows the brush height for each force curve taken on the FV maps. Because the pyramidal AFM tip interacts with the nanohole walls, the measured depth of a nanohole increases as the tip moves towards the center (even though the holes have steep walls in reality). This allows to discriminate measurements at the edge of a nanohole and at the center. These areas are coloured correspondingly in Fig. 3.16.

The brush height is plotted in two different ways. First, we show the brush contact height (Fig. 3.16a, corresponding to the FV maps in Fig. 3.15). It can be seen that without PEG, the data follows the hard-wall line, while the PEGylated samples show a brush contact point above hard-wall. The 10 kDa PEG brush does not extend enough over the whole nanohole, so that the contact point dips below the Au surface already at the edges of the nanoholes. With 20 kDa PEG, the brush stays above the Au surface the whole time. Fig. 3.16b shows the brush height
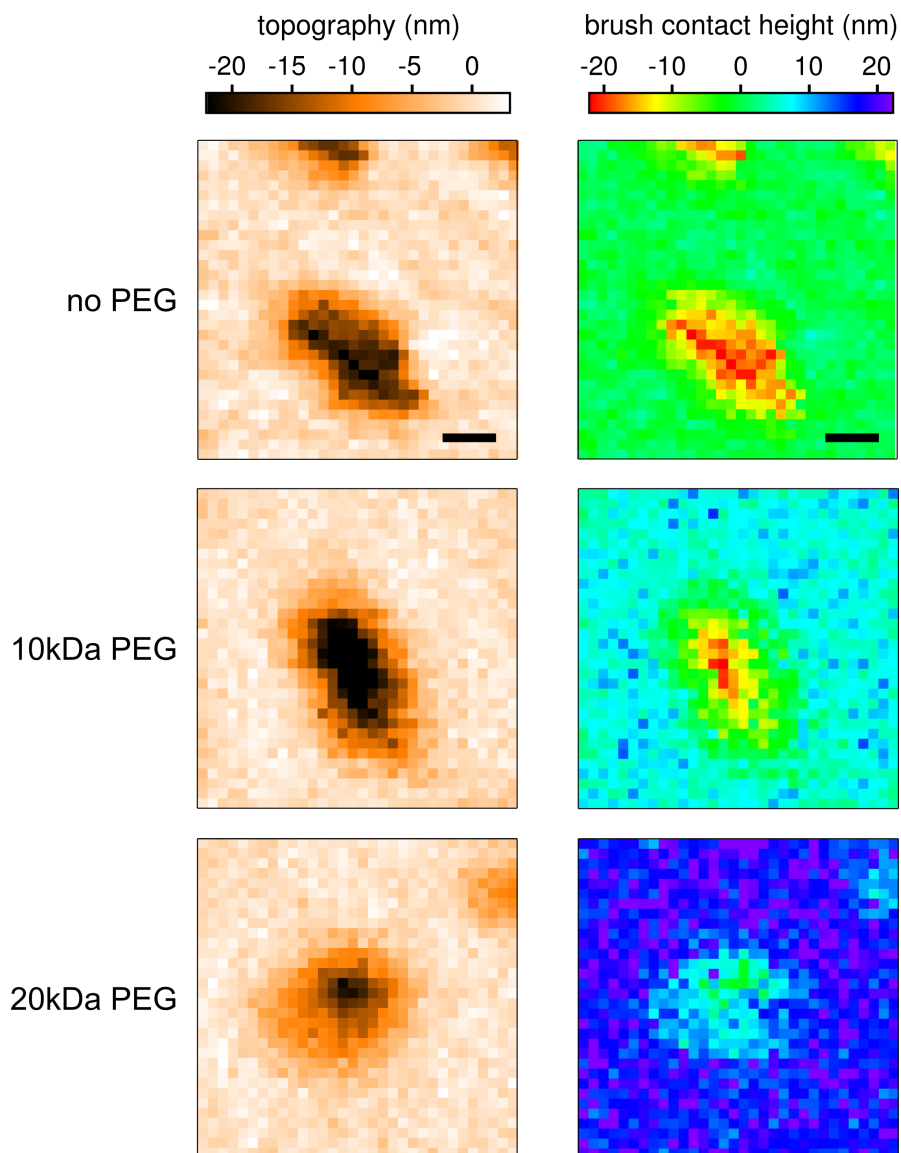
FIGURE 3.15: Force-volume maps of nanoholes (32×32 pixels, $300\,\text{nm} \times 300\,\text{nm}$), unfunctionalized and functionalized with $10\,\text{kDa}$ and $20\,\text{kDa}$ PEG. The left panels show the hard-wall topography of the Au surface and the nanohole. Deviations from circular shape of holes are due to limited pixel resolution and drift in the measurement system. The right panels show the brush contact height relative to the Au surface, i.e. the height at which the brush is felt by the AFM tip, with the Au surface set to $0\,\text{nm}$. Scale bar, $50\,\text{nm}$.
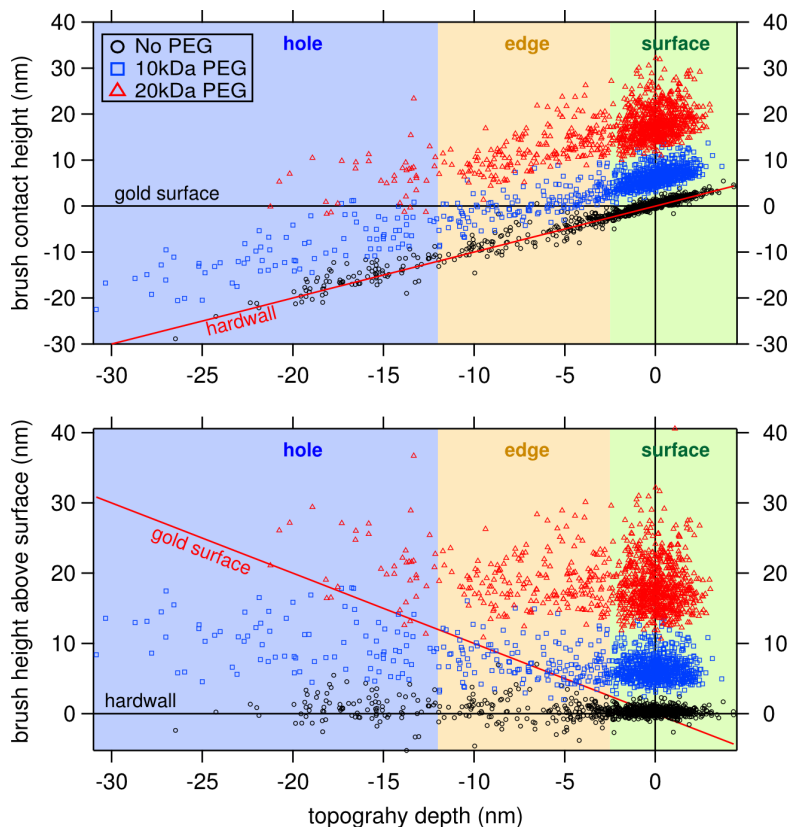
FIGURE 3.16: Scatterplots of brush heights vs hard-wall topography depths from force curves taken over bare and PEGylated Au nanoholes. Depths >0 nm correspond to the Au surface, while data points <0 nm correspond to force curves taken at the nanohole edges and over the hole. Each symbol represents a single force curve. The same data is plotted here in two different views. **(a)** Brush contact height, i.e. the brush height compared to the Au surface, which is set as 0 nm. **(b)** Brush height above hard-wall, i.e. the hard-wall position at each pixel is set as 0 nm. This representation corresponds to the brush height measurements shown for nanorings.

relative to the hard-wall position of each pixel, meaning to the Au surface outside the holes and to the glass basal surface when ramping over the holes. These relative brush height values are equivalent to the brush height analysis performed on the nanoring samples.

We find that without PEG, the algorithmically calculated "brush height" on the Au surface stays within 0.3 nm ± 0.5 nm, i.e. there is no interaction between surface and tip except for the eventual hard-wall contact. With 10 kDa PEG we measure a brush height of 6.4 nm ± 1.7 nm above the Au surface, and with 20 kDa PEG the brush height is 18.1 nm ± 3.6 nm above the Au surface. As expected, the brush height is considerably less with the shorter PEG chains. The value for 20 kDa PEG

agrees well with our measurements on the Au nanorings. The brush height stays relatively constant at the edges and over the nanoholes as well, with a possible slight increase as the tip probes the centres of the holes. Appendix A shows raw force curves recorded over the nanohole surfaces.

3.7 Discussion

The DLS measurements confirm the physical basis of increased grafting density upon cloud point grafting. At cloud point conditions we see clearly that the PEG coils collapse to very small diameters. The cloud point conditions we use are just below a phase transition towards aggregated PEG chains, as can be witnessed by eye when observing the clouding of the PEG solution upon crossing the cloud point. Indeed, the DLS correlation measurement data at cloud point conditions cannot be fit nicely at large time scales (which correspond to larger particles in solution). This might be already a sign of aggregates forming, although the number at our conditions is still sufficiently small as not to disturb the main measurement.

The SPR measurements show that we can tune the grafting density of PEG grafted to an Au surface from a mushroom regime up to a very dense brush regime by changing (a) the grafting solvent, or (b) the PEG concentration. Even though a polymer brush is already formed in good solvent grafting conditions (i.e. H_2O or PBS), the brush density is markedly increased upon using cloud point grafting conditions with Na_2SO_4 in the solvent (up to threefold increase in chain density for 20 kDa PEG). We can see a clear dependence of the final PEG grafting density on the concentration of Na_2SO_4 we use. As Table 3.1 and Fig. 3.4 show, keeping the same PEG concentration, the average grafting distance increases from 2.8 nm to 2.2 nm as we go from 0.6 M to 0.9 M Na_2SO_4. This is a significant increase in an already highly dense brush state. On the other hand, the PEG concentration does not play a large role in the final grafting density for a very wide range of concentrations. Only as the PEG concentration is heavily reduced (3 – 4 orders of magnitude below the cloud point concentration) an effect becomes visible on

the grafting density, as the adsorption from solution to the Au surface occurs most likely much slower than for higher concentrations. A similar effect has been previously measured with PEG grafted from PBS solvent [98].

The SPR height measurement method by using non-interacting particles as molecular layer height probes (in our case the protein BSA) was previously used to measure the height of 20 kDa PEG grafted from good solvent [86]. Our measurements agree with the published results, and we further show that increased density leads to a significantly higher brush. A doubling of the brush height is observed when the average grafting distance is reduced by a factor of two.

AFM measurements on Au nanorings confirm that the general SPR findings are also valid on the nanoscale. PEG grafted from solution forms a brush on the nanorings which interestingly also occludes the central pore of the rings, although no PEG chains are grafted directly at the pore. This means that chains must extend from the inner walls and edges towards the centre, as has already been previously demonstrated [20].

Our AFM force spectroscopy measurements show lower brush heights compared to SPR, especially at higher grafting densities. A general underestimation of the physical brush height is an effect of the brush height measurement method where we detect the brush when its repulsive force on the cantilever exceeds the AFM noise threshold, at which point the tip has already slightly compressed the brush. The AFM tip is also known to splay the brush upon indentation, which further reduces the apparent height of the brush [99, 100].

We note that while in SPR a doubling of the brush height from low to high brush density was measured, in the AFM measurements the increase is only 20 %. Because the denser brush should actually provide a larger repulsive force against the tip, we conclude that most likely the change of grafting conditions from PBS to 0.9 M Na_2SO_4 leads to an increase in grafting density but not by the same amount as in the SPR setup. The peculiar geometry of the nanorings and the nanoscale size of the rings itself could play a role here.

To circumvent the fact that the outer, most-extended, parts of the brush can't be detected by AFM due to limits in sensitivity, we fitted our data with theoretical equations of surface-attached polymer brushes compressed by a spherical tip. The fits give an extrapolation beyond our noise limit to assess the full physical height of a polymer brush, together with providing an average grafting distance which we again can compare to SPR data. The theoretical AdG and MWC force equations were originally developed for parallel plates pushing on each other and later adapted for a spherical AFM tip. It is immediately visible that the AdG and MWC curves are a poor fit to our AFM data at high compression forces. The approximations used apparently break down when the tip is near the surface. Interestingly, the exponential approximation to the full AdG equation fits our data the best. All theoretical fits lead to too large average grafting distances. At low density grafting conditions, the values of $g \approx 9 - 11$ nm are similar to or even larger than the polymer hydrodynamic size, which would not lead to a brush formation, but a clear brush is measured by AFM. Again we see that the equations developed for large macroscopic surfaces pushing towards each other do not correctly scale down to the AFM tip dimensions. As expected, the brush heights provided by the theoretical fits are larger compared to the values obtained from our noise threshold-based analysis method. Curiously, while at low density the noise method matches more closely with the SPR results, at high density the theoretical fits yield heights closer to SPR data. In no case do we find such large differences between low and high density grafting conditions with AFM as with SPR. This again indicates that the real grafting densities achieved on the nanorings do not differ as much as in SPR incubations under same conditions.

Finally, we show by probing PEGylated nanohole arrays that AFM force spectroscopy of polymer-functionalized nanoscale structures is generally applicable to various samples. Using the nanohole arrays we show that by functionalizing nanopore-like structures with PEG of different molecular weights, qualitatively different results can be obtained. With 10 kDa PEG we showed that the nanohole inner volume remains accessible by the AFM tip, while grafting 20 kDa PEG blocks the access to the hole (the AFM tip feels the repulsive effect of the PEG

brush already above the hole entrance). This is presumably also true for any particle of size on the order of the AFM tip radius (i.e. $\sim$30 nm) or larger. This effect could be used for size-exclusion filtering or providing selective access to nanoplasmonic-based sensor elements (e.g. nanoholes) [97].

Chapter 4

Behaviour of Nanoscale PEG Brushes under Confinement

4.1 Locally distinct geometries on Au nanorings

In this chapter, our interest lies in how polymer chains in a brush behave under compressive load. Especially intriguing is the difference between a brush on a flat surface and in a nanopore-like geometry. To probe both configurations on the same sample, we used our Au nanorings fabricated on glass substrates, functionalized with 20 kDa mPEG-SH. AFM force spectroscopy was used to measure observables of interest, such as the local brush height and the brush stiffness, as well as dynamic confinement effects upon compression of the brush.

On a single Au nanoring with an outer diameter of ~ 400 nm, inner diameter of ~ 100 nm and a height of ~ 30 nm we distinguish between two different nanostructural domains: (a) a large (compared to the characteristic length scale of individual polymer chains) flat area over the main ring structure, and (b) a nanopore-like environment at the centre of the ring. Fig. 4.1 shows a to-scale drawing of a PEG-covered nanoring and the probing AFM tip. The two main regions of interest are marked as "hole" and "ring" regions. As can be seen from the drawing, probing the ring region corresponds to compressing a uniform polymer brush by the

tip apex. In comparison, when probing the hole region, the compression doesn't happen strictly perpendicularly to the brush grafting surface and is possibly combined with shearing of the chains which are attached to the side walls. Thus, we should expect different static and dynamic behaviours between the hole and the ring region. We assess this by probing the two different regions of the nanoring at varying loading rates (i.e. tip approach velocities) ranging from $0.4 - 29\,\mu m/s$. We compare the apparent local brush heights and stiffnesses, as differences in brush conformation and dynamics should be visible in these observables over our range of velocities which span two orders of magnitude.
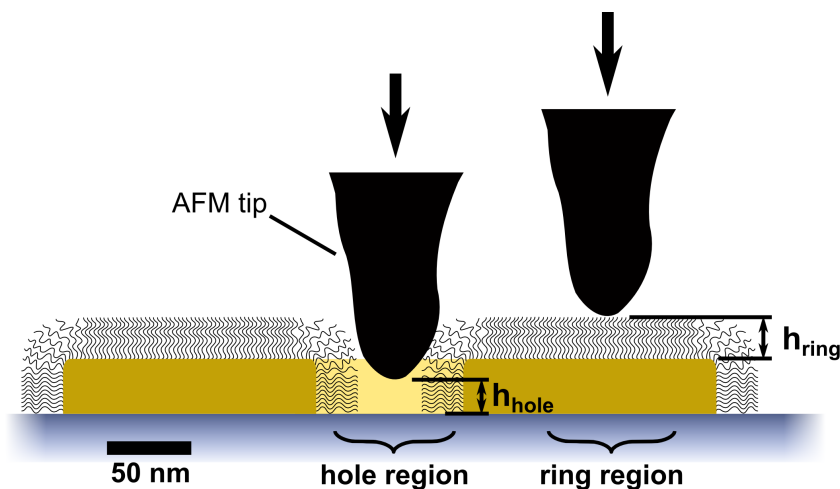
FIGURE 4.1: To-scale schematic of an AFM tip probing an Au nanoring with a PEG polymer brush grafted on it. The tip size and lateral nanoring dimensions are based on SEM images, while the nanoring and brush heights are measured by AFM. Two distinct regions can be analysed: the flat "ring" region, and the "hole" region with a nanopore-like geometry. Even though no molecules are grafted to the center of the hole, due to the finite size of tip and hole and the extension of the chains of the polymer brush, the tip feels the brush well before reaching the bottom surface, resulting in an apparent brush height there (h_{hole}).

4.2 Brush height under varying loading rates

$20\,kDa$ mPEG-SH was covalently grafted on the nanorings at cloud point conditions ($0.13\,mg/ml$ of PEG in PBS / $0.9\,M$ Na_2SO_4). Under these conditions, the resulting average grafting distance between chains measured by SPR was $g_{SPR} = 2.2\,nm$. The average brush height over the ring measured by AFM with

our standard noise-based method (see Methods, section 2.2.6) at intermediate tip velocities ($3.4\,\mu m/s$) is $20.4\,nm \pm 8.4\,nm$, which is somewhat lower than obtained from the SPR measurements (see chapter 3 for details). We have to keep in mind that we slightly underestimate the brush height, but nevertheless our method allows robust and accurate relative comparison of brush heights and morphologies under varying compressive and confining conditions.

Fig. 4.2 shows histograms of measured brush heights over the hole and the ring regions, respectively. The data (from 3 different samples with total $N_{nanorings} = 13$, and $n_{hole} = 533$ and $n_{ring} = 650$ individual force curves per loading rate) can be well fitted with Gaussian distributions. In the hole region, we see a clear trend of decreasing apparent brush heights with increasing loading rates. A similar but much weaker tendency appears over the ring region. Plotting the means of the Gaussian fits vs the loading rates (Fig. 4.3) shows more clearly that at low loading rates up to $1\,\mu m/s$ the brush height is $26\,nm$, after which it gradually decreases down to $14\,nm$ over the hole and to $19\,nm$ over the ring. For the hole region this is a decrease of $43\,\%$, and $26\,\%$ over the ring. Note that at equilibrium, i.e. when the AFM tip is far away and not in contact with the brush, the brush height doesn't change. The measured difference is in the apparent brush height upon compression and stems from the dynamic interaction between the tip and the brush.
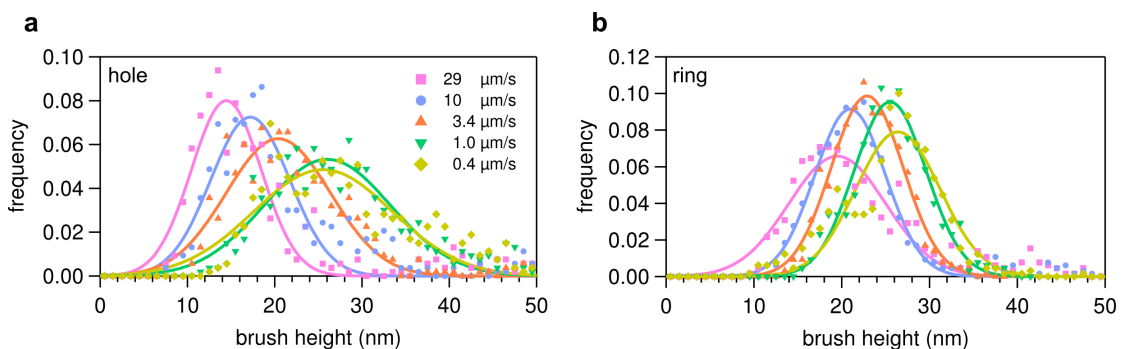
FIGURE 4.2: Combined histograms of brush height measurements for loading rates between $0.4 - 29\,\mu m/s$ (symbols). Solid lines are Gaussian distribution fits to the data. **(a)** hole region **(b)** ring region.
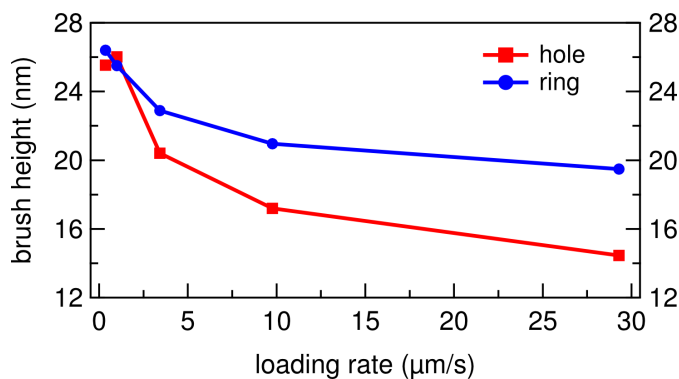
FIGURE 4.3: Mean apparent brush heights extracted from Gaussian fits to the experimental data (see Fig. 4.2).

4.3   Brush stiffness under varying loading rates

Fig. 4.4 shows the histograms and Gaussian fits for the linear stiffness of the brush, calculated as the gradient in the force curve between repulsive forces of $50 – 150\,\text{pN}$ (for detailed explanations of the stiffness measurement algorithms, see Methods section 2.2.6). This force region lies between the first contact with the brush and the hard-wall grafting surface, i.e. we measure directly the repulsive action of the brush. The Gaussian means vs loading rates are plotted in Fig. 4.5. At the hole, the linear stiffness increases above a certain loading rate threshold, while at the ring, no significant trend can be extracted at the accessible rates in this experiment. Interestingly, at low loading rates the brush over the hole appears softer than over the ring, but as loading rates increase we see a cross-over, with the polymer chains ending up being stiffer over the hole. This illustrates the different brush confinement dynamics in flat and nanopore-like geometries.
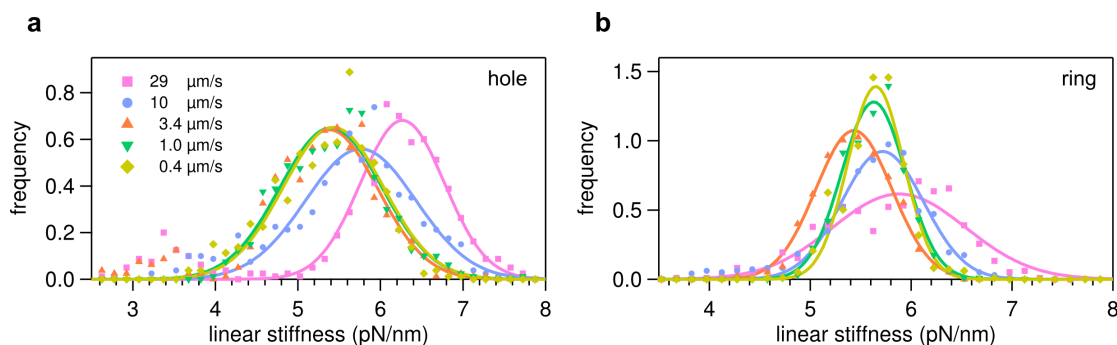
FIGURE 4.4: Histograms of the linear stiffness measured at varying loading rates (symbols). Solid lines are Gaussian fits to the data. **(a)** Hole region. **(b)** Ring region.
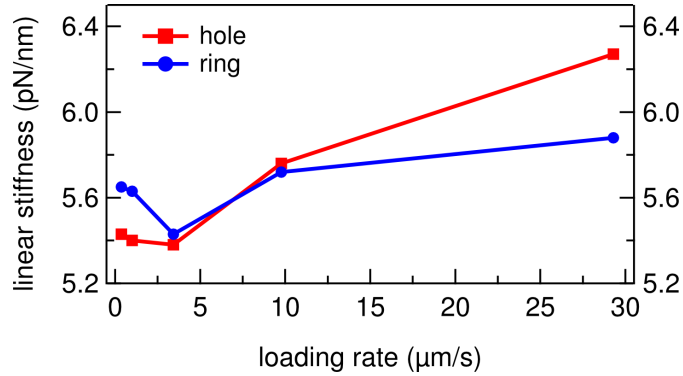
FIGURE 4.5: Linear stiffness means extracted from Gaussian fits to experimental histograms from Fig. 4.4.

To complement the brush characterization, we used a second, independent method of assessing the brush stiffness. We regard the brush as a compliant isotropic film and fit our force curves with the Hertzian contact model. This allows us to extract the Young's modulus of the film which is a measure of the brush stiffness (Methods section 2.2.6). The force curves can be fitted well by using two distinct regions in the indentation of the brush which have different Young's moduli. Region 1 is the softer part following brush-tip contact with a measured Young's modulus (E_1) of around $0.1\,\mathrm{MPa}$. Region 2 is ca. tenfold stiffer with $E_2 \approx 1\,\mathrm{MPa}$ in the more compressed part of the brush, up to the hard-wall contact. The presence of two distinct regions when applying the Hertz model has been shown in earlier work of PEG grafted on flat Au surfaces, yielding very similar values for the Young's moduli [101]. Qualitatively the observed results match with the following model: at weak compression near the top of the brush the PEG chains are flexible, disentangled and have low monomer density [7], which gives a low elastic modulus. Upon stronger compression, the chains become more confined and possibly correlated or entangled, which leads to a significantly stiffer behaviour and is visible as the tenfold increased elastic modulus. This cross-over from soft to stiff behaviour occurs $\sim 10\,\mathrm{nm}$ above the hard-wall surface. We should note that the Hertz model of an isotropic compliant half-space is a very crude approximation of a surface-grafted polymer brush and also does not take substrate effects into account. Nevertheless the fitted Young's modulus values can be used for relative comparisons, and our E_2 measurements give same order of magnitude results as

bulk Young's modulus measurements of PEG hydrogels [102].

Fig. 4.6 shows the means for E_1 and E_2 as extracted from Gaussian fits to histograms, plotted against the loading rate, for the hole and the ring regions. E_1 increases slightly with increasing loading rate in both the hole and the ring regions, but the dependence is weak. Over the hole, E_1 is consistently softer than over the ring for all loading rates. For E_2 we see similar results as with the linear stiffness measurement. Over the ring E_2 stays mostly unchanged (a decrease of 17 % from the lowest to highest loading rate), whereas there is a doubling of the elastic modulus over the hole from the lowest to the highest loading rate. At low loading rates, E_1 in the hole region appears softer than in the ring region (as for the whole loading rate range with E_1), but ends up being stiffer at high loading rates.
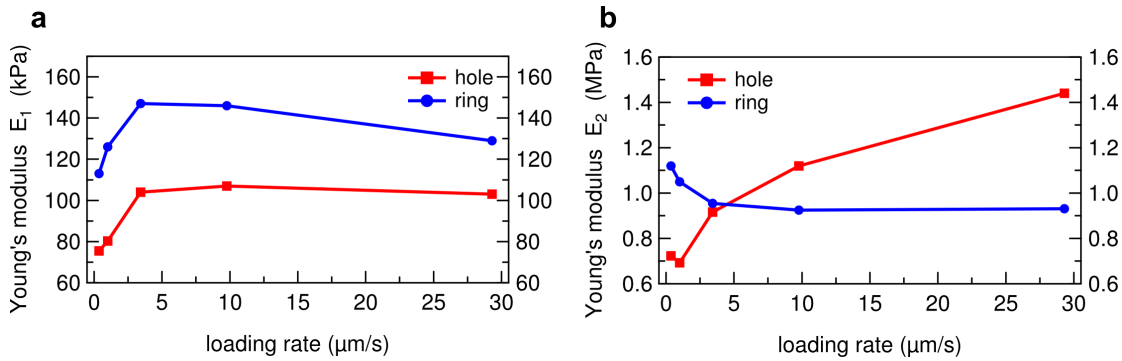
FIGURE 4.6: Mean Young's moduli from region 1 (E_1, **a**) and region 2 (E_2, **b**) of the compression force curves over the hole and the ring.

Finally, Fig. 4.7 shows overview force volume maps of a single nanoring with the ring topography and the calculated brush height, linear stiffness and Young's modulus values. The force curves in this map were taken at 4.9 µm/s tip approach velocity. Comparing the values at the central hole and over the ring in the FV maps, good agreement can be seen to the data shown above which was taken in point-and-shoot mode (see Methods, section 2.2.5) with much higher number of force curves than could be extracted from a 32×32 pixel FV map. The linear stiffness is slightly lower at the hole compared to the ring surface, whereas E_1 is clearly less at the hole (compare to Figs. 4.5 and 4.6a). E_2 shows large inhomogeneities over the map, but on average the hole and ring stiffness are very similar.

The brush height in the FV map is larger at the hole, which does not correspond to the data shown above (Fig. 4.3). This might arise from statistical fluctuations and the low resolution compared to accurate probing of the central hole in point-and-shoot mode, which again demonstrates the need for high volume and high spatial precision recording of force curves.
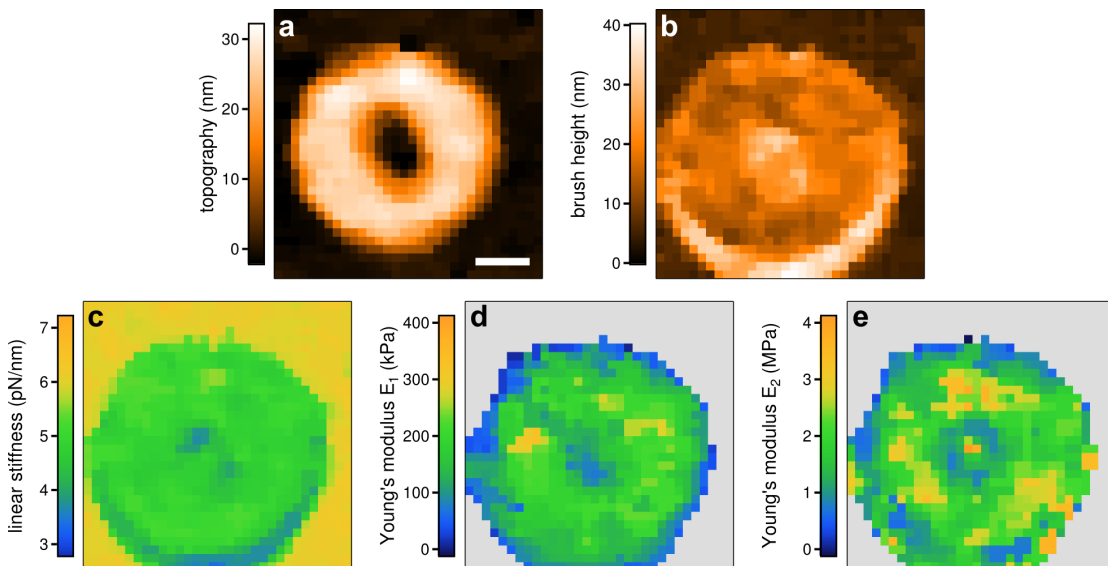
FIGURE 4.7: Force volume maps of a single nanoring display various observables of interest. Force curves were taken at an intermediate tip velocity of $4.9\,\mu m/s$. **(a)** Topography. **(b)** Brush height. **(c)** Linear stiffness. **(d)** Young's modulus in force curve region 1. **(e)** Young's modulus in force curve region 2. For the Young's moduli, no useful fits could be performed on glass; this unanalysed region is marked in grey. Scale bar, 100 nm.

4.4 Escape transition effects upon PEG compression

Upon compressing the PEG brush, we noticed that some of the recorded force curves show a jump or discontinuity in the repulsive force which resembles the behaviour predicted for a polymer escape transition of single chains (Fig. 4.8; see section 1.4.4 for an overview). We conducted further investigations of this effect, comparing possible influencing factors such as ring and tip geometry, and brush grafting density. Samples of two different nanoring geometries were prepared: rings with a large central hole of $\sim 100\,nm$ diameter, and rings having

a small central hole of ~50 nm diameter (the other dimensions were identical, i.e. ~400 nm outer diameter and ~30 nm height). 20 kDa mPEG-SH was grafted to the rings under different conditions resulting in different grafting densities of PEG chains. We then performed AFM force spectroscopy measurements on these samples in PBS solvent, using two different AFM cantilever models with distinct tip geometries.
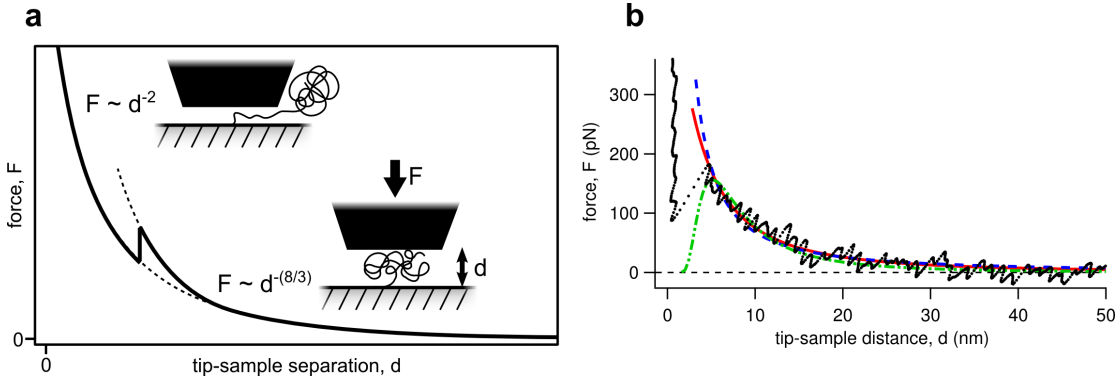
FIGURE 4.8: **(a)** Predicted force curve from scaling theory. The cartoons show schematically a confined but unescaped polymer chain, and an escaped chain with a stretched tether. Scaling analysis predicts that in a good solvent, before the escape transition the force increases in proportion to $d^{-8/3}$, and after escape proportional to d^{-2}, with a sudden jump (first-order transition) in between. **(b)** A typical force curve showing an escape transition (black dots). Fits to the data: power law $F \sim d^{-1.4}$ (dashed blue line); power law with additional offset in the hard-wall position $F \sim (d - d_0)^{-2.2}$ with $d_0 = -6$ nm (solid red line); best fit to the theoretical scenario of many mobile mushrooms, Eq. 4.3 (dash-dotted green line).

Our recorded transitions occur in the sterically repulsive part of the force curve, i.e. while the tip is physically compressing the brush and before the tip has reached the underlying hard-wall Au substrate. Comparison to the predicted force vs distance relationships from scaling theory shows that before the transition the force curves can be fitted with a power law,

$$F(d) \sim d^{-\nu} \tag{4.1}$$

where $F(d)$ is the force acting on the tip at distance d from the grafting surface. The best fit produces $\nu = 1.4$. This does not match the prediction for a single mushroom under compression from scaling theory, where for good solvent, $\nu = 8/3 \approx 2.7$ [54]. Because we are compressing a brush with an AFM tip, instead of

the theoretical compression of a single chain by a cylindrical piston, deviation in the power law exponent is expected. We can account for a possible offset in the hard-wall position by adding another fitting parameter d_0. With

$$F(d) \sim (d - d_0)^{-\nu} \tag{4.2}$$

we get $\nu = 2.2$ and $d_0 = -6\,\text{nm}$. This exponent can be better reconciled with the theoretical models and lies between the scaling analysis predictions for a mushroom, $\nu = 8/3$, and for an immobile brush compressed by a piston, $\nu = 2$ [56]. At the transition, in almost all cases the tip jumps directly to the grafting surface which is seen as being infinitely stiff by the AFM tip. This is in contrast to the predicted $F(d) \sim d^{-2}$ dependence after transition. In the literature we further find calculations of a system of many mobile surface-grafted mushrooms below a compressing obstacle [54, 56]. In that case we have a repulsive power-law force which decreases exponentially below a certain "yield stress" (i.e. threshold distance), when the mobile chains move out from under tip completely. The resulting force curve has the form

$$F(d) \sim d^{-8/3}e^{-Ad^{-5/3}} \tag{4.3}$$

and can partially be fitted to our data as well, as Fig. 4.8b shows. Additional force curves with escape transitions are shown in Appendix A (Fig. A.4).

4.5 Role of local geometry for escape transitions

Our two nanoring geometries provide different ratios of the central hole width compared to the size of the flat region on the Au ring itself. We can use this to investigate the influence of geometrical factors on the escape transitions. By recording force volume (FV) maps of 32×32 force curves over one nanoring, the escape transition occurrences can be spatially resolved as a function of their lateral position on the ring. Because we assumed that the PEG grafting density and the

AFM tip shape might play an important role in the transition effect, we performed measurements with two different cantilever types (henceforth called HYDRA, having a sharp tip with ca. $15 - 20$ nm tip radius; and OBL with a broader tip, ca. $25 - 40$ nm radius), and at two different grafting densities, denoted low and high densities. The low grafting density conditions were achieved by incubating the sample in 40 mg/ml of 20 kDa PEG in PBS (average grafting distance between chains on the surface, as measured by SPR, $g_{SPR} = 4.1$ nm), and the high grafting density by incubating 2 µg/ml PEG in 0.6 M Na_2SO_4 in PBS ($g_{SPR} = 2.9$ nm).

Fig. 4.9 shows the occurrences of escape transitions over nanorings with a small central hole using the two different AFM tips. To our surprise, the probability for an escape transition is very similar all across the nanoring. Apparently the position of the chains with respect to the edges and the central hole does not play a big role in allowing escape transitions to occur. Unfortunately, tip interactions with ring side walls induce too much noise into the force curves to allow drawing any conclusions at the very edge of the ring (i.e. the outermost pixels of the ring in the topography maps). Comparing the two different AFM tips, we measure a slightly increased probability of seeing escape transitions with the broader OBL tip: roughly in 40 % of all curves over the ring with HYDRA, and in 55 % with OBL.

When we look at the nanorings with a large central hole, using the same low grafting density and OBL tip, we see significantly fewer escape transitions, only in ~15 % of all curves over the ring (Fig. 4.10a). Again no discernible dependence on the lateral position over the ring is seen. The PEG brush also extends from the inner walls towards the centre of the hole and even though the AFM tip probing the central hole interacts with the chains, no escape transitions are measured there. We note that some local clustering of escape transition effects might be occurring (e.g. in the lower right quadrant of the ring in Fig. 4.10a). This would hint at inhomogeneities or correlations in the local ordering of the PEG chains on the nanoring, but current measurements are not sufficient to draw definite conclusions. With the small hole nanorings (Fig. 4.9) such clustering would not be visible due to the overall high density of escape events.
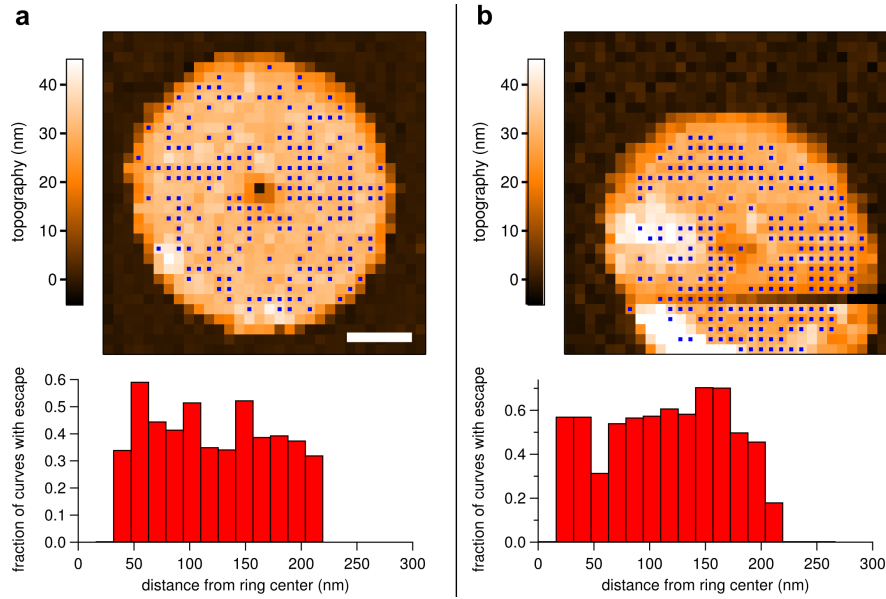
FIGURE 4.9: Escape transitions for nanorings with a small central hole (50 nm diameter) at low PEG grafting density ($g = 4.1$ nm). The panels show a topography map of the nanoring with all pixels exhibiting an escape transition marked in blue, and a histogram of the fraction of curves having an escape transition at a given distance from the centre of the ring. **(a)** Nanoring measured with the sharper HYDRA tip (15 – 20 nm radius). **(b)** Nanoring measured with the broader OBL tip (25 – 40 nm radius). Scale bar, 100 nm.

At high polymer chain grafting densities (Fig. 4.10b and c), the escape transitions disappear almost completely, independent of which tip is used. With only a few escape transitions per nanoring, spatial distributions and local correlations cannot be extracted.

When looking at the forces and the tip-sample distances at which the escape transitions occur (Fig. 4.11), we find differences there as well, in addition to escape event frequencies. The forces and distances cluster around a mean value for each experimental condition. For small central hole nanorings grafted at low density and measured with the HYDRA cantilever, the average transition force is 204 pN ± 51 pN and occurs at the tip-sample distance 3.2 nm ± 1.3 nm (Fig. 4.11a). For the same conditions, measured with the OBL cantilever, the transitions shift to lower forces of 95 pN ± 48 pN and to larger distances of 6.1 nm ± 2.0 nm (Fig. 4.11b). Since the repulsive force of a brush rises for decreasing tip-sample distances, transition occurrences at lower forces are consistent with them occurring at larger distances. For the large central hole sample, at low density, measured with
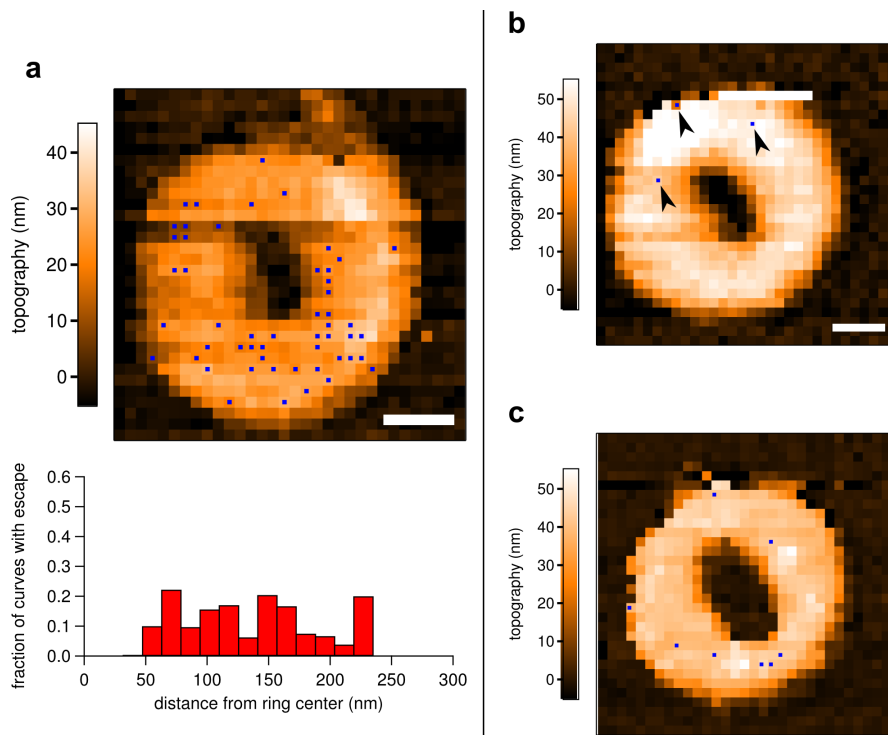
FIGURE 4.10: Escape transitions for nanorings with a large central hole (100 nm inner diameter). Topography maps show force curve pixels with escape transitions marked in blue. **(a)** Low grafting density ($g_{SPR} = 4.1$ nm), probed with an OBL tip. The histogram shows the fraction of pixels having an escape transition as a function of their distance from the ring centre. **(b)** High grafting density ($g_{SPR} = 2.9$ nm), OBL tip. Only three escape transitions were recorded (arrows). **(c)** High grafting density, HYDRA tip. Scale bars, 100 nm.

OBL, we have an average force of 134 pN ± 67 pN and distance of 4.2 nm ± 2.6 nm (Fig. 4.11c).

4.6   Discussion

4.6.1   Polymer brush response under varying loading rates

Our results show that polymer brush response to compression and confinement by a nanoscale object (here, the AFM tip) changes when different loading rates (i.e. tip approach velocities) are applied. It is notable that changes in the properties are especially visible in the "hole" region, where the PEG brush is probed in a nanopore-like geometric environment. Over the "ring" region, in the flat Au part
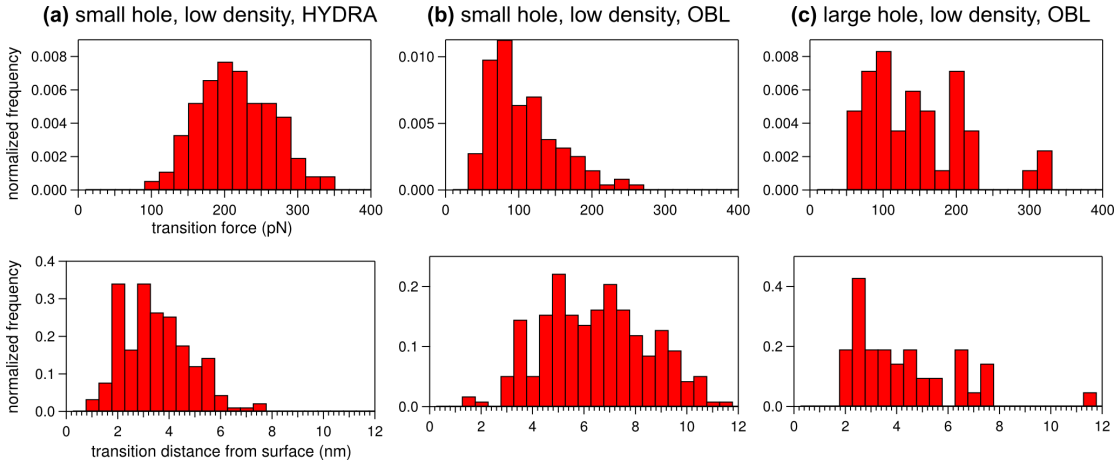
FIGURE 4.11: Histograms showing the forces and tip-sample distances at which the escape transitions occur. **(a)** Small central hole, low density, HYDRA cantilever (corresponds to Fig. 4.9a). **(b)** Small central hole, low density, OBL cantilever (corresponds to Fig. 4.9b). **(c)** Large central hole, low density, OBL cantilever (corresponds to Fig. 4.10a).

of the nanoring, the dependence on loading rate is muted or disappears altogether. The decrease in the *dynamic* apparent brush height at higher loading rates is present in both regions, but much clearer in the hole. Both the linear stiffness and the Young's modulus E_2 show strong dependence on the loading rate over the hole, but negligible dependence over the ring region. E_1 on the other hand seems to remain mostly the same over our range of loading rates, between $0.4 - 29\,\mu\text{m/s}$.

Considering our experimental system, we should check whether any viscoelastic effects on the cantilever itself could contribute to a loading-rate dependent effect. As discussed by Evans [103], a viscoelastic effect of the moving cantilever manifests itself on a characteristic time scale $\tau = \zeta/k$, where ζ is the cantilever damping coefficient and is in the order of $10^{-3}\,\text{pN s/nm}$ and k is the cantilever spring constant, in our case $\sim 8\,\text{pN/nm}$. These values lead to a characteristic response time of about $0.1\,\text{ms}$. The contact time between the brush and the AFM tip in our experiments lies between $1 - 100\,\text{ms}$ (approach part). We conclude from this that the intrinsic viscoelastic response of the cantilever is fast enough that it should not play a role in our measurements. Further, we recorded the internal Z piezo sensor signal which accurately monitors the real physical position of the piezo. By utilising this data in our force curve analysis we eliminated any nonlinear piezo effects which are always present and could otherwise introduce artefacts into our

data. Thus, our results display a true effect of the polymer brush under dynamic confinement.

Our results confirm that we have indeed two different regimes on our nanostructures, the flat and the nanopore-like part. The larger magnitude of most loading rate dependent effects at the pore leads to the following picture: At the flat areas we have only pure compression of the brush, normal to the grafting surface, while at the pore other mechanical interaction modes are present in addition to compression. As can be seen in the to-scale depiction in Fig. 4.1, when the tip is probing the centre of the pore, brush compression as well as lateral shearing is likely to occur.

Over the flat part, where we expect purely compressional effects, we measure a modest decrease in the height at high loading rates. This might stem from viscoelastic and hydrodynamic effects. Rate-dependent non-oscillatory probing of polymer brushes with a sharp AFM tip has to our knowledge not been carried out in the literature. Experiments show that probing a PEG brush with a large colloidal probe induces an additional repulsive force, and so actually a *larger* measured dynamic brush height [28]. This effect is attributed to the hydrodynamic draining of solvent between the colloid and the surface. The colloidal probes used in those experiments had a diameter of $\sim 5\,\mu m$, and so it is unlikely that a similar effect would be visible with our tips with an apex radius of $\sim 30\,nm$. Noise-based AFM probing experiment of polymer brushes show that cantilever motion can couple to viscous modes of the brush at separations much larger than the physical height of the brush [30]. This coupling was not visible in the static force profile in the same experiment (comparable to very low loading rates in our system), but it is conceivable that at high loading rates increased viscoelastic forces act on the brush even before physical contact is established and reduce the measured brush height.

Interestingly, in our experiment the dynamic height decrease is even more pronounced in the nanopore region. We can assume that similar effects as over the flat area contribute to the measured decrease, but additional effects come to play

to increase the effect size. Dissipative particle dynamics simulations have shown that under shear, individual chains become stretched laterally in the direction of shear, and the polymer brush layer height decreases with increasing shear rate [36, 104].

When performed at varying velocities or frequencies, stiffness measurements probe the internal molecular relaxation dynamics of the polymer brush [105]. We don't find significant correlations between the measured stiffness and the loading rate for chains probed at the ring region. Presumably the steric repulsion effect of a compressed polymer brush is elastic and there are no relaxation modes that would manifest themselves as a loading rate dependent change in measured stiffness. On the other hand, our measurements show that in the pore environment a definite loading rate dependency is visible. Shearing and off-normal compression can introduce possibilities for chain rearrangements and relaxations. Relaxations with a characteristic time faster than the AFM tip approach could lead to a softer brush response while those with a slower characteristic time keep the chains entangled and locked into position, thus stiffening the brush. That these additional relaxation modes are accessible in the nanopore confinement situation could explain both the softer response of the brush in the pore region compared to the ring region at low loading rates, as well as the progressive stiffening as we increase the loading rate.

It is interesting to observe that our measured elastic modulus of the brush in the weakly confining part of the force curve (E_1) is always lower in the pore compared to the ring surface. A clear loading rate dependence is difficult to extract. The results indicate that the additional shearing effects that lead to a stiffer brush response only become important at increased confinement of the chains. Previous AFM measurements with similar nanoring structures at intermediate loading rates also showed a softer brush at the pore compared to over the ring, in accordance with our results [20].

Regarding future directions of experimentally accessing polymer morphologies and

dynamics in and near nanopores, one interesting avenue concerns the possible appearance of different morphological scenarios for the polymers as the nanopore size shrinks further and reaches the scale of the polymer chains [16, 25]. In poor solvent, such strong confinement is predicted by simulations to lead to novel morphologies besides a collapse to the grafting walls, e.g. a formation of a polymer plug in the centre of the pore [25]. No predictions have been offered for the dynamics of such a plug under compression and shear.

4.6.2 Escape transition effects upon brush compression

An AFM tip has the ideal dimensions to measure a possible polymer escape transition. With the tip radius R_{tip} and the polymer Flory radius R_F, the ratio in our system is approximately $R_{\text{tip}}/R_F \approx 2 - 4$; or when compared to the grafting distance between chains, g_{SPR}, the ratio is ca. $R_{\text{tip}}/g_{\text{SPR}} \approx 5 - 10$. This satisfies the condition that the compressing obstacle should be much larger than the unperturbed chain but much smaller than a stretched-out chain [59]. Because a single mushroom is very difficult to access experimentally, our experiments have focused on checking whether any escape transitions can occur within a polymer brush instead. Our AFM measurements show that when compressing a PEG brush, sudden transitions in force can indeed occur. These discontinuities resemble the theoretical descriptions of polymer escape transitions. Before the transition point, the force as a function of the distance to the grafting surface can be fitted with a power law, but the obtained exponent does not match the analytical calculations or simulation results for a single confined chain ($\nu = 1.4$ from best fit instead of $\nu = 8/3 \approx 2.7$). This is to be expected, since the ideal compression of a single mushroom is rather far away from the experimental situation of an AFM tip compressing a polymer brush. Jimenez and Rajagopalan performed simulations that show a transition when compressing a brush, but no force scaling relationships were provided which could be compared to the current data [71].

Our measurements deviate further from the analytical models and simulations by showing a direct jump to hard-wall contact at the escape transition. Calculations

show that compressing the stretched tether of the escaped polymer chain should result in a force following a d^{-2} power law [54, 67, 68]. The direct jump to hard-wall could be explained by a modification of the escape mechanism. One can imagine that if the polymer chains on the Au surface are mobile enough, they can completely move out from under the compressing tip after the initial transition in order to further decrease the total energy. This would lead to the tip jumping to hard-wall contact, as we see in our data. After retracting the tip, the increased local crowding just outside the tip-surface contact area would lead to a "back flow" of the chains and reformation of the original brush state. While calculations and simulations involving chains that can move or splay from under the compressing obstacle do not show an escape transition, they do describe a lower force response compared to a brush of fixed chains [56, 70]. This behaviour seems to be confirmed by our data which shows a less steep power law scaling than predicted for mushrooms or immobile brushes. Other AFM brush compression experiments have also shown this effect [99].

Calculations have been performed of systems where many mobile surface-grafted mushrooms are compressed by a large piston. In such a scenario there is a maximal repulsive force ("yield stress") after which the force decreases as the mushrooms move out of the obstacle's way and the system becomes totally squashed [54, 56]. However, similar scenarios with brushes have not been shown. The same mobile many-mushroom system was considered with additional attractive van der Waals forces present and it was concluded that for many real situations the mushrooms are ineffective in providing a steric barrier against the compressing piston and thus no maximum in force would be visible. It is conceivable that a similar evacuation mechanism could be present with a brush, but the much denser brush succeeds in providing an adequate barrier to the piston, thus showing a maximum in compressive force before snapping in to the grafting surface due to van der Waals forces. This might lead to force curves like we see in our data.

A striking result is the disappearance of escape transitions at high grafting densities of the brush. This is intuitively easy to understand, as a less dense brush provides enough available space for an escape or evacuation mechanism of some

sort, while a dense brush lacks the space. In the dense case we then have pure compression of the brush. These results can reconcile the presence [26] and absence [106] of escape transitions in various AFM polymer brush compression experiments in the literature.

Our spatially resolved maps of 3D nanopore-like geometries show that across a single ring the probability for an escape transition is approximately constant, independent of where on the nanoring we compress the brush. This is surprising, since it should not be expected that the brush has exactly the same morphology near the walls of the ring and far away from them. We note that over the central hole we rarely see an escape transition, and it was not possible to reliably determine whether an escape transition occurs at the very edges of a ring (within $\sim \pm 10\,\text{nm}$ from the edges). More sensitive measurements might still reveal local geometry effects here.

Although there were no variations in the occurrence of escape transitions within one ring, geometrical effects became visible for different combinations of the nanoring and tip geometry. Any AFM measurement is always the result of the convolution of the sample and tip geometries, and here this seems to influence the occurrence of escape transitions. As an example, in Fig. 4.9 the signature of the sharper HYDRA tip is visible by the better resolved $50\,\text{nm}$ wide central hole, whereas the hole is almost too narrow to be resolved by the broader OBL tip.

As a result we see an elevated number of escape transitions with the OBL tip even though the nanoring sample is the same. That this is not a pure tip effect becomes clear when we look at nanorings with the larger central hole (Fig. 4.10a). Here we see a clearly reduced amount of escape transitions over the ring with the OBL tip, all grafting and measurement conditions and materials being the same as for the small hole samples. The following emerging pattern can be seen in the presented force volume maps: the larger the "flat" area of the ring as seen by the compressing tip is, the more probable are the escape transitions. The exact mechanics leading to this result remain unclear at the moment, but it seems feasible that chains could have correlations across the whole of the nanoring (some

tens of nanometres, corresponding to as few as a hundred polymer chains) that influence the accessible states of the particular polymer chains under compression.

Another tip effect becomes visible when we look at the forces and distances at which the transitions occur. The easier the chains can escape beneath the compressing tip, the lower the force will be at which the transition occurs and the earlier (at larger tip-sample distances) it will occur. The chains escape at higher forces and smaller distances for the HYDRA tip than for the OBL tip. Here the tip geometry might play a major role in determining the escape force and distance. A more detailed study with a complete set of different AFM tips vs nanostructured samples is warranted to further elucidate the behaviour these first results regarding tip and ring geometry show.

Chapter 5

Synthetic Protein Targeting with Nanoscale PEG Targets and PEG Antibodies

5.1 Introduction

Considerable efforts are being made in biomaterials and biointerface science to engineer biocompatible materials that exhibit recognition and specificity [44, 45, 107–109]. According to Elbert and Hubbell [44], this refers to the ability to "endow an entirely synthetic material with the biological recognition characteristics of biological macromolecules". Lying at the intersection between biology and materials science, biorecognition materials not only are important for exerting control over biological processes (e.g., tissue regeneration) [110] but are envisaged to impart bioinspired functionality in technological systems [45, 107].

An area that is of important practical benefit lies in how biorecognition materials can regulate molecular sorting and precision immobilization in complex biological fluids [44, 107, 109, 111]. To put this in perspective, the way specific proteins are sorted and delivered to exact spatial locations (e.g., organelles) within the complex environment of the cell (i.e., protein targeting) [112] is physically unprecedented. One problem lies with protein denaturation on engineered surfaces [113] that often leads to non-specific contamination and fouling. For instance, protein microarrays where surface-immobilized proteins capture analyte molecules from solution are known to suffer from these effects [111, 114]. This can be remedied by constructing biocompatible polymer brushes chemically derivatized with biotin [115, 116], or histidine-binding nitrilotriacetate (NTA)–metal ion complexes [43], to impart both antifouling and biorecognition properties at biointerfaces. These then allow for the binding of streptavidin-modified or His-tagged proteins, respectively. While successful, it should be noted that these chemical-based strategies impart a property of *extrinsic* biorecognition (i.e., indirect) because the proteins do not a priori recognize the polymers themselves. This imposes the limitation where only a predetermined set of tagged proteins can be targeted and not endogenous proteins sourced from authentic biological fluids. The latter aspect might be possible with proteins that are covalently immobilized on polymer brushes [117]; however no (extrinsic) biorecognition has yet been reported.

The objective of this work lies in exploiting the *intrinsic* protein–polymer biorecognition interactions between PEG-binding antibodies and PEG to sift out and sort specific molecular "cargoes" from a complex biological environment to site-specific targets. On the basis of its renowned properties of biocompatibility and protein resistance, PEG [118] is used extensively (i) in technology to impart fouling resistance against protein and cell adsorption on surfaces [119] and ultrafiltration membranes for water purification [10], as well as (ii) in biomedical applications [84] to reduce immunogenicity and increase resistance to proteolytic cleavage in drug targeting [84, 118]. Subsequently, PEG-binding antibodies have been developed for the identification and analysis of pharmacokinetic parameters of PEGylated

molecules in drug development and clinical applications [85, 120, 121]. Neverthe-
less, it should be noted that the use of PEG-binding antibodies in the current
context lies not in detecting PEGylated surfaces per se, but as biohybrid mo-
lecular adaptors or "receptors" that deliver and mediate the binding of specific
protein 'cargoes' to PEG. Further appeal rests in how intrinsic biorecognition in-
teractions may exert a biomimetic stimuli-induced conformational change in the
PEG. This so-called smart "protein-like" functionality is unique in comparison to
current stimuli-responsive polymers where conformational changes are triggered
by changes in solvent quality, pH, and temperature [122].

5.2 Results

To show how PEG-binding antibodies can be applied toward synthetic protein
targeting, we obtained a PEG-binding mouse IgG monoclonal antibody (i.e., E11
[85]; henceforth known as anti-PEG) that is known to recognize the repeat ethyl-
ene oxide (EO) subunits on the PEG backbone. An immunoblot assay shows
that anti-PEG binds with high specificity to the 20 kDa PEG chains (Fig. 5.1a;
Methods section 2.2.8). Its equilibrium dissociation constant was measured by
surface plasmon resonance (SPR) by flowing anti-PEG at different concentra-
tions over a PEG-functionalized SPR chip. The equilibrium dissociation con-
stant, K_D, was calculated by fitting the equilibrium SPR binding signal, R_{eq}, at
each respective concentration to the Langmuir adsorption isotherm [123], giving
$K_D = 0.40\,\text{nM} \pm 0.09\,\text{nM}$ (Figs. 5.1b and c).

Therefore, from a strict materials perspective, anti-PEG is remarkable in that it
provides an exclusive biochemical interface for binding to PEG. To be precise, this
is to our knowledge the first ever instance where a protein specifically recognizes
and binds a completely synthetic, unmodified polymer (i.e., the anti-PEG spe-
cifically recognizes the PEG backbone itself). Thereafter, we hypothesized that
the anti-PEG could act as a biohybrid molecular adaptor that selectively targets
specific secondary antibodies out of bulk solution and used (i) polyclonal donkey

anti-mouse secondary IgG as model cargo ("specific IgG") and (ii) polyclonal donkey anti-rabbit secondary IgG ("unspecific IgG"), which does not bind anti-PEG as a fouling control.
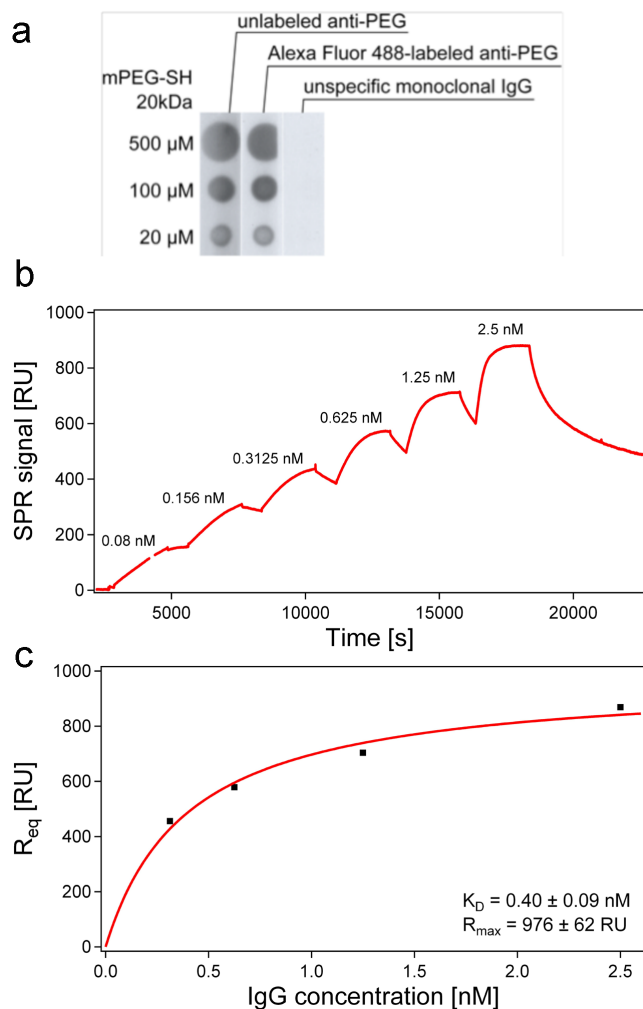
FIGURE 5.1: **(a)** Comparison of immunoblots with unlabelled and Alexa488-labelled anti-PEG. An unspecific mouse monoclonal IgG was used as negative control. **(b)** SPR sensogram for quantifying anti-PEG binding to 20 kDa PEG at increasing anti-PEG concentrations. **(c)** Calculation of the anti-PEG–PEG equilibrium dissociation constant, K_D, by a Langmuir adsorption isotherm fit to the equilibrium SPR binding signals, R_{eq}, obtained at different anti-PEG concentrations.

Spatially distinct PEG targets were constructed by tethering 20 kDa methoxy- and thiol-terminated polyethylene glycol (mPEG-SH) chains via covalent thiol bonds to Au nanorings ("PEGylated nanoring", Fig. 5.2; Methods section 2.2.2). The nanorings were fabricated 1.3 μm apart on glass slides in a 20×20 array format with each bare nanoring having a thickness and inner and outer diameter

of $27.1\,\text{nm} \pm 1.6\,\text{nm}$, $115\,\text{nm} \pm 8\,\text{nm}$ and $367\,\text{nm} \pm 6\,\text{nm}$, respectively. A combined atomic force microscope (AFM) and total internal reflection fluorescence (TIRF) microscope was used to correlate nanomechanical changes in the PEG chains to subsequent biochemical interactions via fluorescence, respectively (Fig. 5.2b). After PEGylation, the hydrated PEG chains form polymer brushes, which act as barriers over individual nanorings [20].
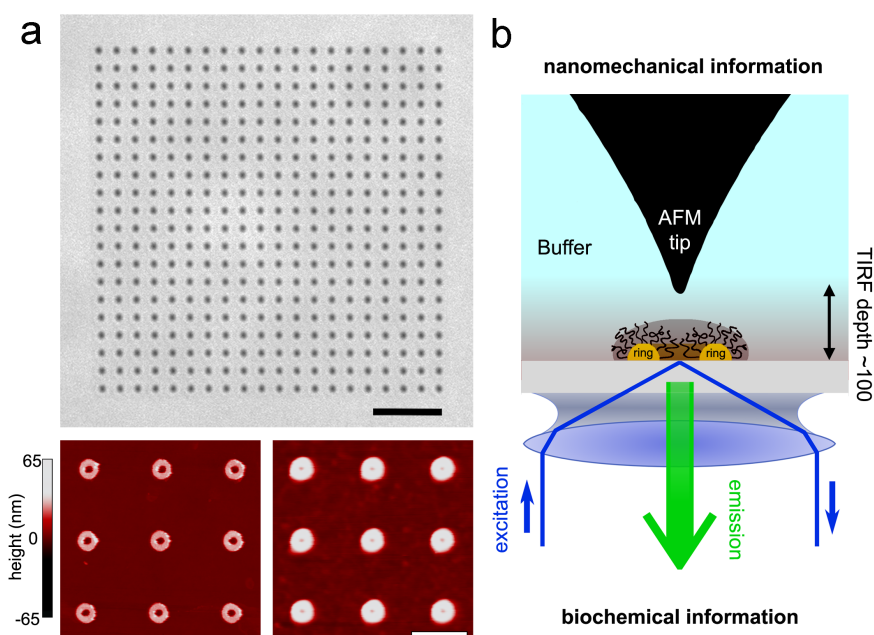
FIGURE 5.2: Combining nanofabrication, AFM, and TIRF. **(a)** Bright-field optical view of a 20×20 array of Au nanorings fabricated on a glass slide. Scale bar, $5\,\mu\text{m}$. Lower left: Individual nanorings resolved by AFM before PEGylation. Lower right: A polymer brush barrier forms over each nanoring after PEGylation. Scale bar, $1\,\mu\text{m}$. **(b)** Combining AFM and TIRF allows for the direct correlation of local nanomechanical effects in the PEG brush to antibody-associated biochemical interactions occurring at each nanoring.

Fig. 5.3 shows TIRF images obtained in a phosphate-buffered saline (PBS) solution simultaneously pre-incubated with Alexa488-labelled anti-PEG[1], Cy3-labelled specific IgG, Cy5-labelled unspecific IgG ($\sim 7\,\text{nM}$ per antibody), and $1\,\%$ ($150\,\mu\text{M}$) unlabelled bovine serum albumin (BSA). Strong fluorescent signals corresponding to anti-PEG and specific IgG are seen at the PEGylated nanorings (Fig. 5.3a–c). In comparison, inverted contrast is observed for unspecific IgG in epifluorescence

---

[1]An immunoblot was used to confirm that the labelling procedure did not impair the specificity of anti-PEG towards PEG (Fig. 5.1)

(i.e., the PEGylated nanorings are dark compared to the surrounding area), indicating a lack of localization despite being abundant in solution (Fig. 5.3d). We note that this is also observed for specific IgG in the absence of anti-PEG (see later, Fig. 5.8b). Time-lapse measurements recorded approximately equal accumulation rates of $1.6 \times 10^{-3}\,\text{s}^{-1}$ and $1.5 \times 10^{-3}\,\text{s}^{-1}$ for anti-PEG and specific IgG, respectively (Fig. 5.3e), indicating that specific IgG is being escorted with anti-PEG from solution. This is further supported by their mean fluorescence intensities and intensity distributions that are closely correlated over three consecutive targeting–washing cycles (Fig. 5.3f; see Methods, section 2.2.10). The observed decrease in the net fluorescence intensity per cycle, however, may be attributed to the harsh $500\,\text{mM}$ NaOH (pH 13.7) cleaning solution used to ensure complete removal of the antibodies during each washing step. This was later avoided by lowering the concentration and pH of the NaOH solution (see Fig. 5.7b).

AFM force volume (FV) spectroscopy [20] was used to monitor changes in the PEG brush height under the influence of the different antibodies (Fig. 5.4). In PBS, the PEG barrier height is $29.5\,\text{nm} \pm 4.8\,\text{nm}$ and $34.2\,\text{nm} \pm 11.2\,\text{nm}$ above the nanoring surface and the glass surface (at the nanoring center or "pore"), respectively. After adding the specific and unspecific IgG, the barrier height at these locations reduces to $24.4\,\text{nm} \pm 1.6\,\text{nm}$ and $29.5\,\text{nm} \pm 9.0\,\text{nm}$, respectively. This reduction in PEG height could arise from physical interactions (e.g., van der Waals force) occurring between the non-PEG-binding antibodies and the underlying gold surface that would exert a "compressive" effect on the intervening PEG brush [124]. Nevertheless, their lack of accumulation (as seen in TIRF; see Fig. 5.8) suggests that the PEG is still in a brush-like barrier state. When anti-PEG is bound to the PEG (as confirmed by TIRF), the height at the nanoring surface and the pore further reduces to $20.0\,\text{nm} \pm 2.8\,\text{nm}$ and $19.5\,\text{nm} \pm 5.1\,\text{nm}$, respectively. Closer inspection of force curves reveal further insights into the brush structure (Fig. 5.5).

We observe an exponential increase in force upon AFM tip approach above the PEGylated ring and pore, in contrast to the hard-wall repulsion measured over the glass surface. This indicates that the PEG forms a polymer brush over the entire nanoring [20]. After addition of specific and unspecific IgG at $\sim 10\,\text{nM}$
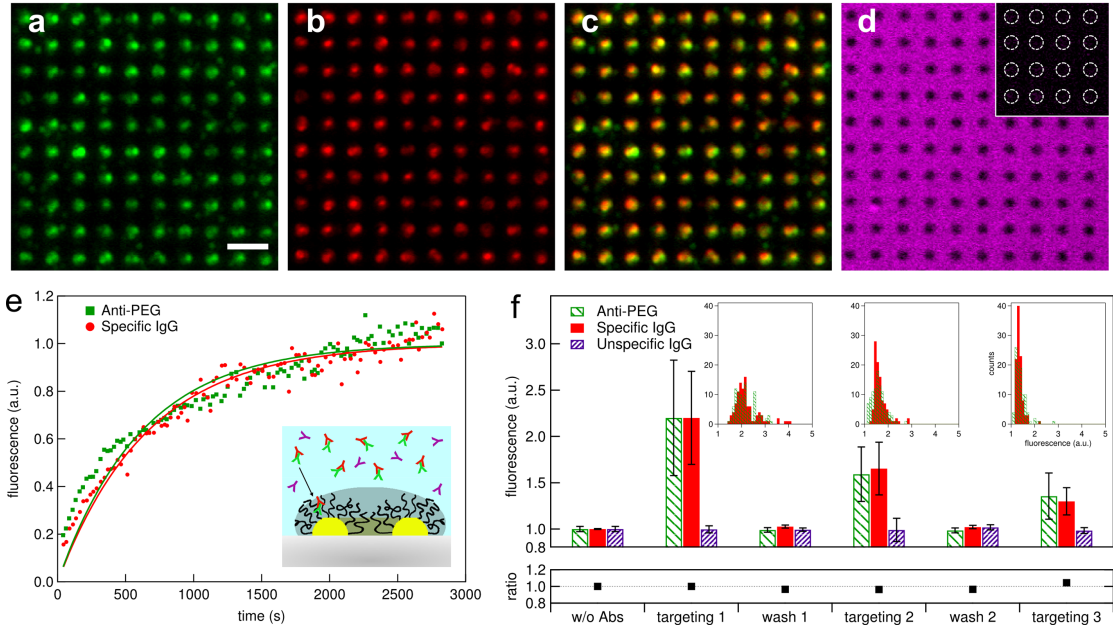
FIGURE 5.3: Precision targeting of specific IgG via anti-PEG. **(a)** TIRF reveals anti-PEG binding to each PEGylated nanoring. Scale bar, 2 µm. **(b)** The targeting of specific IgG from solution. **(c)** Merged co-localisation signal of anti-PEG and specific IgG. **(d)** The "inverted contrast" in epifluorescence shows that unspecific IgG is abundant in solution but does not accumulate at the PEGylated nanorings. This is confirmed by a lack of fluorescence in TIRF (inset; dashed circles indicate the positions of individual nanorings). **(e)** Time-lapse TIRF fluorescence intensity measurements for anti-PEG (green squares) and specific IgG (red circles), respectively. The solid lines are single exponential fits (Eq. 2.16) to the data. **(f)** Fluorescence quantification over consecutive targeting–wash cycles. By definition, the fluorescence intensity obtained in the absence of all three antibodies is set to unity. The mean nanoring intensities that remain at a constant 1 : 1 ratio (anti-PEG : specific IgG) indicate that targeting is reversible, as validated by the overlap in their intensity distributions (inset). Error bars denote the standard deviation of nanoring intensities on a single sample.

each, the repulsive force over the nanorings retains its exponential form, although with a slightly lower decay length, i.e. brush height. The change over glass can be explained by unspecific adsorption of the proteins (BSA and antibodies). In comparison, when adding ∼4 nM anti-PEG to the solution, dominant instabilities are present in the measured force curves over the ring and pore. Together with a clear reduction of the brush height (particularly at the pore), this indicates a disruption of the PEG barrier upon binding of anti-PEG, with the bound anti-bodies likely contributing to the instabilities. The less obvious reduction at the nanoring surface is most likely marred by the accumulation of antibodies there
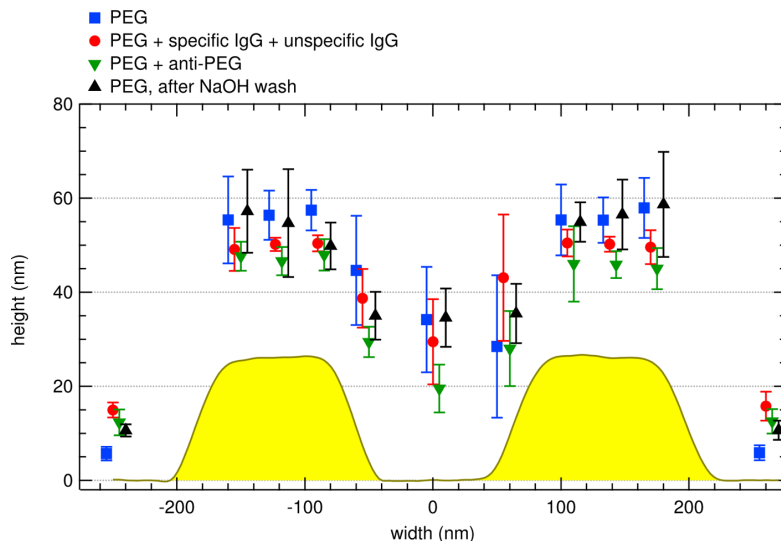
FIGURE 5.4: Correlating nonbinding/binding interactions to conformational changes in the PEG barrier. The average cross-section of a bare nanoring is shown in yellow. The PEG brush forms a barrier in PBS that envelops the nanoring surface and the central pore, respectively (blue squares). A slight reduction at both the nanoring and the pore is measured in the presence of specific and unspecific IgG (red circles). Anti-PEG binding elicits a strong reduction (green inverted triangles) that is more obvious at the pore because the PEG chains collapse to their tethering sites along the inner wall and not to the pore's basal glass surface. After removal of anti-PEG with NaOH, the brush height re-extends to its original brush height (black triangles). The outermost measurements (i.e., $< -200\,\text{nm}$ and $>200\,\text{nm}$) result from the adsorption of BSA and/or nonspecific molecules to the glass surface surrounding the nanorings. Force curves acquired at the outer nanoring edge have been omitted due to unstable tip contact. Error bars denote the standard deviation at each point.

(IgG has a hydrodynamic radius of $\sim5\,\text{nm}$) [125]. Subsequently, the PEG brush barrier recovers to a height of $29.6\,\text{nm} \pm 8.0\,\text{nm}$ (nanoring) and $34.6\,\text{nm} \pm 6.2\,\text{nm}$ (pore) after removing the anti-PEG using NaOH, and the force curves are restored to a similar form as before antibody incubation. This reversible "collapse" of the PEG chains might explain how the brush can maintain its antifouling property over several targeting–wash cycles.

Sequential binding experiments of first anti-PEG and then specific IgG show that anti-PEG alone binds to the PEGylated nanorings with an observed rate of $2.3 \times 10^{-3}\,\text{s}^{-1}$ (Fig. 5.6). After removal of unbound anti-PEG in solution, we find that specific IgG binds to the pre-bound anti-PEG with an observed rate of $2.4 \times 10^{-3}\,\text{s}^{-1}$. Interestingly, while specific IgG binds to the anti-PEG on the PEG targets, there is almost no co-localization between specific IgG and anti-PEG on
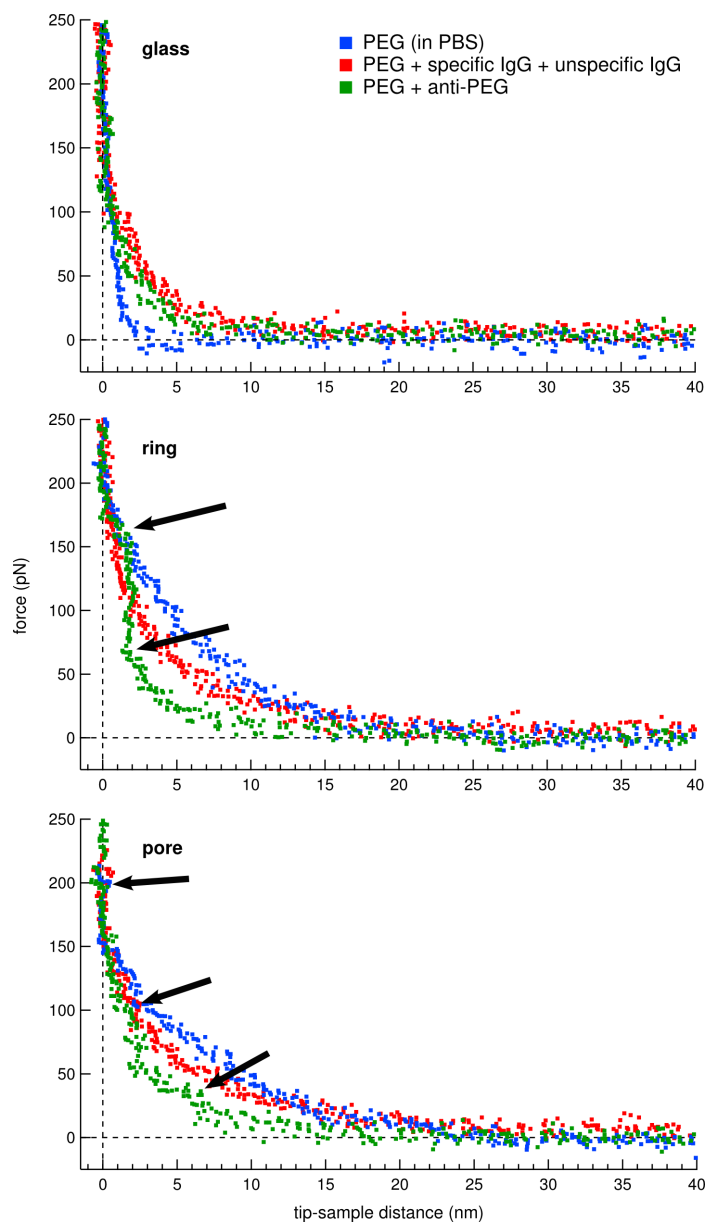
FIGURE 5.5: Representative force curves obtained upon approach of the AFM tip towards the sample at three distinct positions, i.e. over glass (top), over the nanoring surface (middle), and over the central pore (bottom). Blue: PEG brush in PBS before antibody binding; red: PEG brush with specific and unspecific IgG added; green: PEG brush with dominant instabilities (arrows) after anti-PEG addition.

the glass surface. This shows that the anti-PEG maintains its bioactivity when bound to PEG, but not on the glass surface.
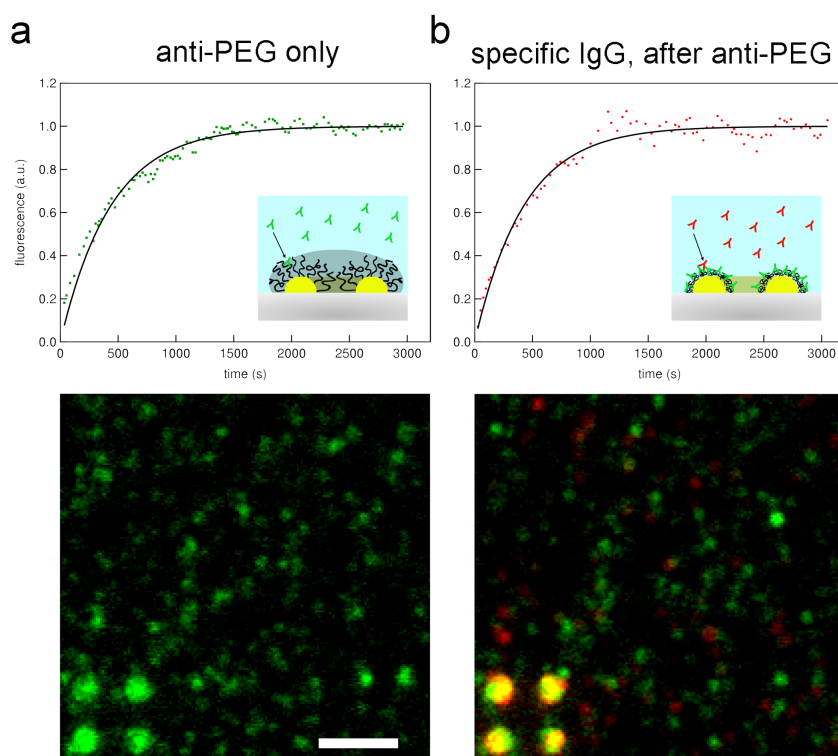
FIGURE 5.6: **(a)** TIRF measurements during incubation with only anti-PEG in solution. The upper panel shows time-lapse data (symbols) and a single exponential fit (Eq. 2.16) to the data (solid line). The lower panel shows specific binding of anti-PEG to PEGylated nanorings (4 rings, lower left corner) accompanied with random non-specific adsorption to the surrounding glass surface. Scale bar, 2 µm. **(b)** Sequential incubation of specific IgG (after removal of unbound anti-PEG in solution). Upper panel: time-lapse data (symbols) and single exponential fit (solid line). Lower panel: the specific IgG is now co-localized with the anti-PEG on the same PEGylated nanorings, but not on glass.

Finally, all three antibodies ($\sim$7 nM per antibody) were incubated in blood serum (containing $50 - 100$ mg/ml protein and $\sim$2 mg/ml lipids) to assess the effectiveness and reversibility of our synthetic protein targeting assay in an authentic, multicomponent biological fluid. As in PBS, the co-localization of specific IgG and anti-PEG is unmistakable (Fig. 5.7a), with their ratios (anti-PEG : specific IgG) remaining close to unity over two consecutive NaOH wash–antibody incubation cycles (Fig. 5.7b). Here, the 10 mM NaOH (pH 12) washing solution did not result in a decrease of the fluorescence intensity between cycles (compare with Fig. 5.3f).

Hence, PEG not only is antifouling against nonspecific entities within the serum but also maintains its viability to anti-PEG binding (and specific IgG targeting) over consecutive washes. This shows that specific IgG targeting by anti-PEG is robust, reproducible, and reversible.
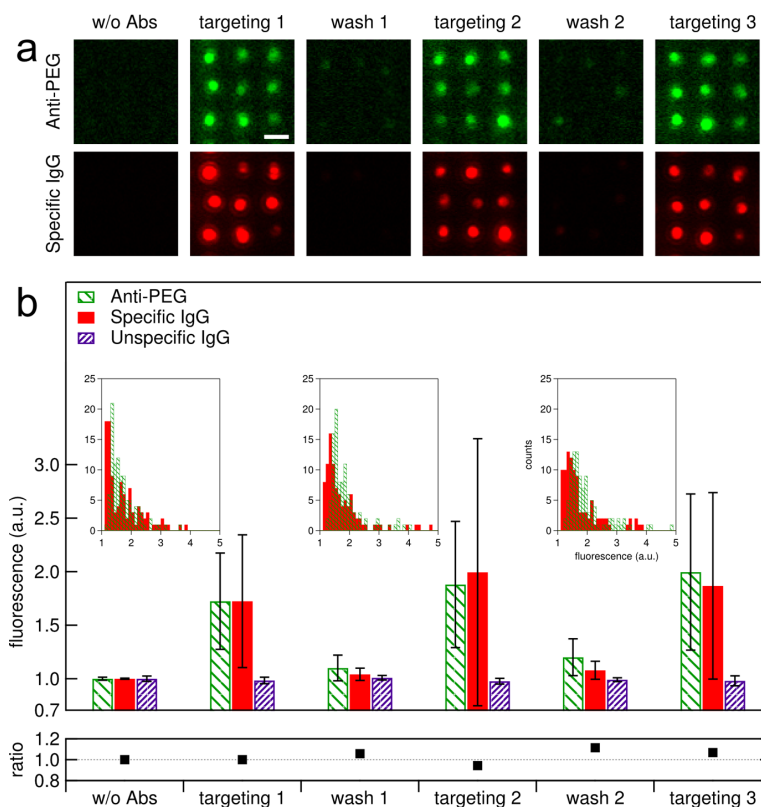
FIGURE 5.7: Reversible targeting in blood serum. **(a)** TIRF images obtained over three consecutive targeting–wash cycles. Targeting is reversible after $10\,\mathrm{mM}$ NaOH washing steps, although the number of anti-PEG and specific IgG molecules (= intensity) can differ between PEGylated nanorings. Scale bar, $1\,\mu\mathrm{m}$. **(b)** Fluorescence quantification at the PEGylated nanorings. By definition, the fluorescence intensity obtained in the absence of all three antibodies is set to unity. The overall intensities of specific IgG and anti-PEG are reproducible over two targeting–wash cycles with an approximate $1:1$ distribution ratio (inset). Accumulation of the unspecific IgG does not occur at the PEGylated nanorings. The error bars denote the ring intensity standard deviations within one sample.

5.3   Discussion

On the basis of these results, the use of the PEG–anti-PEG system may be able to resolve several issues related to interfacial protein stability. First, PEG targets do not denature in complex biological environments (except oxidation by

alcohol dehydrogenase) [126]. Second, the mode of specific IgG capture by anti-PEG in solution before PEG targeting precludes binding artefacts and potential loss of bioactivity that result from the surface immobilization of capture proteins/antibodies (e.g., from denaturing and molecular orientation effects) [111, 114]. Third, precision targeting from a complex milieu (i.e., serum) is achieved without sample prepurification given the antifouling characteristics of PEG. Likewise, no washing steps or dilutions are required for targeting. Fourth, given its inability to denature, PEG targets can be reversibly washed and targeted unlike surface-bound protein targets. Fifth, PEG preserves and maintains antibody bioactivity on surfaces [127]. By incubating the antibodies sequentially, we find that specific IgG binds to anti-PEG prebound to the PEGylated nanorings but not to anti-PEG nonspecifically adsorbed on the glass (Fig. 5.6). Therefore, this method of preloading PEG with anti-PEG may be even applied in ELISA-based assays [111]. Sixth, the relative ease at which PEG functionalization can be carried out enhances the prospect of nanoscale miniaturization in biodiagnostics (i.e., a protein microarray spot size is typically $\sim 200\,\mu\text{m}$, whereas our targets are sub-micrometre in size) [128]. Altogether, these attributes satisfy six out of the eleven performance benchmarks listed by Wu et al. concerning the future development of assay capture surfaces in complex biological milieus [111].

The biochemical selectivity and spatial targeting precision we observe is governed by applying a concept that accounts for molecular sorting, selective targeting, and surface fouling as closely interconnected effects. As we illustrate in Fig. 5.8, this requires (1) a nanoscale target exhibiting antifouling properties in complex media (e.g., PEG brush); (2) a molecular adaptor with exclusive access to the intended target (e.g., anti-PEG); and (3) a suite of specific cargoes that do not themselves bind to the target but instead "hitchhike" along with the molecular adaptor (e.g., specific IgG). Based on these hierarchical principles, its implementation is not likely limited to PEG-based systems alone. Nevertheless, PEG-based applications can benefit from expanding the repertoire of target cargoes by engineering bispecific antibodies [129] (or other antibody variants) [130] that would

similarly act as biohybrid molecular adaptors that bind to PEG and another epitope (e.g., a disease biomarker). This adds a biochemical versatility that may be advantageous over the use of chemically derivatized biorecognition polymers [43] given the fact that untagged endogenous proteins can be sourced directly from authentic biological fluids. In combination with nonfouling PEGylated surfaces, such biohybrid adaptors could have potential applications spanning from nanopatterning to biosensing technologies and for regulating molecular transport processes more generally.

Technological implications aside, we observe that anti-PEG binding leads to a reduction in the repulsive Z-range of the PEG brush barrier that correlates to a conformational compaction. This might stem from a loss of conformational entropy in the PEG that is further exacerbated by the presence of several anti-PEGs that bind in a bivalent manner either intermolecularly between PEG chains or intramolecularly along a single chain. While theoretical efforts are starting to yield insight into the underlying physics of such behaviour [131], the relevance of this biomimetic effect, where intrinsic biorecognition and binding can induce conformational changes in an entirely synthetic polymer, resides in how it is analogous to the folding of intrinsically disordered (also called natively unfolded) proteins [132] upon binding to a ligand. This so-called "protein-like" functionality is unique in comparison to current stimuli-responsive polymers, where conformational changes are triggered by changes in solvent quality, pH, and temperature [122]. From a structural viewpoint, resolving exactly how anti-PEG binds to the PEG backbone may provide further insight into the molecular basis of fouling resistance in PEG [11].

5.4 Conclusions

The essence of our work in this chapter lies in being able to connect a biological material system to an abiological one by intrinsic biorecognition. Specifically, anti-PEG acts as a biohybrid molecular adaptor that can be used to sift specific
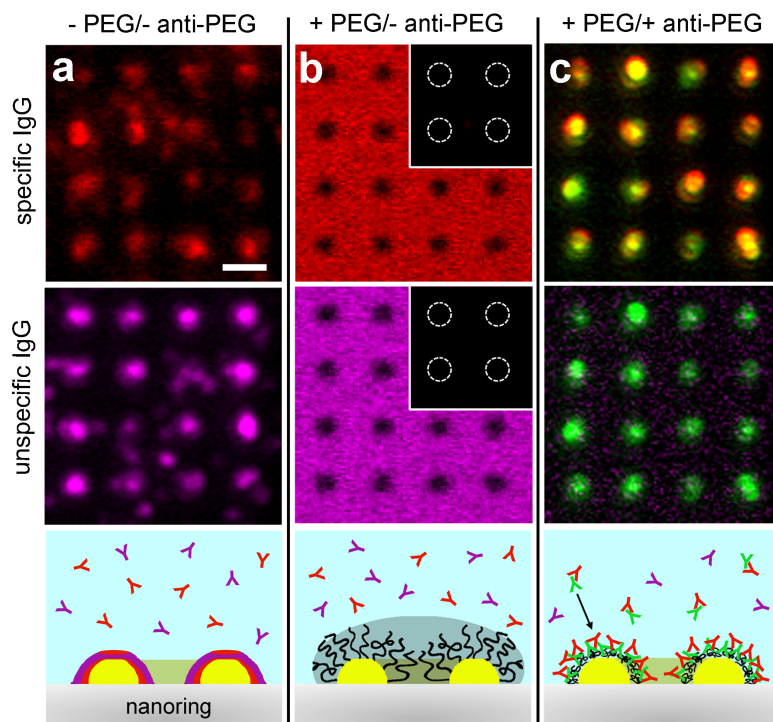
FIGURE 5.8: Molecular sorting, selective targeting, and surface fouling are interconnected effects. **(a)** Fouling: in the absence of PEG and anti-PEG, TIRF images show that "red", specific IgG (top) and "magenta", unspecific IgG (center) bind nonspecifically to (i.e. foul) the bare nanorings. (Bottom) Red **Y** and magenta **Y** symbols correspond to specific IgG and unspecific IgG in solution, respectively. Fouling is denoted by the red and magenta bands over the nanoring. Scale bar, 1 µm. **(b)** Antifouling: in the absence of anti-PEG, the PEGylated nanorings remain dark in epifluorescence, although specific IgG (top) and unspecific IgG (center) are abundant in solution. The lack of fouling at the nanorings (TIRF, inset) indicates that both antibodies are being repelled by the PEG brush barrier (bottom). **(c)** Precision targeting: in the presence of "green" anti-PEG, specific IgG is distinctly co-localized with anti-PEG at the PEGylated nanorings (top). In contrast, unspecific IgG does not co-localize (center). By binding specifically to anti-PEG, specific IgG is precisely targeted to the PEGylated nanorings via exclusive anti-PEG binding interactions with the PEG (bottom). This is accompanied by a conformational compaction or "collapse" of the PEG brush.

proteins out of complex biological fluids for immobilization onto PEGylated targets. In part, this is inspired by how biological "adaptors" (known as transport receptors or karyopherins) identify and target specific proteins (deemed for transport into the nucleus) from the cytoplasm to nuclear pore complexes in eukaryotic cells [133]. In fact, the central pore of the nuclear pore complex is comprised of several intrinsically disordered proteins, which have been implicated in regulating the transport of selective cargo by reversibly collapsing during binding with karyopherins [134]. Thus, it may be possible to harness the binding-induced collapse of PEG to function as a selective gating mechanism in stimuli-responsive nanoporous membranes [135] (as opposed to changing solvent conditions) [20].

Chapter 6

Conclusions and Outlook

6.1 Conclusions

In this thesis we have thoroughly characterized the covalent grafting of poly(ethylene glycol) (PEG) to Au surfaces from solution. We have shown how the size of the polymer and especially the grafting conditions can greatly influence the grafting density of PEG chains on the surface. Cloud point grafting by using Na_2SO_4 in the grafting solution extends the possible grafting densities towards the very dense regime. By varying the PEG and Na_2SO_4 concentrations we have explored a parameter space where the final grafting densities can be tuned from mushroom regime to dense brushes. We further applied a recently developed surface plasmon resonance (SPR) technique [86] using non-interacting macromolecules (the protein BSA) to directly measure the height of PEG brushes on a flat Au surface, and find that our results are in accordance to polymer theory predictions [8] and to other measurements [47]. We especially note that by controlling the grafting density, we can tune the polymer brush height in a wide range.

We have presented a unique, truly three-dimensional nanoscale experimental system in the form of Au nanorings. Our nanorings have distinct nanostructural geometric domains, such as a nanopore-like environment at the centre of the rings. Conventional nanopatterning methods use a two-dimensional flat surface as the

grafting surface to create patterns in the lateral directions [136]. In comparison, here we have a grafting surface that is modulated in all 3 dimensions. This is crucial for modelling a nanopore-like environment. The Au nanorings were PEG-functionalized (PEGylated) at the same conditions as we used for SPR to enable direct comparison between the two systems. We have used atomic force microscopy (AFM) as a tool for probing interactions and forces of polymers at the nanorings at spatial resolutions of a few nm and at forces down to 20 pN.

Using AFM to measure the morphology and dynamics of the Au nanoring system, we first confirm that changing the grafting conditions leads to similar trends in the final surface density and brush height changes as seen by SPR. By employing different analysis methods, we conclude that most likely surface densities do not change by as much upon change in grafting conditions as on the flat SPR Au chip. Unfortunately, a direct measurement method of surface densities or adsorbed mass on the nanostructures is lacking at present.

Nanopore polymer functionalization is of great interest for creating filtering and sensing systems with single-molecule sensitivity and control. It is thus of importance to understand the morphology and dynamic behaviour of polymer chains grafted at nanopores. So far mainly theoretical considerations are available, and experimental probing of polymer-functionalized nanopore systems is difficult to conduct. Our Au nanorings with easy handling and access to nanomechanical and optical probing by AFM and fluorescence microscopy, yet having a real nanopore-like geometry, are ideally suited to address polymer dynamics at nanopores, as well as the sorting and targeting of biological molecules to nanoscale PEG targets.

By dynamically compressing the PEG brushes on the nanorings and varying the AFM loading rate over two orders of magnitude, we show that the loading rate influences the response of the brush to the compressing tip. In particular we have shown that the local nanoring geometry influences the brush properties such as height and stiffness. At the nanoring central hole we see a distinctly different response to compression at various loading rates than over the ring Au substrate. This we attribute to different modes of mechanical interaction in these two regions.

At the flat surface, elastic compression of the polymer brush takes place, while over the nanopore-like central region additional modes such as shearing could occur.

Finally, we have explored and shown how nanoscale PEGylated targets can be used as a synthetic targeting system for biological macromolecules. By employing an antibody-based model system we show a way how the anti-fouling and biocompatibility properties of PEG can be harnessed to selectively and specifically target cargoes even from complex biological fluids towards synthetic nanoscale structures. Further, we show that PEG brushes can change their morphology upon the stimulus of specific biochemical binding interactions. In the context of protein-functionalized nanopores, this "smart" stimuli-responsive behaviour could show a way towards specific and robust filtering and transport systems.

6.2 Outlook

Based on our experiments with nanorings and nanoholes, we see that polymers (here: PEG) of appropriate length can create a steric barrier across a nanopore or -channel. By tuning the polymer size, a barrier against desired particle sizes can be created, leading a way towards a nanofiltering system based on size exclusion. Further, as we have shown in chapter 5, (bio-)molecules can be introduced that interact specifically with the PEG barrier, allowing targeting of cargoes to the barrier and even locally disrupting the PEG barrier by biochemical binding interactions, leading possibly to exclusive access of our PEG-binding molecules to the pore interior. Taken together, this could be harnessed to create nanopores or membranes with possibly single molecule control and sensitivity, and at the same time specificity towards certain molecules or particles. An obvious follow-up to our proof-of-concept of these effects on nanorings grafted to a solid substrate is to create real nanopores or nanoporous membranes that connect two reservoirs, and correlate transport or flux measurements with our AFM and fluorescence data.

Towards this end we have fabricated suspended SiN membranes with arrays of solid-state nanopores, with dimensions comparable to our current nanoring system

(Fig. 6.1). Having a similar Au ring grafting substrate around the nanopores, there is an opportunity to use the grafting parameters investigated in this thesis to rationally design nanopores with PEG barriers of desired properties. The nanopore behaviour could be assessed both by AFM and by transport measurements between reservoirs, and so similarities and possible differences elucidated between nanorings on a substrate and free-standing nanopores.
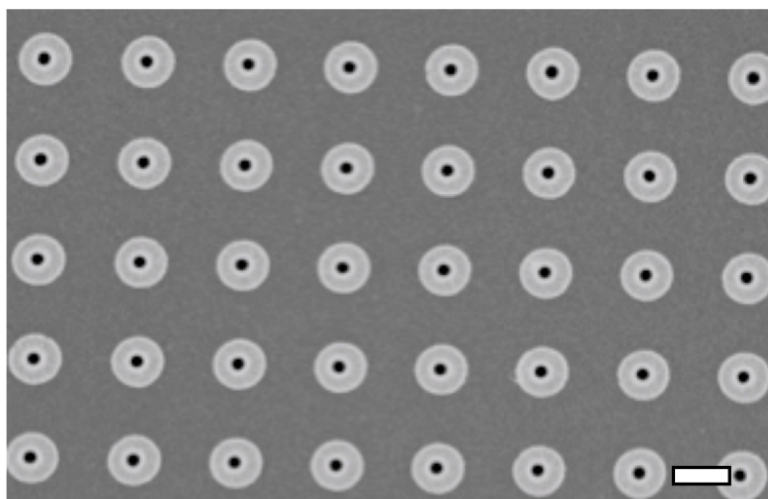
FIGURE 6.1: Scanning electron micrograph of suspended nanopore array. The nanopores with pore length of ~ 100 nm and width ~ 100 nm, surrounded by Au ring structures. Scale bar, 500 nm.

PEG barriers exclusively accessed by specific molecules could also be used to create nanohole arrays as plasmonic sensors [97] with restricted molecular access to the sensing volume. If only desired molecules can pass to the detection volume, specificity could be greatly enhanced even in non-ideal sensing situations (e.g. from "dirty" or complex fluids).

Regarding dynamic effects of polymer brush compression by an AFM tip, we have seen interesting effects depending on the local geometry, both in the collective response to confinement (i.e. brush height and stiffness changes), as well as in single events such as a polymer escape-like transition. Here our system has not been thoroughly described theoretically, so providing a clear picture of polymer brush mechanics remains difficult at the moment. For example, simulations of tip-like structures shearing a brush in nanopores, or of an AFM tip compressing a brush at various speeds would be welcomed (in comparison to large obstacles or

uniform shear velocity fields, as has been done). Experimentally, fully exploring the effect of relative tip and pore or ring sizes could enhance our understanding of the effects measured in this thesis.

Appendix A

Force Curves

This appendix contains typical raw force vs tip-sample distance curves.

Fig. A.1 and Fig. A.2 show example force curves taken over Au nanorings functionalized at low density and high density PEG brush conditions, respectively. PEG grafted at lower density leads to a lower brush height on the nanorings. This can be seen in the example force curves, where at low density conditions the repulsive interaction between tip and brush starts closer to surface. Fig. A.3 shows typical force curves taken over the Au surface of nanohole samples. $20\,kDa$ PEG exhibits a significantly larger brush height than $10\,kDa$ PEG. Force curves over unfunctionalized (bare) samples don't show any brush behaviour. Attractive interactions between the AFM tip and the bare surface cause a jump into contact when the tip is close to the surface. Fig. A.4 shows example force curves exhibiting an escape transition-like jump in the force while compressing a $20\,kDa$ PEG brush on Au nanorings.
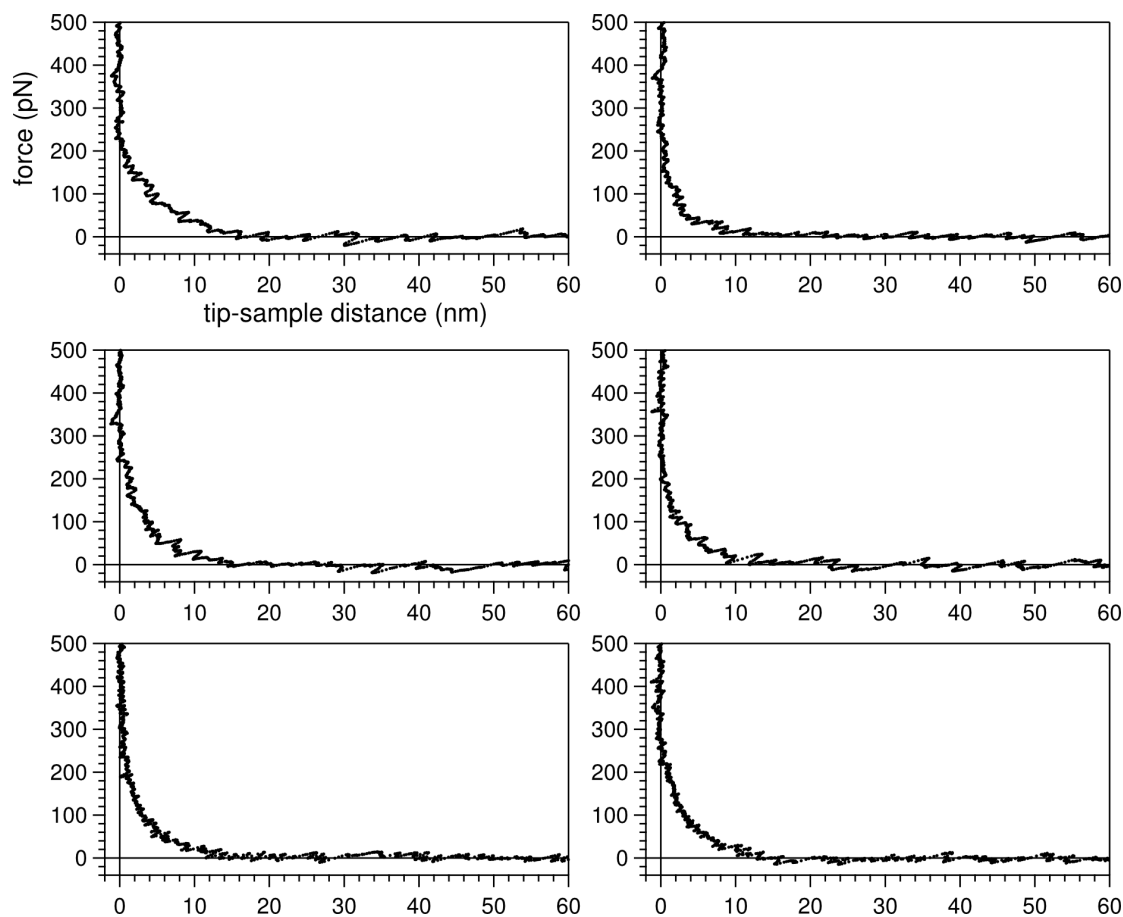
FIGURE A.1: Typical force curves recorded over Au nanorings functionalized with 20 kDa PEG at low brush density conditions (grafting solution 40 mg/ml PEG in PBS; $g_{\mathrm{SPR}} = 4.1$ nm). Average brush height is 16.2 nm. Note the onset of repulsion at lower distances (i.e. smaller brush height) compared to high density conditions (Fig. A.2).
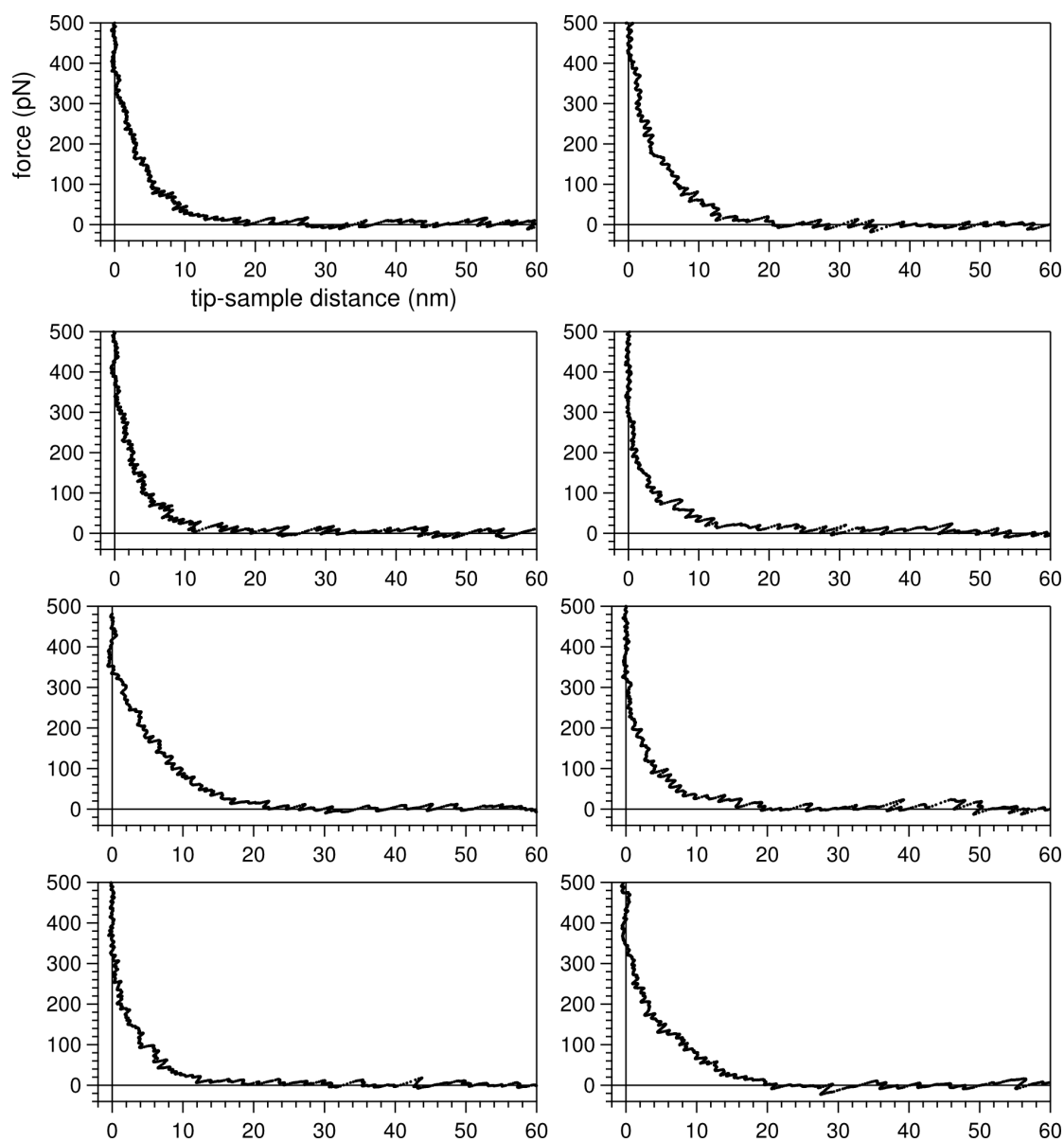
FIGURE A.2: Typical force curves recorded over Au nanorings functionalized with 20 kDa PEG at high brush density conditions (grafting solution 0.13 mg/ml PEG in 0.9 M Na_2SO_4 in PBS; $g_{SPR} = 2.2$ nm). Average brush height is 19.5 nm.
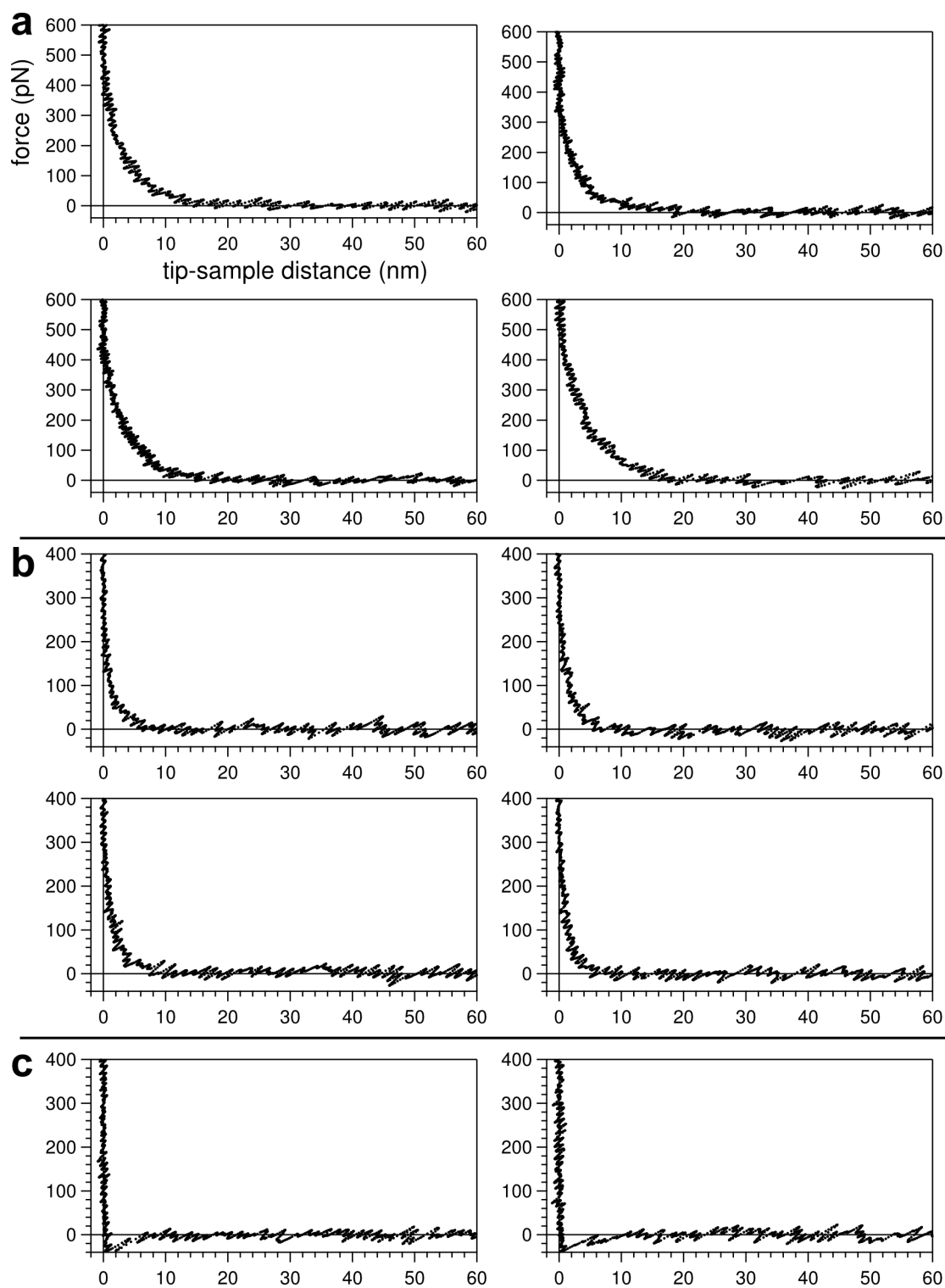
FIGURE A.3: Typical force curves over Au nanohole samples. **(a)** Sample functionalized with 20 kDa PEG. Average brush height 18.1 nm. **(b)** 10 kDa PEG, average brush height 6.4 nm. **(c)** Bare Au surface with jump into contact due to attractive interactions between tip and surface.
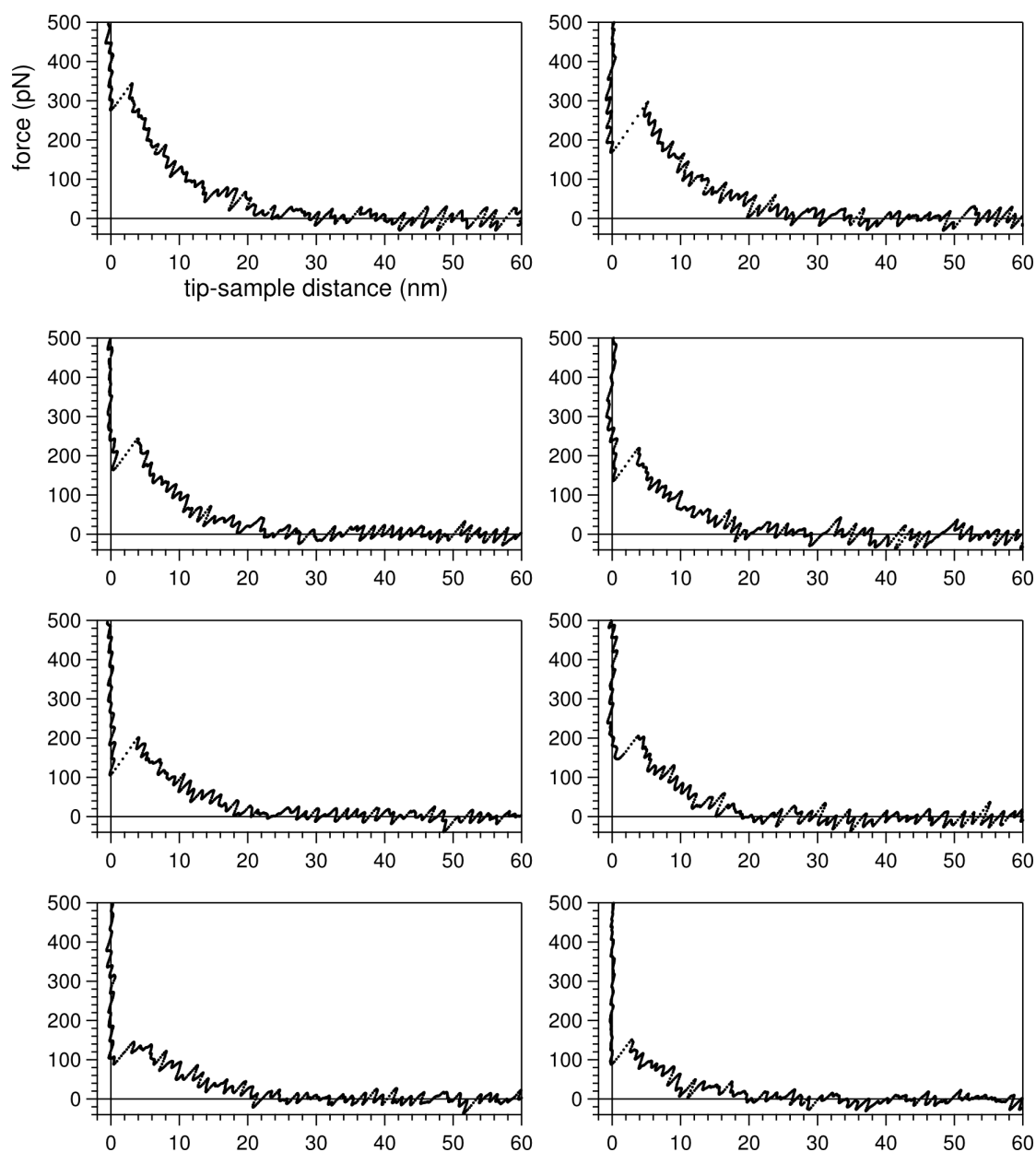
FIGURE A.4: Typical force curves exhibiting a sudden escape transition-like jump in force during compression of a 20 kDa PEG brush on an Au nanoring. Force curves with transitions at different forces and distances have been selected.

Appendix B

Data Analysis Software

This appendix describes the custom-written data analysis software used in this thesis. Section B.1 briefly describes ImageJ macros used for the fluorescence intensity analysis in chapter 5. Section B.2 serves as the user manual for the custom IGOR software used for most AFM data analysis in this thesis. All code is available under a free license.

B.1 ImageJ image analysis macros

A set of ImageJ [92] macros was used to assist with the fluorescence intensity measurements in this thesis. The macros can be downloaded at `https://github.com/jhyot/imagej-helper-macros`. These macros can be imported and run via the usual ImageJ macro commands (refer to the ImageJ manual for a description of how to run macros).

copy-timings-to-clipboard.ijm

This macro analyses any optical microscopy time series file and copies the acquisition times of each frame to the clipboard. After starting the macro, select the time series file you wish to analyse, and then select which series and channels you'd like

to include in the output. After the macro finishes, the timings are copied into the clipboard in a tab-separated format (a column for each selected channel), so that it can be easily pasted e.g. into a spread sheet.

The Bio-Formats [137] plugin for ImageJ[1] must be installed for the macro to work.

measure-ring-intensities.ijm

This macro measures the fluorescence intensity over the nanorings in a nanoring array such as seen in Fig. 3.6. The macro can handle a single image or a stack of images. Upon running the macro a dialog window will ask for various parameters. The grid angle and position of the top-left ring can optionally be determined in a visual way: Draw exactly one line ROI horizontally across a row of rings (determines the angle), and one point ROI in the center of the top-left ring (determines the x and y starting coordinates).

Parameters can also be read in from a file. The parameter file can be chosen in the next window appearing after closing the parameter dialog. In the parameter file, parameters must be defined one per line in the format `parameterName=value`. For a list of all parameters look at the header of a result file after running the analysis once. Missing or invalid parameter values will be replaced by a default value.

Fluorescence intensities can be adjusted for background by two different methods (the third option is no background adjustment).

median min

> The median min method runs a median filter over the image to reduce noise outliers and takes the minimum intensity value around each ring as the background for that ring. This background value is subtracted from the ring intensity to arrive at the background-corrected ring intensity.

---

[1] `http://www.openmicroscopy.org/site/products/bio-formats`

avg normalized

>   The avg normalized method takes the average intensity (no filtering applied) within a background ring region (bounded by an inner and outer radius as defined in the analysis parameters), and normalizes the nanoring intensity by this background average for each ring.

roi-multi-measure.ijm

This is a small helper macro to quickly measure all ROIs for all slices in all open images. The user can define ROIs for a single image, and then automatically have the ROIs measured in all slices and images. For this to work, the ROIs must not be named in a slice-specific way, i.e. the `sss-yyyy-xxxx` format is not allowed. The macro writes the pixel area, average intensity, standard deviation, and integrated intensity into a single file.

B.2   AFM analysis software

The custom AFM analysis software package consists of IGOR Pro procedure files (WaveMetrics, USA)[2]. It has been tested with IGOR version 6.3.4 under Windows 7. The analysis software can be downloaded at `https://github.com/jhyot/afm-forcecurve-analysis`.

The software offers a basic user interface for loading force curves and force volume maps from Bruker (formerly Veeco) Nanoscope files, analysing the brush height of each force curve, and reviewing and classifying curves. Further, additional functionality is available by calling specific functions manually (from the command window, a macro or a procedure). The software has been tested with data obtained by Nanoscope versions 7.3 and 8.1x.

---

[2]`http://www.wavemetrics.com/`

This manual is divided into three parts. Section B.2.1 describes the installation, start and configuration of the software. Section B.2.2 describes the features accessible through the graphical user interface (GUI), and section B.2.3 finally describes the additional functions not available through the GUI. Basic familiarity of IGOR Pro operation is assumed, and knowledge about functions and procedures is necessary for using the functions not provided through the GUI.

B.2.1 Installation and configuration

Installation

Download the software package and place all included files and folders into any folder. No additional installation is necessary. In the root folder, `forcecurve-analysis.ipf` is the main program file. The `config` folder contains configuration files which can be edited by the user. The `lib` folder contains most of the software code, and does not need to be modified by the user.

Loading the software

To load the software package, start Igor by opening the `forcecurve-analysis.ipf` file (e.g. double-click on the file), or load the file within Igor from the menu `File` `Open File` `Procedure...`. Compile the script by selecting `Macros` `Compile` from the menu, or `Compile` in the procedure window. On successful compilation, all the other files are loaded automatically and a new top-level menu entry `Force Map Analysis` will appear (Fig. B.1).

Configuration

Some basic parameters for data loading and analysis are configured by editing the file `config/fca-config.ipf` which is available once the code has been loaded (see above). Access the file by selecting `Windows` `Procedure Windows` `fca-config.ipf`.
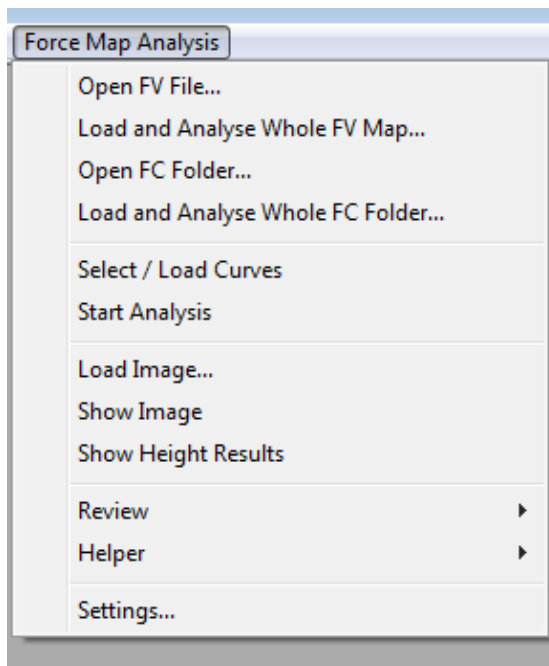
FIGURE B.1: Menu for accessing the GUI functions of the AFM analysis software.

Enable editing by clicking on the pencil symbol in the lower left corner. This file contains parameters which each control a particular aspect of the software. Change a parameter by editing the part following the assignment symbol $\boxed{=}$. Parameters have been set to sensible values by default, but depending on the data, changing the values can be necessary for correct results.

The following parameters influence the loading of Nanoscope data files.

ksVersionReq

> Lists all valid file versions that can be read by this software (separated by commas). Any files recorded by differing Nanoscope software versions will not be loaded and produce an error to protect from unnoticed wrong loading or analysis. Usually the file format does not change between Nanoscope versions, so additional versions can be added here (see the header of the Nanoscope data file for the version string), but careful inspection of the results should be performed when first loading data from a new version.

ksFixPointNum

> Defines how the number of data points per force curve is determined.

0: Automatically read the number of points from the force curve data file.

1: Fix the number of points to the value given in the next parameter (this setting is mainly left for legacy reasons).

ksFCPoints

Number of points per force curve. This parameter only has an effect if **ksFixPointNum** is set to **1**.

ksFVRowSize

Number of pixels per row in a force volume map. Since maps are quadratic, this also defines the number of rows. Only the values **16** and **32** have been thoroughly tested.

ksFileTypeFV

The string by which force volume files are identified (the header of the files is searched for this string). There should be no reason to change this parameter, unless the Nanoscope file format has changed.

ksFileTypeFC

The string by which single force curve files are identified (the header of the files is searched for this string). There should be no reason to change this parameter, unless the Nanoscope file format has changed.

ksHeaderEnd

The string which defines the end of the header in data files. There should be no reason to change this parameter, unless the Nanoscope file format has changed.

The following parameters influence aspects of data analysis.

ksBaselineFitLength

Value between 0 and 1. Sets the fraction of the whole force curve length that is used for baseline fitting. Too small values lead to inaccurate fits if the force curve has some irregularities. Too large values also lead to wrong

fits if the baseline is not perfectly linear (as can be the case for very long ramp sizes).

ksBrushCutoff

Used only if the brush height calculation is based on the exponential fit algorithm. Defines the brush height as the distance at which the exponential fit crosses this force value (in pN). **Note:** In the current version of the software there is no straightforward way to switch to the exponential fit brush height calculation.

ksBrushOverNoise

Used only if the brush height calculation is based on the noise threshold algorithm. Defines the brush height as the distance at which the smoothed force curve crosses the smoothed baseline noise multiplied by this factor. Smaller values give larger (more realistic) brush heights but lead to higher susceptibility to noise. Values <1 are not useful.

ksDeflSens_ContactLen

Approximate length of the piezo ramp during which there is contact between tip and sample (in nm). This doesn't have to be accurate but provides guidelines for the fitting algorithm. The default value should work for most force curves. If the deflection sensitivity fit leads to wrong values, changing this parameter can improve results.

ksDeflSens_EdgeFraction

Defines how much of the hard-wall portion of a curve is getting fitted for deflection sensitivity. The default value should work for most force curves. If the deflection sensitivity fit leads to wrong values, changing this parameter can improve results. Useful values are in the range of $0.01 - 0.1$.

ksFixDefl

Defines how the deflection sensitivity is determined for each curve. **0:** The deflection sensitivity is fitted separately for each curve. **1:** Read the sensitivity from the header of the force curve or force volume file.

ksXDataZSens

> Defines whether available Z sensor (height sensor) data is used instead of the fixed ideal ramp size set when recording force curves. Using Z sensor gives more correct data. For this, one ramp channel has to be set to Z sensor (sometimes denoted Height sensor) during recording. **0:** Don't use Z sensor data. **1:** Use Z sensor data if it is available. **2:** Always use Z sensor data (aborts data analysis if it is not available).

ksMaxGoodPt

> Some force data may have corrupted data at the end of the curves. If such cases are not detected automatically, this parameter can be set to the point number after which the rest of the force curve is ignored. Set to **-1** to ignore this parameter.

B.2.2   GUI features

This section describes the features available through the Force Map Analysis menu (Fig. B.1).

Before loading and working with a force volume file or a force curve file set, you should create and switch to a new data folder in Igor. Working directly in the root data folder is not recommended. To create a new data folder, select Data ⟩ ⟩ Data Browser from the top menu, followed by New Folder... in the data browser window. Enter a unique name and select Set As Current Data Folder. Each force curve data set should go into its own data folder. Nested folders are allowed.

Loading and analysing data

Loading and analysing a force volume file

Select Force Map Analysis ⟩ Open FV File.... In the settings dialog, choose whether to load any friction data and Z sensor data present in the FV dataset. Only select yes if your dataset includes this data. These settings are saved per data folder. If

you want to change them later, choose ⟨Settings...⟩ from the menu. Next, select the file to load. The quasi-topography map appears after successful loading of the FV file.

Choose ⟨Select / Load curves⟩ from the menu to select which force curves from the map to import into Igor and to analyse. Select individual force curves by clicking on the corresponding pixel in the map, or ⟨All⟩ to select all curves.

Next, select ⟨Start Analysis⟩ from the menu to perform the brush height and related analysis of the previously loaded force curves. After the analysis is finished, an image representing the brush heights is displayed. Any errors during this step can be related to inappropriate configuration values (see Section B.2.1) or trying to load data which is not present (such as Z sensor data).

The menu command ⟨Load and Analyse Whole FV Map...⟩ serves as a shortcut to automatically open a FV file and load and analyse all force curves.

Navigating through the data

After successful loading and analysis of the FV data, you can view any force curve by clicking on the corresponding pixel in the quasi-topography or brush height maps. A new graph is shown each time a pixel is selected. To navigate through the data without opening a new graph, hold ⟨Ctrl⟩ while in the force curve graph and use the arrow keys to navigate around the map.
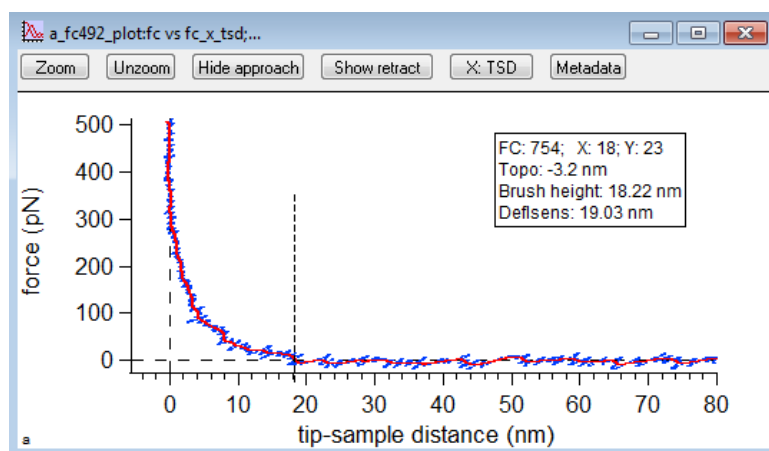

FIGURE B.2: Force curve graph.

In the force curve graph (Fig. B.2), you have several buttons to control the data presentation. All regular Igor formatting methods and options are available as well. The $\boxed{\text{Zoom}}$ and $\boxed{\text{Unzoom}}$ buttons cycle through predefined zoom levels. The zoom levels can be re-defined through editing of the source code (see Section B.2.3). The $\boxed{\text{Approach}}$ and $\boxed{\text{Retract}}$ buttons show or hide the approach and retract parts of the force curves, respectively. The button starting with $\boxed{\text{X:}}$ switches between display modes and displays the current mode. $\boxed{\text{X: TSD}}$ is showing the force vs tip-sample-distance curve, while $\boxed{\text{X: Zpiezo}}$ is showing the force vs Z piezo position curve. $\boxed{\text{Metadata}}$ prints metadata for the displayed curve gathered during loading and analysing to the command window.

The graphs can be closed at any time, but any changes to the presentation of the graph will be lost.

Images

The menu command $\boxed{\text{Load Image...}}$ allows to select and load a different image as the quasi-topography map. This is useful when you want to process the topography map in a different software (e.g. flattening) and then import it back to Igor. $\boxed{\text{Show Image}}$ and $\boxed{\text{Show Height Results}}$ bring the quasi-height image and the brush height map to the front, respectively, if they have been hidden after the initial loading. Note that closing the images (instead of just hiding them) cannot be undone.

Loading and analysing a collection of individual force curves

In addition to a force volume file, this software can also load and analyse individual force curves. Use the menu items $\boxed{\text{Open FC Folder...}}$, $\boxed{\text{Select / Load Curves}}$ and $\boxed{\text{Start Analysis}}$ (or the shortcut $\boxed{\text{Load and Analyse Whole FC Folder...}}$) to import all force curves located in a given folder. All files in the folder which are recognized as force curves will be analysed. The curve files are imported in the order of their filenames.

After selecting the source folder, you can choose between three different types:

line Indicates that the individual force curves were taken in a straight line over the surface (e.g. using the point-and-shoot mode of Nanoscope). The cross-section force curve analysis graph will open after the analysis step (Fig. B.3).

box Indicates that the force curves were taken in a quadratic pattern similar to the force volume mode. When selecting this option, the data set behaves as though it was loaded from a force volume file.

random

Indicates that the force curves have neither a linear nor box-like relation to each other. After analysis, the cross-section force curve analysis graph will open for ease of analysing and displaying the data. But although the curves are shown to be in one line, this is only for display purposes.

Cross-section analysis

The cross-section force curve analysis window (Fig. B.3) will open after analysis of line or random type force curve data. This window is divided in three parts. The top part shows the hard-wall topography (black line) and brush height (red area) for each force curve. The middle part shows the force (i.e. vertical deflection) data, and the bottom part shows the friction data (horizontal deflection).

The vertical and horizontal deflection graphs show both approach and retract curves. The dashed vertical line indicates the calculated brush contact point. The buttons above the graph allow to choose between tip-sample-distance and piezo position modes, and to switch between predefined zoom levels. The zoom levels can be re-defined through editing of the source code (see Section B.2.3). By holding the Shift key and moving the mouse over the force curves, a vertical guide appears. Moving the cross-hair in the top panel (either by dragging it or with left/right arrow keys) selects the corresponding force curve data set. All graphs can be customized by using the standard Igor features.
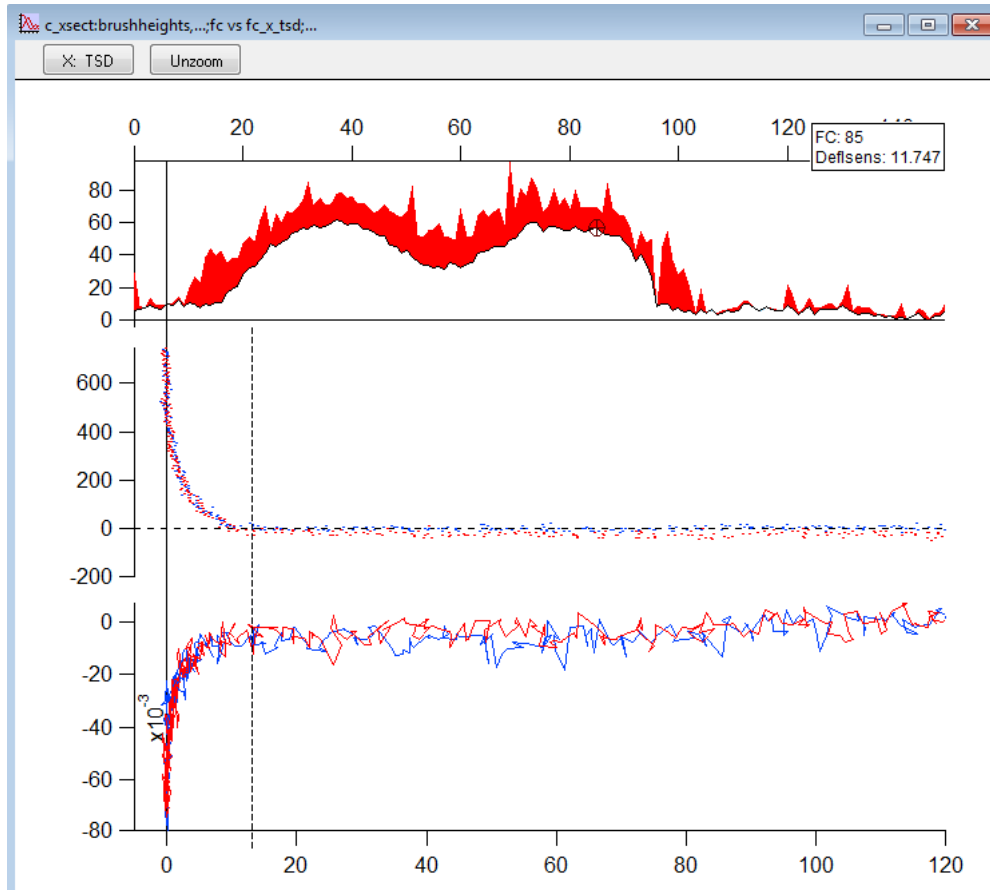
FIGURE B.3: Cross-section force curve analysis window.

Reviewing data

Once data has been loaded and analysed by the software, several data review functions are available through the Review submenu.

Flagging curves

The function Review ⟩ Flag Curves... allows to flag force curves based on parametrizable criteria. The different criteria allow to find force curves with general bad quality or incorrect fits. Once the Flag Curves algorithm has been run, Review ⟩ Mark Flagged shows the flagged curves as red markers in the topography and brush height images (only for FV data).

The `flaggedcurves` wave stores the value 1 at the index of every flagged curve, and can be used for custom analysis or processing of flagged curves.

Reviewing curves

Selecting Review ⟩ Review All Curves or Review ⟩ Review Flagged Curves starts the review mode. Each curve in turn can be accepted or rejected as a valid data point. When using Review Flagged Curves, the non-flagged curves are automatically accepted as valid. The Zoom and Unzoom buttons cycle through the predefined zoom levels (customizable through editing of the source code, see Section B.2.3). The default zoom level for the next curve can be selected in the drop-down list. The Redo last button returns to the previous curve. The Stop button stops the review.

Brush heights from accepted and rejected curves are stored in the `heights_acc` and `heights_rej` waves, respectively. The data can be used to perform calculations and statistical analysis based on the particular subset of data. If a review is stopped before reviewing all curves, the brush heights from the remaining curves will not be added to either of the new waves.

Classifying curves

The Review ⟩ Classify Curves function is a specialized reviewing tool that was used to analyse the data for Chapter 4.5. In its current form it can only be used to classify force curves taken over a ring-like structure. A force curve can be classified as "exhibiting a certain feature", or "not exhibiting the feature" (or excluded from classification, e.g. when the data quality is too bad). After the classification step, a histogram is computed that shows the frequency of the classified feature as a function of the distance from the center of the ring (with and without normalizing for the number of curves at a given distance). Pixels which have low enough quasi-topography height (i.e. which lie outside the ring structure) are automatically excluded from classification.

Helper Functions

The Helper menu provides access to some utility functions.

Brush Histogram

Calculates and displays a histogram of brush heights over the whole dataset. The display will not show outliers with very large brush height values, because those are usually measurement or analysis errors.

Subtract Baseline

Subtracts a baseline (linear fit) from the designated wave. If the active window has a "A" cursor placed on a trace, then that wave is used, otherwise a dialog will ask for the wave name. You can exclude regions from participating in the baseline fit by placing them between pairs of cursors (i.e. between A and B, C and D, etc.). The original wave will be backed up as `backups/<wavename>_baselinesubtr`.

Median Filter Image

Applies a median filter with a 3×3 pixel kernel to a given image, and also filters out any `NaN` pixels. You will be asked for the image wave name to be filtered. The original wave will be backed up as `backups/<wavename>_medianfilt`.

B.2.3   Additional functions

Some functionality is not accessible via the Force Map Analysis menu but only by directly calling specific functions, e.g. in the Command Window or from custom scripts. The following sections briefly describe the additional useful functions, grouped by functionality. The full explanation of the input and output parameters, and implementation details can be obtained by reading the source code.

Brush height analysis

Most functions in the file `lib/fca-analysis.ipf` perform the brush height calculation and related analysis, and are accessible through the menu. Additionally some functions can be called manually for further analysis. It is recommended

to call the additional analysis functions only after performing a regular analysis through the menu, to ensure that all necessary setup is done and waves have been created.

CalcLinStiffness

Calculates the linear brush stiffness for the currently loaded data, as used in section 4.3 and described in the Methods in section 2.2.6. The resulting data will be saved in the `linstiffness` wave.

CalcHertzEModAll

Calculates the brush Young's modulus for the currently loaded data. The algorithm is described in section 4.3. Uses the `twohertz` curve fitting function from `lib/fca-fitting.ipf`. Note that some coefficients for the fit are hardcoded in the `CalcHertzEMod` function. The calculated E_1 and E_2 Young's moduli are saved in the `emod1` and `emod2` waves.

Functions residing in the file `lib/fca-absolute-relative-heights.ipf` are used to produce the "brush contact height" analysis and corresponding plots in section 3.6.

absrelheights

Creates the wave that holds the "brush contact height" data (i.e. image height plus brush height). It's called "absolute" height in the functions, as opposed to "relative" height, which is the brush height above the hard-wall contact point. Parameters `img` and `bheights` are existing image and brush height wave names, while the other parameters are names of waves that will be created by the function (absolute brush height wave and the two different "zero" lines).

scatterplots

Creates the scatterplots used in section 3.6. Parameters are as above, with `img`, `bheights` and `added` names of existing waves, while the other two will be created.

plot_color, plot_color_auto

> Creates the coloured areas on the scatterplot (or any other plot). `plot_color` takes the color boundary positions as parameters, while `plot_color_auto` chooses the boundaries automatically based on the first X wave data in the plot.

absrelheights_combine

> Concatenates multiple input waves into a single output wave and displays a scatterplot of the combined data.

Loading rate analysis

The code in `lib/fca-loadingrate-analysis.ipf` was used to analyse the data and create the graphs for section 4.2. Unfortunately, the code is extremely specialised for the particular task and no effort has been spent to make it more general and user-friendly. The interested reader is welcome to look through the code and associated comments.

Helper Functions

Helper functions assist with miscellaneous small tasks. The functions are located in `lib/fca-datainfo.ipf` and `lib/fca-wave-handling.ipf`.

PrintInfo, PrintInfoDF

> Prints information about the current data folder or one passed as parameter.

PrintParams

> Prints analysis and curve parameters. The desired parameters must be passed into the function. The function searches global analysis parameters and per-curve parameters and prints out any matches. The second input argument selects the curve number for which to print the parameters. To see what parameters are available, have a look at the `internalvars/analysisparameters` variable and at the `fcmeta` text wave.

SaveBackupWave, RestoreBackupWave

Saves and restores a given wave to/from the `backups` data folder.

MakeTempCurve

Extracts a single curve from the full curve dataset. This can be used to try out analysis and operations on a given wave. It is intended to be used with the `fc` and `rfc` group of 2D waves. The index to be extracted can be passed in by hand or it can be read from an open graph displaying the desired curve.

Curve Fitting

The curve fitting functions in `lib/fca-fitting.ipf` can be used from a script or from the Igor Analysis ≫ Curve Fitting... dialog. The mathematical formulas can be found in the code comments within the individual functions. Most functions are transformed to work with nm and pN units, since the loaded and analysed force curves are saved in these units.

Zoom settings

Although all graphs can use standard Igor zooming and scaling functions, many force curve graphs include special zoom buttons for convenient setting of standard zoom levels. The zoom levels can be configured in the `config/fca-zoom-config.ipf` file. The configuration is done by editing a matrix with zoom values. Each field in the matrix corresponds to a curve type, zoom level, and axis. The source file has additional comments to help with finding the correct field for changing a specific zoom setting.

Bibliography

[1] C. Dekker. 'Solid-state nanopores.' In: *Nature Nanotechnology* 2 (2007), pp. 209–215.

[2] S. Howorka and Z. Siwy. 'Nanopore analytics: sensing of single molecules.' In: *Chemical Society Reviews* 38 (2009), pp. 2360–2384.

[3] W. Sparreboom, A. van den Berg and J. C. T. Eijkel. 'Principles and applications of nanofluidic transport.' In: *Nature Nanotechnology* 4.11 (2009), pp. 713–20.

[4] B. N. Miles, A. P. Ivanov, K. a. Wilson, F. Dogan, D. Japrung and J. B. Edel. 'Single molecule sensing with solid-state nanopores: novel materials, methods, and applications.' In: *Chemical Society Reviews* 42.1 (2013), pp. 15–28.

[5] O. Azzaroni and K. H. A. Lau. 'Layer-by-Layer Assemblies in Nanoporous Templates: Nano-Organized Design and Applications of Soft Nanotechnology.' In: *Soft Matter* 7.19 (2011), pp. 8709–8724.

[6] P. G. de Gennes. 'Conformations of Polymers Attached to an Interface'. In: *Macromolecules* 13.5 (1980), pp. 1069–1075.

[7] S. T. Milner. 'Polymer Brushes.' In: *Science* 251.4996 (1991), pp. 905–914.

[8] P. G. de Gennes. 'Polymers at an interface; a simplified view'. In: *Advances in Colloid and Interface Science* 27.3-4 (1987), pp. 189–209.

[9] B. Zhao and W. J. Brittain. 'Polymer brushes: surface-immobilized macromolecules'. In: *Progress in Polymer Science* 25.5 (2000), pp. 677–710.

[10] A. Asatekin, S. Kang, M. Elimelech and A. M. Mayes. 'Anti-fouling ultrafiltration membranes containing polyacrylonitrile-graft-poly(ethylene oxide) comb copolymer additives'. In: *Journal of Membrane Science* 298 (2007), pp. 136–146.

[11] M. Morra. 'On the molecular basis of fouling resistance.' In: *Journal of Biomaterials Science. Polymer Edition* 11.6 (2000), pp. 547–69.

[12] L.-P. Zhu, H.-B. Dong, X.-Z. Wei, Z. Yi, B.-K. Zhu and Y.-Y. Xu. 'Tethering hydrophilic polymer brushes onto PPESK membranes via surface-initiated atom transfer radical polymerization'. In: *Journal of Membrane Science* 320.1-2 (2008), pp. 407–415.

[13] J.-Q. Meng, T. Yuan, C. J. Kurth, Q. Shi and Y.-F. Zhang. 'Synthesis of antifouling nanoporous membranes having tunable nanopores via click chemistry'. In: *Journal of Membrane Science* 401-402 (2012), pp. 109–117.

[14] S. Minko. 'Responsive Polymer Brushes'. In: *Journal of Macromolecular Science, Part C: Polymer Reviews* 46.4 (2006), pp. 397–420.

[15] M. A. Cohen Stuart et al. 'Emerging applications of stimuli-responsive polymer materials.' In: *Nature Materials* 9.2 (2010), pp. 101–13.

[16] M. Tagliazucchi and I. Szleifer. 'Stimuli-responsive polymers grafted to nanopores and other nano-curved surfaces: structure, chemical equilibrium and transport'. In: *Soft Matter* 8.28 (2012), p. 7292.

[17] O. Azzaroni. 'Polymer brushes here, there, and everywhere: Recent advances in their practical applications and emerging opportunities in multiple research fields'. In: *Journal of Polymer Science Part A: Polymer Chemistry* 50.16 (2012), pp. 3225–3258.

[18] J. Tetenbaum-Novatt and M. P. Rout. 'The mechanism of nucleocytoplasmic transport through the nuclear pore complex.' In: *Cold Spring Harbor Symposia on Quantitative Biology* 75 (2010), pp. 567–584.

[19] O. Peleg and R. Y. H. Lim. 'Converging on the function of intrinsically disordered nucleoporins in the nuclear pore complex.' In: *Biological Chemistry* 391.7 (2010), pp. 719–30.

[20] R. Y. H. Lim and J. Deng. 'Interaction forces and reversible collapse of a polymer brush-gated nanopore.' In: *ACS Nano* 3.10 (2009), pp. 2911–8.

[21] J. T. Hyotyla, J. Deng and R. Y. H. Lim. 'Synthetic protein targeting by the intrinsic biorecognition functionality of poly(ethylene glycol) using PEG antibodies as biohybrid molecular adaptors.' In: *ACS Nano* 5.6 (2011), pp. 5180–7.

[22] G. W. de Groot, M. G. Santonicola, K. Sugihara, T. Zambelli, E. Reimhult, J. Vörös and G. J. Vancso. 'Switching Transport through Nanopores with pH-Responsive Polymer Brushes for Controlled Ion Permeability.' In: *ACS Applied Materials & Interfaces* 5.4 (2013), pp. 1400–7.

[23] S. P. Adiga and D. W. Brenner. 'Flow control through polymer-grafted smart nanofluidic channels: molecular dynamics simulations.' In: *Nano Letters* 5.12 (2005), pp. 2509–14.

[24] J. Huang, Y. Wang and M. Laradji. 'Flow Control by Smart Nanofluidic Channels: A Dissipative Particle Dynamics Simulation'. In: *Macromolecules* 39.16 (2006), pp. 5546–5554.

[25] O. Peleg, M. Tagliazucchi, M. Kröger, Y. Rabin and I. Szleifer. 'Morphology control of hairy nanopores.' In: *ACS Nano* 5.6 (2011), pp. 4737–47.

[26] S. J. O'Shea, M. E. Welland and T. Rayment. 'An atomic force microscope study of grafted polymers on mica'. In: *Langmuir* 9.7 (1993), pp. 1826–1835.

[27] R. Ivkov, P. D. Butler, S. K. Satija and L. J. Fetters. 'Effect of Solvent Flow on a Polymer Brush: A Neutron Reflectivity Study of the Brush Height and Chain Density Profile'. In: *Langmuir* 17.10 (2001), pp. 2999–3005.

[28] S. C. McLean, H. Lioe, L. Meagher, V. S. J. Craig and M. L. Gee. 'Atomic force microscopy study of the interaction between adsorbed poly(ethylene oxide) layers: effects of surface modification and approach velocity.' In: *Langmuir* 21.6 (2005), pp. 2199–208.

[29] M. Heuberger, T. Drobek and N. D. Spencer. 'Interaction forces and morphology of a protein-resistant poly(ethylene glycol) layer.' In: *Biophysical Journal* 88.1 (2005), pp. 495–504.

[30] M. Gelbert, A. Roters, M. Schimmel, J. Rühe and D. Johannsmann. 'Viscoelastic spectra of soft polymer interfaces obtained by noise analysis of AFM cantilevers'. In: *Surface and Interface Analysis* 27.5-6 (1999), pp. 572–577.

[31] A. M. Jonas, Z. Hu, K. Glinel and W. T. S. Huck. 'Effect of nanoconfinement on the collapse transition of responsive polymer brushes.' In: *Nano Letters* 8.11 (2008), pp. 3819–24.

[32] G. Dunér, E. Thormann, A. Dedinaite, P. M. Claesson, K. Matyjaszewski and R. D. Tilton. 'Nanomechanical mapping of a high curvature polymer brush grafted from a rigid nanoparticle'. In: *Soft Matter* 8.32 (2012), p. 8312.

[33] J. Klein, D. Perahia and S. Warburg. 'Forces between polymer-bearing surfaces undergoing shear'. In: *Nature* 352.6331 (1991), pp. 143–145.

[34] E. Eiser and J. Klein. 'The Effect of Mobile Polymers on the Normal and Shear Forces between Polymer Brushes'. In: *Macromolecules* 40.23 (2007), pp. 8455–8463.

[35] J. Harden and M. Cates. 'Deformation of grafted polymer layers in strong shear flows'. In: *Physical Review E* 53.4 (1996), pp. 3782–3787.

[36] C. M. Wijmans and B. Smit. 'Simulating Tethered Polymer Layers in Shear Flow with the Dissipative Particle Dynamics Technique'. In: *Macromolecules* 35.18 (2002), pp. 7138–7148.

[37] S. M. Baker, G. S. Smith, D. L. Anastassopoulos, C. Toprakcioglu, A. A. Vradis and D. G. Bucknall. 'Structure of Polymer Brushes under Shear Flow in a Good Solvent'. In: *Macromolecules* 33.4 (2000), pp. 1120–1122.

[38]   G. Binnig, C. Quate and C. Gerber. 'Atomic force microscope.' In: *Physical Review Letters* 56.9 (1986), pp. 930–933.

[39]   S. S. Sheiko and M. Möller. 'Visualization of macromolecules–a first step to manipulation and controlled response.' In: *Chemical Reviews* 101.12 (2001), pp. 4099–124.

[40]   L. Gross, F. Mohn, N. Moll, P. Liljeroth and G. Meyer. 'The chemical structure of a molecule resolved by atomic force microscopy.' In: *Science* 325.5944 (2009), pp. 1110–4.

[41]   H.-J. Butt, B. Cappella and M. Kappl. 'Force measurements with the atomic force microscope: Technique, interpretation and applications'. In: *Surface Science Reports* 59.1-6 (2005), pp. 1–152.

[42]   M. Rubinstein and R. H. Colby. *Polymer Physics.* Oxford University Press, 2003, p. 456.

[43]   R. Barbey, L. Lavanant, D. Paripovic, N. Schüwer, C. Sugnaux, S. Tugulu and H.-A. Klok. 'Polymer brushes via surface-initiated controlled radical polymerization: synthesis, characterization, properties, and applications.' In: *Chemical Reviews* 109.11 (2009), pp. 5437–527.

[44]   D. L. Elbert and J. A. Hubbell. 'Surface Treatments of Polymers for Biocompatibility'. In: *Annual Review of Materials Science* 26.1 (1996), pp. 365–294.

[45]   S. Granick et al. 'Macromolecules at surfaces: Research challenges and opportunities from tribology to biology'. In: *Journal of Polymer Science Part B: Polymer Physics* 41.22 (2003), pp. 2755–2793.

[46]   R. A. L. Jones and R. W. Richards. *Polymers at Surfaces and Interfaces.* Cambridge University Press, 1999.

[47]   L. C. H. Moh, M. D. Losego and P. V. Braun. 'Solvent quality effects on scaling behavior of poly(methyl methacrylate) brushes in the moderate- and high-density regimes.' In: *Langmuir* 27.7 (2011), pp. 3698–702.

[48]   S. Milner, T. Witten and M. Cates. 'Theory of the grafted polymer brush'. In: *Macromolecules* 21.8 (1988), pp. 2610–2619.

[49]   H. J. Taunton, C. Toprakcioglu, L. J. Fetters and J. Klein. 'Forces between surfaces bearing terminally anchored polymer chains in good solvents'. In: *Nature* 332.6166 (1988), pp. 712–714.

[50]   F. Li and F. Pincet. 'Confinement free energy of surfaces bearing end-grafted polymers in the mushroom regime and local measurement of the polymer density.' In: *Langmuir* 23.25 (2007), pp. 12541–8.

[51]   J. N. Israelachvili. *Intermolecular and Surface Forces.* 3rd ed. Academic Press, 2011.

[52] B. Derjaguin. 'Untersuchungen über die Reibung und Adhäsion, IV'. In: *Kolloid-Zeitschrift* 69.2 (1934), pp. 155–164.

[53] H. J. Taunton, C. Toprakcioglu, L. J. Fetters and J. Klein. 'Interactions between surfaces bearing end-adsorbed chains in a good solvent'. In: *Macromolecules* 23.2 (1990), pp. 571–580.

[54] G. Subramanian, D. R. M. Williams and P. A. Pincus. 'Escape Transitions and Force Laws for Compressed Polymer Mushrooms'. In: *Europhysics Letters* 29.4 (1995), pp. 285–290.

[55] D. R. Williams and F. C. MacKintosh. 'Polymer Mushrooms Compressed Under Curved Surfaces'. In: *Journal de Physique II* 5.9 (1995), pp. 1407–1417.

[56] G. Subramanian, D. R. M. Williams and P. A. Pincus. 'Interaction between Finite-Sized Particles and End Grafted Polymers'. In: *Macromolecules* 29.11 (1996), pp. 4045–4050.

[57] J. Ennis, E. Sevick and D. Williams. 'Compression of a polymer chain by a small obstacle: The effect of fluctuations on the escape transition'. In: *Physical Review E* 60.6 (1999), pp. 6906–6918.

[58] A. Milchev, V. Yamakov and K. Binder. 'Escape transition of a polymer chain: Phenomenological theory and Monte Carlo simulations'. In: *Physical Chemistry Chemical Physics* 1 (1999), pp. 2083–2091.

[59] A. Milchev, V. Yamakov and K. Binder. 'Escape transition of a compressed polymer mushroom under good solvent conditions'. In: *Europhysics Letters* 47.6 (1999), pp. 675–680.

[60] D. Dimitrov, L. Klushin, A. Skvortsov, A. Milchev and K. Binder. 'The escape transition of a polymer: A unique case of non-equivalence between statistical ensembles'. In: *The European Physical Journal E* 29.1 (2009), pp. 9–25.

[61] E. M. Sevick and D. R. M. Williams. 'A Polymer End-Tethered to a Potential Stripe: A Simple Example of an Escape Transition'. In: *Macromolecules* 32.20 (1999), pp. 6841–6846.

[62] A. M. Skvortsov, L. I. Klushin and F. A. M. Leermakers. 'Exactly solved polymer models with conformational escape transitions of a coil-to-flower type'. In: *Europhysics Letters* 58.2 (2002), pp. 292–298.

[63] L. Klushin, A. Skvortsov and F. Leermakers. 'Partition function, metastability, and kinetics of the escape transition for an ideal chain'. In: *Physical Review E* 69.6 (2004), p. 061101.

[64] J. Ennis and E. M. Sevick. 'Compression and Escape of Copolymers of Adsorbing and Nonadsorbing Blocks'. In: *Macromolecules* 34.6 (2001), pp. 1908–1916.

[65] E. M. Sevick. 'Compression and Escape of a Star Polymer'. In: *Macromolecules* 33.15 (2000), pp. 5743–5746.

[66] J. Paturej, A. Milchev, S. A. Egorov and K. Binder. 'The Escape Transition of a Compressed Star Polymer: Self-Consistent Field Predictions Tested by Simulation'. In: *Macromolecules* 46.19 (2013), pp. 8009–8016.

[67] M. C. Guffond, D. R. M. Williams and E. M. Sevick. 'End-Tethered Polymer Chains under AFM Tips: Compression and Escape in Theta Solvents'. In: *Langmuir* 13.21 (1997), pp. 5691–5696.

[68] J. Jimenez and R. Rajagopalan. 'Interaction between a Grafted Polymer Chain and an AFM Tip: Scaling Laws, Forces, and Evidence of Conformational Transition'. In: *Langmuir* 14.10 (1998), pp. 2598–2601.

[69] F. A. M. Leermakers and A. A. Gorbunov. 'Polymer-Surface Interactions in Bridging Escape and Localization Transitions'. In: *Macromolecules* 35.22 (2002), pp. 8640–8649.

[70] M. Murat and G. S. Grest. 'Molecular Dynamics Simulations of the Force between a Polymer Brush and an AFM Tip'. In: *Macromolecules* 29.25 (1996), pp. 8282–8284.

[71] J. Jimenez and R. Rajagopalan. 'A new simulation method for the determination of forces in polymer/colloid systems'. In: *The European Physical Journal B* 5.2 (1998), pp. 237–243.

[72] J. Abbou, A. Anne and C. Demaille. 'Accessing the dynamics of end-grafted flexible polymer chains by atomic force-electrochemical microscopy. Theoretical modeling of the approach curves by the elastic bounded diffusion model and Monte Carlo simulations. Evidence for compression-induced late'. In: *The Journal of Physical Chemistry. B* 110.45 (2006), pp. 22664–75.

[73] N. A. Alcantar, E. S. Aydil and J. N. Israelachvili. 'Polyethylene glycol-coated biocompatible surfaces.' In: *Journal of Biomedical Materials Research* 51.3 (2000), pp. 343–51.

[74] D. Leckband, S. R. Sheth and A. Halperin. 'Grafted poly(ethylene oxide) brushes as nonfouling surface coatings.' In: *Journal of Biomaterials Science. Polymer Edition* 10.10 (1999), pp. 1125–47.

[75] J. Israelachvili. 'The different faces of poly(ethylene glycol).' In: *Proceedings of the National Academy of Sciences of the United States of America* 94.16 (1997), pp. 8378–9.

[76] H. Matsuura and K. Fukuhara. 'Conformational analysis of poly(oxyethylene) chain in aqueous solution as a hydrophilic moiety of nonionic surfactants'. In: *Journal of Molecular Structure* 126 (1985), pp. 251–260.

[77] M. Jannelli, S. Magazu', G. Maisano, D. Majolino and P. Migliardo. 'Non-ideal compressibility in poly(ethylene oxide)-water solutions induced by H-bond interactions'. In: *Journal of Molecular Structure* 322 (1994), pp. 337–343.

[78] H. Ju, B. D. McCloskey, A. C. Sagle, Y. Wu, V. A. Kusuma and B. D. Freeman. 'Crosslinked poly(ethylene oxide) fouling resistant coating materials for oil/water separation'. In: *Journal of Membrane Science* 307.2 (2008), pp. 260–267.

[79] D. L. Elbert and J. A. Hubbell. 'Reduction of fibrous adhesion formation by a copolymer possessing an affinity for anionic surfaces.' In: *Journal of Biomedical Materials Research* 42.1 (1998), pp. 55–65.

[80] K. D. Park, Y. S. Kim, D. K. Han, Y. H. Kim, E. H. Lee, H. Suh and K. S. Choi. 'Bacterial adhesion on PEG modified polyurethane surfaces.' In: *Biomaterials* 19.7-9 (1998), pp. 851–9.

[81] B. D. Ratner and S. J. Bryant. 'Biomaterials: where we have been and where we are going.' In: *Annual Review of Biomedical Engineering* 6 (2004), pp. 41–75.

[82] A. Abuchowski, J. R. McCoy, N. C. Palczuk, T. van Es and F. F. Davis. 'Effect of covalent attachment of polyethylene glycol on immunogenicity and circulating life of bovine liver catalase.' In: *The Journal of Biological Chemistry* 252.11 (1977), pp. 3582–6.

[83] S. Zalipsky. 'Functionalized Poly(ethylene glycols) for Preparation of Biologically Relevant Conjugates'. In: *Bioconjugate Chemistry* 6.2 (1995), pp. 150–165.

[84] K. Knop, R. Hoogenboom, D. Fischer and U. S. Schubert. 'Poly(ethylene glycol) in drug delivery: pros and cons as well as potential alternatives.' In: *Angewandte Chemie International Edition* 49.36 (2010), pp. 6288–308.

[85] T.-L. Cheng, C.-M. Cheng, B.-M. Chen, D.-A. Tsao, K.-H. Chuang, S.-W. Hsiao, Y.-H. Lin and S. R. Roffler. 'Monoclonal antibody-based quantitation of poly(ethylene glycol)-derivatized proteins, liposomes, and nanoparticles.' In: *Bioconjugate Chemistry* 16.5 (2005), pp. 1225–31.

[86] R. L. Schoch and R. Y. H. Lim. 'Non-Interacting Molecules as Innate Structural Probes in Surface Plasmon Resonance.' In: *Langmuir* 29.12 (2013), pp. 4068–4076.

[87] J. a. De Feijter, J. Benjamins and F. A. Veer. 'Ellipsometry as a tool to study the adsorption behavior of synthetic and biopolymers at the air-water interface'. In: *Biopolymers* 17.7 (1978), pp. 1759–1772.

[88] J. L. Hutter and J. Bechhoefer. 'Calibration of atomic-force microscope tips'. In: *Review of Scientific Instruments* 64.7 (1993), p. 1868.

[89] H. J. Butt and M. Jaschke. 'Calculation of thermal noise in atomic force microscopy'. In: *Nanotechnology* 6.1 (1995), pp. 1–7.

[90] D. Nečas and P. Klapetek. 'Gwyddion: an open-source software for SPM data analysis'. In: *Open Physics* 10.1 (2011), pp. 181–188.

[91] H. Hertz. 'Ueber die Berührung fester elastischer Körper.' In: *Journal für die reine und angewandte Mathematik* 92 (1882), pp. 156–171.

[92] C. A. Schneider, W. S. Rasband and K. W. Eliceiri. 'NIH Image to ImageJ: 25 years of image analysis'. In: *Nature Methods* 9.7 (2012), pp. 671–675.

[93] P. Kingshott, H. Thissen and H. J. Griesser. 'Effects of cloud-point grafting, chain length, and density of PEG layers on competitive adsorption of ocular proteins.' In: *Biomaterials* 23.9 (2002), pp. 2043–56.

[94] R. L. Schoch, L. E. Kapinos and R. Y. H. Lim. 'Nuclear transport receptor binding avidity triggers a self-healing collapse transition in FG-nucleoporin molecular brushes.' In: *Proceedings of the National Academy of Sciences of the United States of America* 109.42 (2012), pp. 16911–6.

[95] W. Norde and D. Gage. 'Interaction of Bovine Serum Albumin and Human Blood Plasma with PEO-Tethered Surfaces: Influence of PEO Chain Length, Grafting Density, and Temperature'. In: *Langmuir* 20.10 (2004), pp. 4162–4167.

[96] T. Sannomiya, O. Scholder, K. Jefimovs, C. Hafner and A. B. Dahlin. 'Investigation of plasmon resonances in metal films with nanohole arrays for biosensing applications.' In: *Small* 7.12 (2011), pp. 1653–63.

[97] J. Junesch, T. Sannomiya and A. B. Dahlin. 'Optical Properties of Nanohole Arrays in Metal-Dielectric Double Films Prepared by Mask-on-Metal Colloidal Lithography.' In: *ACS nano* 6.11 (2012), pp. 10405–10415.

[98] N. Backmann, N. Kappeler, T. Braun, F. Huber, H.-P. Lang, C. Gerber and R. Y. H. Lim. 'Sensing surface PEGylation with microcantilevers'. In: *Beilstein Journal of Nanotechnology* 1.1 (2010), pp. 3–13.

[99] T. W. Kelley, P. A. Schorr, K. D. Johnson, M. Tirrell and C. D. Frisbie. 'Direct Force Measurements at Polymer Brush Surfaces by Atomic Force Microscopy'. In: *Macromolecules* 31.13 (1998), pp. 4297–4300.

[100] M. Patra and P. Linse. 'Simulation of grafted polymers on nanopatterned surfaces.' In: *Nano Letters* 6.1 (2006), pp. 133–7.

[101] G. Stan, F. W. DelRio, R. I. MacCuspie and R. F. Cook. 'Nanomechanical properties of polyethylene glycol brushes on gold substrates.' In: *The Journal of Physical Chemistry. B* 116.10 (2012), pp. 3138–47.

[102] Z. Drira and V. K. Yadavalli. 'Nanomechanical measurements of polyethylene glycol hydrogels using atomic force microscopy.' In: *Journal of the Mechanical Behavior of Biomedical Materials* 18 (2013), pp. 20–8.

[103] E. Evans. 'Probing the relation between force–lifetime–and chemistry in single molecular bonds.' In: *Annual Review of Biophysics and Biomolecular Structure* 30 (2001), pp. 105–28.

[104] M. Deng, X. Li, H. Liang, B. Caswell and G. E. Karniadakis. 'Simulation and modelling of slip flow over surfaces grafted with polymer brushes and glycocalyx fibres'. In: *Journal of Fluid Mechanics* 711 (2012), pp. 192–211.

[105] M. Gelbert, M. Biesalski, J. Rühe and D. Johannsmann. 'Collapse of polyelectrolyte brushes probed by noise analysis of a scanning force microscope cantilever'. In: *Langmuir* 16.13 (2000), pp. 5774–5784.

[106] H.-J. Butt, M. Kappl, H. Mueller, R. Raiteri, W. Meyer and J. Rühe. 'Steric Forces Measured with the Atomic Force Microscope at Various Temperatures'. In: *Langmuir* 15.7 (1999), pp. 2559–2565.

[107] D. G. Castner and B. D. Ratner. 'Biomedical surface science: Foundations to frontiers'. In: *Surface Science* 500.1–3 (2002), pp. 28–60.

[108] A. E. Nel, L. Mädler, D. Velegol, T. Xia, E. M. V. Hoek, P. Somasundaran, F. Klaessig, V. Castranova and M. Thompson. 'Understanding biophysicochemical interactions at the nano-bio interface.' In: *Nature Materials* 8.7 (2009), pp. 543–57.

[109] B. D. Ratner. 'The engineering of biomaterials exhibiting recognition and specificity.' In: *Journal of Molecular Recognition* 9.5-6 (1996), pp. 617–25.

[110] L. L. Hench and J. M. Polak. 'Third-generation biomedical materials.' In: *Science* 295 (2002), pp. 1014–1017.

[111] P. Wu, D. G. Castner and D. W. Grainger. 'Diagnostic devices as biomaterials: a review of nucleic acid and protein microarray surface performance issues.' In: *Journal of Biomaterials Science. Polymer Edition* 19.6 (2008), pp. 725–53.

[112] G. Blobel. 'Protein targeting (Nobel lecture).' In: *ChemBioChem* 1.2 (2000), pp. 86–102.

[113] J. J. Gray. 'The interaction of proteins with solid surfaces.' In: *Current Opinion in Structural Biology* 14.1 (2004), pp. 110–5.

[114] P. Mitchell. 'A perspective on protein microarrays.' In: *Nature biotechnology* 20 (2002), pp. 225–229.

[115] D. Falconnet, D. Pasqui, S. Park, R. Eckert, H. Schift, J. Gobrecht, R. Barbucci and M. Textor. 'A Novel Approach to Produce Protein Nanopatterns by Combining Nanoimprint Lithography and Molecular Self-Assembly'. In: *Nano Letters* 4.10 (2004), pp. 1909–1914.

[116] L. A. Ruiz-Taylor, T. L. Martin, F. G. Zaugg, K. Witte, P. Indermuhle, S. Nock and P. Wagner. 'Monolayers of derivatized poly(L-lysine)-grafted poly(ethylene glycol) on metal oxides as a class of biomolecular interfaces.' In: *Proceedings of the National Academy of Sciences of the United States of America* 98.3 (2001), pp. 852–7.

[117] S. Tugulu, A. Arnold, I. Sielaff, K. Johnsson and H.-A. Klok. 'Protein-functionalized polymer brushes.' In: *Biomacromolecules* 6.3 (2005), pp. 1602–7.

[118] J. M. Harris, ed. *Poly (ethylene glycol) chemistry: biotechnical and biomedical applications*. Springer Science & Business Media, 1992.

[119] J. L. Dalsin, B.-H. Hu, B. P. Lee and P. B. Messersmith. 'Mussel adhesive protein mimetic polymers for the preparation of nonfouling surfaces.' In: *Journal of the American Chemical Society* 125.14 (2003), pp. 4253–4258.

[120] T.-L. Cheng, P. Y. Wu, M. F. Wu, J. W. Chern and S. R. Roffler. 'Accelerated clearance of polyethylene glycol-modified proteins by anti-polyethylene glycol IgM.' In: *Bioconjugate Chemistry* 10.3 (1999), pp. 520–8.

[121] Y.-C. Su, B.-M. Chen, K.-H. Chuang, T.-L. Cheng and S. R. Roffler. 'Sensitive quantification of PEGylated compounds by second-generation anti-poly(ethylene glycol) monoclonal antibodies.' In: *Bioconjugate Chemistry* 21.7 (2010), pp. 1264–1270.

[122] E. S. Gil and S. M. Hudson. 'Stimuli-reponsive polymers and their bioconjugates'. In: *Progress in Polymer Science* 29.12 (2004), pp. 1173–1222.

[123] R. B. Schasfoort and A. J. Tudos. *Handbook of surface plasmon resonance*. Royal Society of Chemistry, 2008.

[124] A. Halperin. 'Polymer brushes that resist adsorption of model proteins: Design parameters'. In: *Langmuir* 15.7 (1999), pp. 2525–2533.

[125] W. Hartmann, N. Saptharishi, X. Y. Yang, G. Mitra and G. Soman. 'Characterization and analysis of thermal denaturation of antibodies by size exclusion high-performance liquid chromatography with quadruple detection'. In: *Analytical Biochemistry* 325.2 (2004), pp. 227–239.

[126] D. A. Herold, K. Keil and D. E. Bruns. 'Oxidation of polyethylene glycols by alcohol dehydrogenase'. In: *Biochemical Pharmacology* 38.1 (1989), pp. 73–76.

[127] K. Yoshimoto, M. Nishio, H. Sugasawa and Y. Nagasaki. 'Direct Observation of Adsorption-Induced Inactivation of Antibody Fragments Surrounded by Mixed-PEG Layer on a Gold Surface.' In: *Journal of the American Chemical Society* 132.23 (2010), pp. 7982–7989.

[128] N. L. Rosi and C. A. Mirkin. 'Nanostructures in biodiagnostics.' In: *Chemical Reviews* 105.4 (2005), pp. 1547–62.

[129] A. Plückthun and P. Pack. 'New protein engineering approaches to multivalent and bispecific antibody fragments.' In: *Immunotechnology* 3.2 (1997), pp. 83–105.

[130] S. W. P. Chan, S.-P. Hung, S. K. Raman, G. W. Hatfield, R. H. Lathrop, N. A. Da Silva and S.-W. Wang. 'Recombinant human collagen and biomimetic variants using a de novo gene optimized for modular assembly.' In: *Biomacromolecules* 11.6 (2010), pp. 1460–9.

[131] A. Halperin and M. Kröger. 'Ternary protein adsorption onto brushes: strong versus weak.' In: *Langmuir* 25.19 (2009), pp. 11621–34.

[132] P. Tompa and A. Fersht. *Structure and function of intrinsically disordered proteins.* CRC Press, 2009.

[133] L. J. Terry, E. B. Shows and S. R. Wente. 'Crossing the nuclear envelope: hierarchical regulation of nucleocytoplasmic transport.' In: *Science* 318.5855 (2007), pp. 1412–6.

[134] R. Y. H. Lim, B. Fahrenkrog, J. Köser, K. Schwarz-Herion, J. Deng and U. Aebi. 'Nanomechanical basis of selective gating by the nuclear pore complex.' In: *Science* 318.5850 (2007), pp. 640–3.

[135] M. Ulbricht. 'Advanced functional polymer membranes'. In: *Polymer* 47.7 (2006), pp. 2217–2262.

[136] D. C. Kim and D. J. Kang. 'Molecular Recognition and Specific Interactions for Biosensing Applications'. In: *Sensors* 8.10 (2008), pp. 6605–6641.

[137] M. Linkert et al. 'Metadata matters: access to image data in the real world'. In: *The Journal of Cell Biology* 189.5 (2010), pp. 777–782.

Acknowledgements

First and foremost I want to thank my PhD advisor Roderick Lim. I thank Rod for giving me the opportunity to perform interesting research in his lab and for giving me a lot of freedom to think and to work on things that interested me. I learned a lot from him, how to think critically, how to write scientific texts, how to perform good research. I also want to thank Thomas Pfohl and Wolfgang Meier for taking the time to be on my advisory committee and being my co-examiners. I thank both for giving me advise and answering my questions occasionally.

Many thanks go to my old and current office mates Teba, Unai, Larisa, Orit, Raphael, Kai, Ludovit, Marija, Marko and Philipp. I had always a lot of fun and also nice scientific discussions with you all. The same goes for the rest of the Lim Nanobiology group, Rafael, Chantal, Selim and Leon.

Acknowledgements go to Deng Jie for nanofabricating our Au nanoring samples, to Steve Roffler for providing Anti-PEG antibodies, to Raphael Wagner for showing to me how to work with the DLS and SPR machines, to Unai Silvan for providing the rabbit serum, and to Cora-Ann Schönenberger for showing me some of the biology lab techniques. Thanks to Andreas Dahlin for providing the nanohole samples and for pointing me towards PEG cloud point grafting, and Rafael Schoch for performing the Anti-PEG SPR measurements.

List of Publications

- Plodinec M., Loparic M., Monnier C.A., Obermann E.C., Zanetti-Dallenbach R., Oertle P., Hyotyla J.T., Aebi U., Bentires-Alj M., Lim R.Y.H., Schoenenberger C-A., 2012. "The Nanomechanical Signature of Breast Cancer." *Nature Nanotechnology*, 7(11), pp.757–65.

- Hyotyla J.T., Lim, R.Y.H., 2012. "Atomic Force Microscopy (AFM)." *Supramolecular Chemistry: From Molecules to Nanomaterials.* Eds. J.W. Steed & P.A. Gale. pp. 659–668 (book chapter).

- Hyotyla J.T., Deng J., Lim R.Y.H., 2011. "Synthetic Protein Targeting by the Intrinsic Biorecognition Functionality of Poly(ethylene glycol) using PEG Antibodies as Biohybrid Molecular Adaptors." *ACS Nano*, 5(6), pp.5180–7.